Spring 2021

Demystifying Denitrification: Coordination Complexes Give Valuable Insight into the Reduction of Nitrogen Oxides

Walker R. Marks
Western Washington University, walkermarks15@gmail.com

Demystifying Denitrification: Coordination Complexes Give Valuable Insight into the Reduction of Nitrogen Oxides

By

Walker R. Marks

Accepted in Partial Completion
of the Requirements for the Degree
Master of Science

ADVISORY COMMITTEE

Dr. John D. Gilbertson, Chair

Dr. Margaret L. Scheuermann

Dr. James R. Vyvyan

GRADUATE SCHOOL

David L. Patrick, Dean

Master's Thesis

In presenting this thesis in partial fulfillment of the requirements for a master's degree at Western Washington University, I grant to Western Washington University the non-exclusive royalty-free right to archive, reproduce, distribute, and display the thesis in any and all forms, including electronic format, via any digital library mechanisms maintained by WWU.

I represent and warrant this is my original work, and does not infringe or violate any rights of others. I warrant that I have obtained written permissions from the owner of any third party copyrighted material included in these files.

I acknowledge that I retain ownership rights to the copyright of this work, including but not limited to the right to use all or part of this work in future works, such as articles or books.

Library users are granted permission for individual, research and non-commercial reproduction of this work for educational purposes only. Any further digital posting of this document requires specific permission from the author.

Any copying or publication of this thesis for commercial purposes, or for financial gain, is not allowed without my written permission.

Walker R. Marks

May 10, 2021

Demystifying Denitrification: Coordination Complexes Give Valuable Insight into the Reduction of Nitrogen Oxides

A Thesis
Presented to
The Faculty of
Western Washington University

In Partial Fulfillment
Of the Requirements for the Degree
Master of Science

by
Walker R. Marks
May 2021

Abstract

Increasing human population is driving the need to produce increasing amounts of food without the ability to dramatically increase farmland area. This has been accomplished by the application of increasing amounts of nitrogen containing fertilizers onto croplands. Nitrogen fertilizer overuse is causing imbalance in the natural nitrogen cycle via excessive amounts of high oxidation-state nitrogen entering both the atmosphere and aquatic ecosystems, which are major contributors to global warming and environmental damage. There is a need to explore synthetic systems which are capable of the reduction of these pollutants through pathways such as denitrification. This thesis will explore the functionalization of a dinuclear dinitrosyl iron complex which is capable of coupling nitrosyl to release nitric oxide. The activity of this system is explored through examination of mono-nuclear dinitrosyl complexes as well as modification of the secondary-sphere ligand interactions which allow control of nitrous oxide evolution from a dinuclear dinitrosyl complex. The complete denitrification of nitrate by divalent samarium in a "single pot" is presented, which represents one of few synthetic systems that are capable of such reactivity. Preliminary results on nitrate binding and activating iron complexes based on the pyridinediimine ligand scaffold with tunable secondary-sphere interactions are introduced.

Acknowledgments

Research Advisor:	Dr. John D. Gilbertson
Thesis Committee:	Dr. Margaret L. Scheuermann
	Dr. James R. Vyvyan
Research Group Members:	Hanalei Lewine, Allison Teigen, April Trausch
Former Group Members:	Douglas Baumgartner, Kyle Burns, Wyatt Parks
Instrument Technicians:	Sam Danforth, Dr. Hla Win-Piazza, Kimberly Wurth, Charles Wandler
X-ray Crystallography:	Dr. Lev Zakharov and Dr. Eric Reinheimer
Mossbauer:	Dr. Takele Seda
SQUID:	Dr. John Anderson
Financial Support:	National Institutes of Health and The National Science Foundation

.

Table of Contents

List of Tables and Figures

Supplemental Figures

1.1 Nitrogen Oxides as Pollutants

Though often overlooked as a major source of pollution, agriculture is a significant contributor to global greenhouse gas (GHG) production as well as pollution of fresh and sea water systems.[1] Worldwide agriculture production is expected to increase by 100% between 2005 and 2050 to accommodate for a growing world population and the development of nations, since developed nations will consume more calories per capita.[2] To accommodate this growth in agriculture, increased use of inorganic fertilizers will be necessary. From 1961 to 2013, nitrogen (N) fertilizer use increased from 0.9 to 7.4 grams of N per square meter of cropland per year.[3] Currently, about 30 to 50% of crop yields are attributed to the application of commercial fertilizers.[4] While increased fertilizer input is required to increase crop yield, poor government planning of assistance programs and lack of farmer education on the appropriate application of fertilizers leads to fertilizer overuse.[5,6]

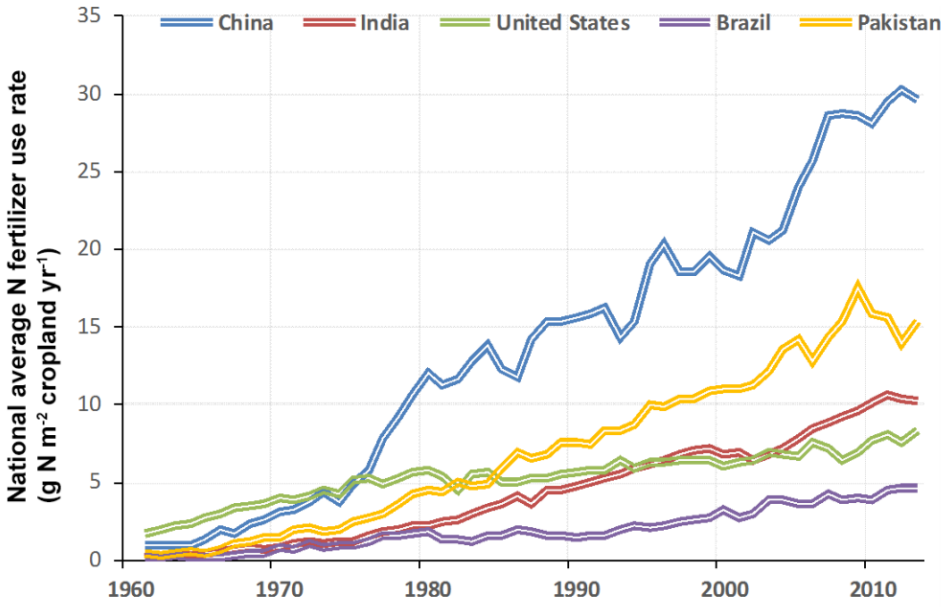

Figure 1.1.1. Average nitrogen fertilizer input for the top five fertilizer consuming countries. Adapted from Chaoqun, L. *Earth Syst. Sci. Data*, **2017**, *9*, 181-192.

With this drastic increase in fertilizer use it is no surprise that 24% of anthropogenic GHG emissions can be attributed to agriculture,[1] with 72% of agricultural nitrous oxide emissions coming directly from fields and grazing areas.[7] Approximately 50% of the N that is added to fields is not taken up by crops, instead being washed away by irrigation or consumed by denitrifying bacteria.[8] GHG emissions

from agriculture are dominated by nitrous oxide, ammonia, methane, and carbon dioxide. Farming contributes to 80% of total yearly nitrous oxide emissions while ammonia and methane are 70% and 40% respectively.[9,10]

GHG emissions are not the only source of agriculture pollution, however, with nitrite and nitrate pollution having serious adverse effects on aquatic systems.[11] With approximately half of applied fertilizer not being taken up by crops, an average of 25% of the unabsorbed N is transported to coastal waters with the rest being converted to gaseous N and stored in soils.[12] The presence of fertilizer run-off in aquatic ecosystems leads to a serious problem. Algal blooms, driven by the presence of significant quantities of N in estuaries such as the Mississippi river basin, cause massive areas of hypoxia (low oxygen concentrations in water) which stifles marine life. The amounts of phosphorous (P) from fertilizer has little effect in highly saline water, however, it should not be overlooked, especially in freshwater systems.[11]

The increase in use of nitrogen fertilizer is affecting the natural nitrogen cycle. Anthropogenic pollution is causing a buildup of nitrate which must be addressed. Taking inspiration from nature, scientists can develop synthetic systems capable of reducing the pollutant nitrate back to benign compounds or even useful feedstocks to close the loop and complete the nitrogen cycle[13,14]

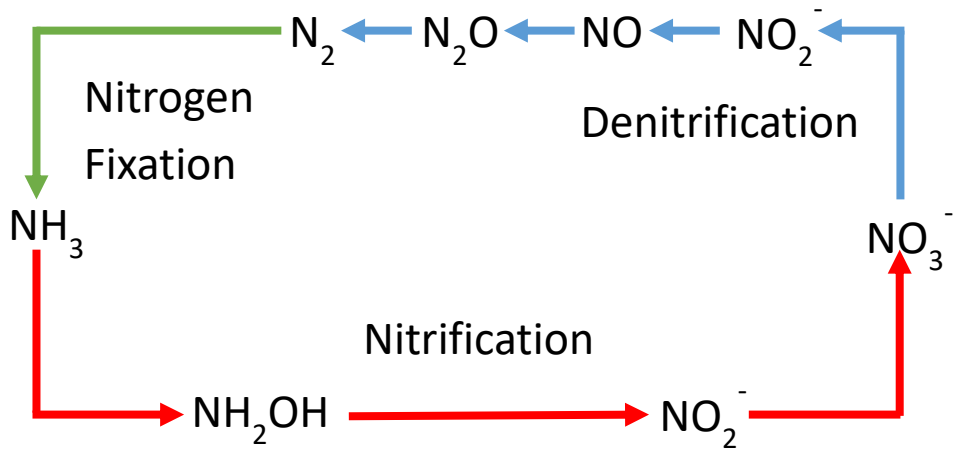

Figure 1.1.2. A simplified nitrogen cycle showing the major pathways.

1.2 Nitric Oxide as a Signaling Molecule

Nitric oxide, a component of the nitrogen cycle, is not only toxic but also an important signaling molecule in many biological systems. The small molecule easily passes through cell membranes and at modest concentrations (nanomolar) is able to affect various essential processes from smooth muscle relaxation, thrombosis, cell propagation, and many others.[15] The production of nitric oxide is handled by the enzyme nitric oxide synthase (NOS) found in many different tissues, endothelial NOS (eNOS) and inducible NOS (iNOS) are thought to primarily act as cardiovascular signalers and inflammation response initiators, respectively.[16] The family of enzymes produce nitric oxide through the oxidation of L-arginine shown by equation 1.[17] While nitric oxide is primarily thought to be produced from L-arginine, as shown below, more recently it has been found that the nitrite anion is also a source of cellular nitric oxide, particularly when the cell is experiencing hypoxia.[18]

$$2\ \text{L-arginine} + 3\ \text{NADPH} + 3\ H^+ + 4\ O_2 \leftrightharpoons 2\ \text{citrulline} + 2\ NO + 4\ H_2O + 3\ NADP^+ \qquad (\mathbf{1.1})$$

Soluble guanylyl cyclase (sGC), a heme-centered protein, is a known target for eNOS generated nitric oxide.[19] Upon reaction with sGC, the five-coordinate iron mononitrosyl complex (MNIC) is formed which in turn produces cyclic guanosine monophosphate (cGMP), the signal for vasodilation as well as many of the other important functions of nitric oxide such as neurotransmission, smooth muscle relaxation, and anti-platelet aggregation.[19] Nitric oxide also plays a role as a cytotoxic agent, and has been investigated as a potential anti-cancer agent. Tumor cells that have been modified to over-express iNOS have shown promise as potential treatment with a minimum therapeutic concentration of nitric oxide around 200 nM, although achieving these high concentrations of nitric oxide has proven difficult.[20] Nitric oxide has also been studied in *E. coli* bacteria for its cytotoxic effects, where it was found that nitric oxide deactivates an iron-sulfur cluster, dihydroxyacid dehydratase (IlvD), causing branched chain amino acid (BCAA) depletion and subsequent cell death.[21]

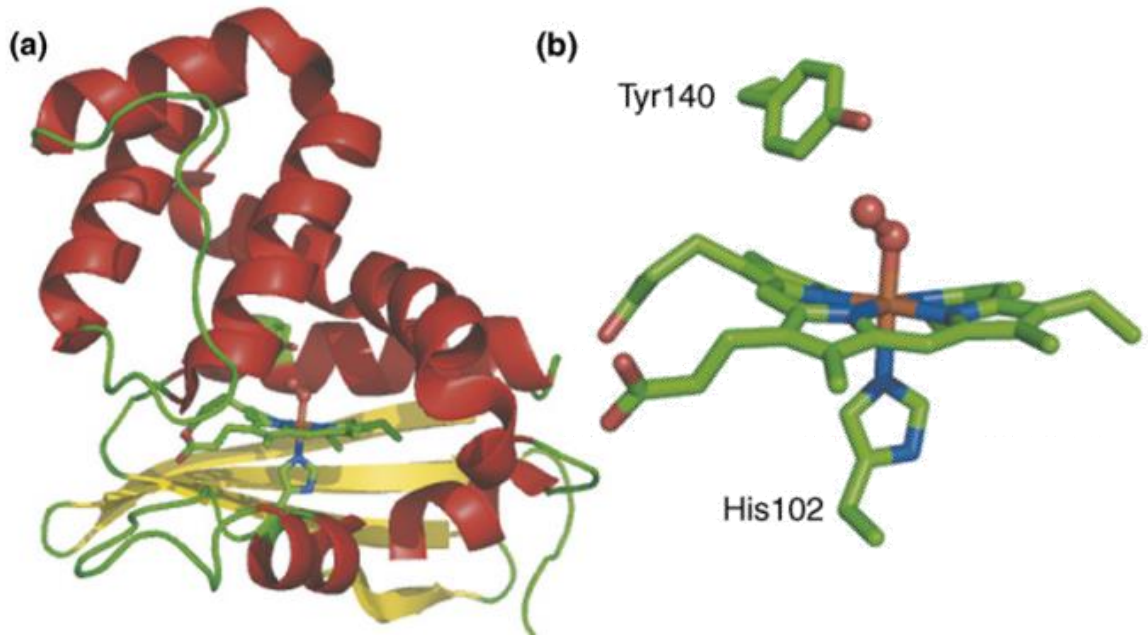

Figure 1.2.1. The heme domain of mammalian sGC with an O_2 ligand bound to the iron featuring a hydrogen bond to a tyrosine residue (a) and close-up of the heme (b). Adapted from Poulos, T. *Current Opinion in Structural Biology*, **2006**, *16*, 736-743.

So far, approximately 200 unique iron-sulfur cluster containing proteins have been identified, controlling important biological processes such as sugar metabolism, heme and biotin biosynthesis, amino acid synthesis, RNA modification, DNA synthesis and repair, and gene expression regulation.[22] Nitric oxide is thought to act as a biological signal by modification of these non-heme iron-sulfur cluster proteins as well as targeting heme-containing proteins.[21] *In vitro* studies have shown that, when introduced to nitric oxide, iron-sulfur proteins form dinitrosyl iron complexes (DNICs). Formation of these complexes is often times monitored by the appearance of an electron paramagnetic resonance (EPR) signal at g = 2.04.[23] Nitric oxide plays a significant role in biology, therefore, studying the pathways that nitric oxide controls as well as the products of its biological targets is of importance to the greater scientific community.

1.3 Biological Roles of DNICs

Various studies have shown that nitric oxide is used in biological systems to modify [2Fe-2S] and [4Fe-4S] type cluster proteins to form stable DNICs,[23] however, it has been suggested that these DNICs are not only the inactivated or modified forms of iron-sulfur clusters, but are also capable of delivering nitric oxide themselves.[24] DNICs are thought to be the most abundant nitric oxide containing species in cells because nitric oxide is highly reactive; DNIC concentration in cells tracks with the upregulation of iNOS even at low concentrations of nitric oxide (50 nM).[25] The ultimate fate of these intercellular DNICs, however, is still not well understood.

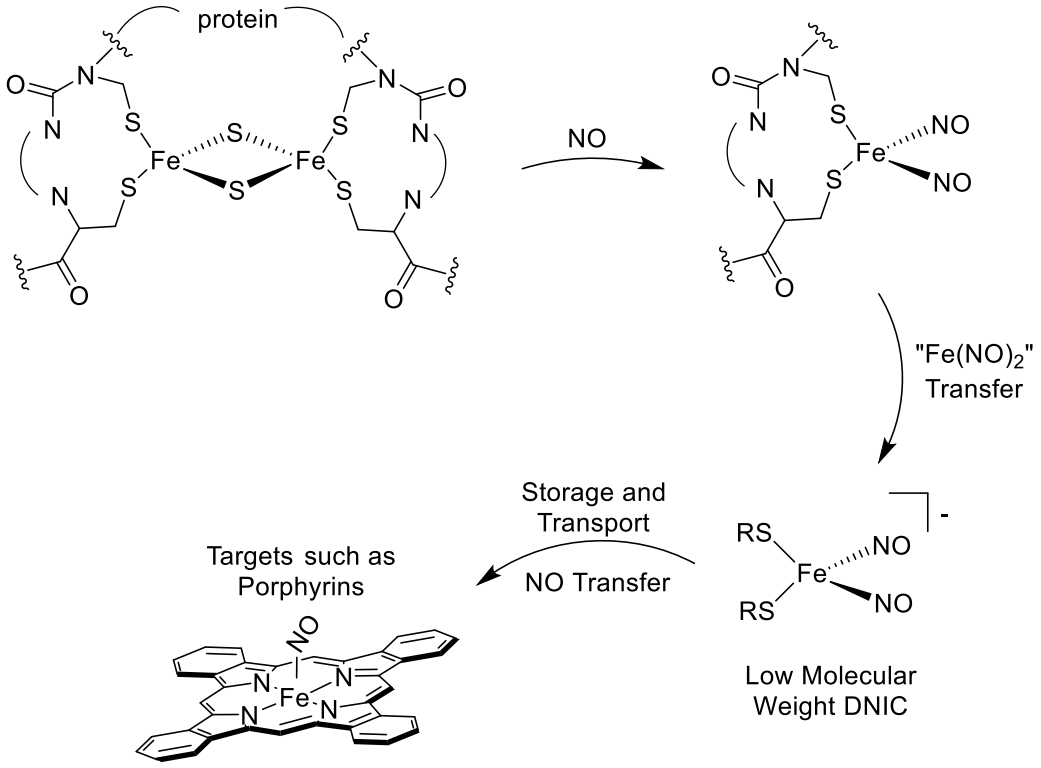

Figure 1.3.1. Nitric Oxide targeting of a generic [2Fe-2S] protein with subsequent DNIC transfer and heme nitrosylation.

As the importance of DNICs in biological systems is slowly understood, their exact function is still a mystery and the focus of intense research.[26] Repair of DNICs back to [Fe-S] motifs often can be

undertaken without the need for new protein synthesis such as in the case of endonuclease III repair by l-cysteine, cysteine desulfurase (IscS) and ferrous iron.[27]

Roussin's red ester and the reduced Roussin's red ester have been studied as biomimetics of [2Fe-2S] clusters, the latter of which is easily studied due to being EPR active.[28] The reaction of nitric oxide with Rieske type clusters, [2Fe-2S] clusters where one of the irons is bound to histidine ligands rather than the usual cystine, indicates that dinuclear DNICs are likely the prominent species that is responsible for the biological roles of nitric oxide when bound to iron-sulfur clusters. Other dinuclear, non-iron-sulfur clusters have been synthesized to try and model the reactivity seen in biological DNICs as well as in other systems such as functional mimics of nitric oxide reductase.[29–31]

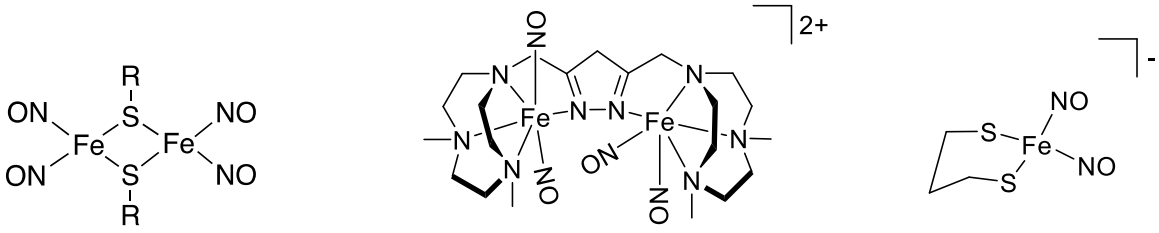

Figure 1.3.2. A generic Roussin's red ester (left) and two examples of synthetic DNICs.

1.4 Denitrification in Nature and Synthetic Systems

Denitrification is an important pathway in the nitrogen cycle, encompassing the reduction of nitrate to dinitrogen. Nature utilizes four different metalloenzymes to complete the transformation from nitrate to dinitrogen, a five electron and six proton process to yield half an equivalent of dinitrogen. To date, there are only two synthetic systems that are capable of the transformation from nitrate to dinitrogen on a single metal center, the first being a nickel centered PNP complex and the second a lanthanide system.[32,13] Many microbes that perform tasks along the denitrification pathway are unable to complete the process leading to the release of gaseous nitrogen oxides as GHG's.[33]

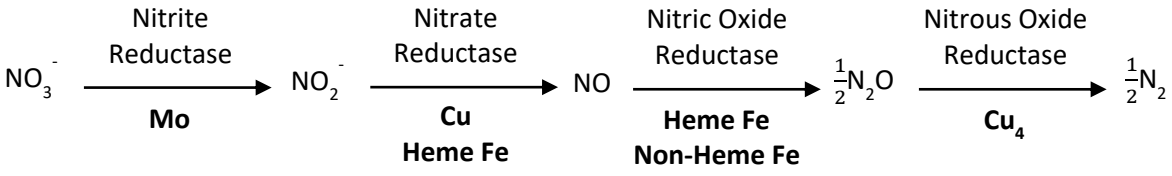

Figure 1.4.1. Denitrification in biology, enzymes are named above each step with the active site metal below.

The conversion of nitrate to nitrite is handled biologically by nitrate reductase (NR) which is dependent on a molybdenum cofactor in all forms of NR.[34] Synthetically, there are several systems which boast the ability to reduce nitrate. Notable examples include inner sphere reduction of nitrate by the lanthanide cerium(III) to nitrite.[35] Other examples are iron pyridinediimine (PDI) complexes with hydrogen bond donors in the secondary coordination-sphere that reduce nitrate to nitrosyl,[36] and a molybdenum complex that releases nitrite.[37]

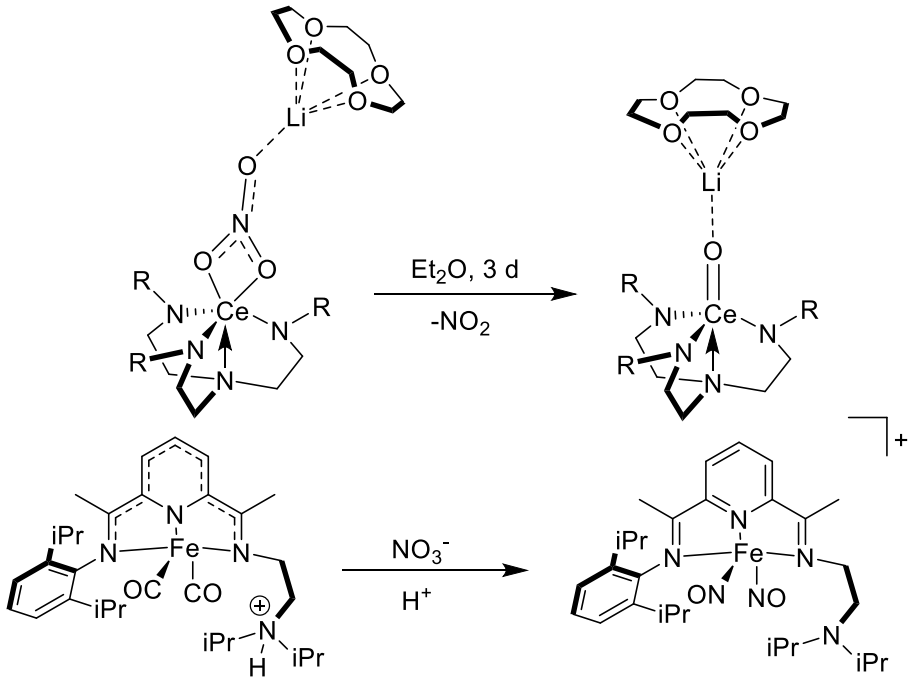

Figure 1.4.2. A general scheme of nitrate reduction by a Ce(III) complex (top) and a Fe PDI complex (bottom).

Nitrite reduction biologically can go through two different pathways, either by the multielectron reduction to ammonium,[38] or the single electron reduction to nitrosyl.[39] The reduction to ammonium

being utilized for protein synthesis and reduction to nitrosyl as a terminal electron acceptor for anerobic respiration. Many synthetic systems have been designed to mimic the activity of the latter case, for example the above iron PDI complex and its associated complexes are able to reduce nitrite to nitrosyl forming stable DNICs.[40,36,41] The DNICs formed through this reaction have been studied extensively for their ability to act as mimics of the DNICs formed in intracellular nitric oxide reactions and because of their unusual electronic structures.[26,42]

Nitric oxide reduction, the next step along the denitrification pathway, is handled by the family of enzymes known as nitric oxide reductase (NOR). Bacterial cytochrome c dependent NOR (cNOR) features a bimetallic active center with a heme and non-heme, Glu, His, His, His coordinated iron center,[43] the mechanism of this reaction is still debated.[44] The aforementioned reaction, done by bacteria in soil, is the largest contributor to global nitrous oxide emissions and research has been undertaken to try and limit the activity of such bacteria.[45] In synthetic systems, nitric oxide reduction is often reported to proceed through a hyponitrite species,[29,46] and the N-N bond formation and N-O bond cleavage in the reductive coupling of nitric oxide are of particular interest to synthetic chemists.[43]

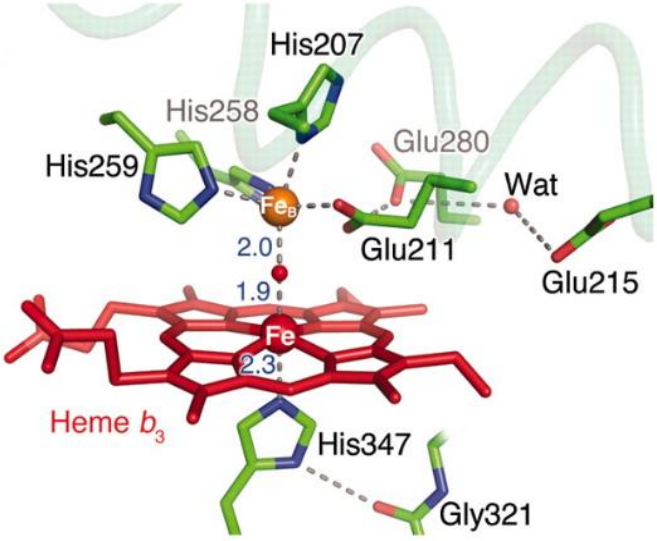

Figure 1.4.3. Illustration of the active site from bacterial nitric oxide reductase showing the heme b_3 iron and the non-heme Glu, His, His, His coordinated iron centers with a bridging oxide. Adapted from Hino, T. *Science* **2010**, *330*, 1666-1670.

The final step in denitrification, the reduction of nitrous oxide to dinitrogen is handled by nitrous oxide reductase (N_2OR) in denitrifying bacteria. These bacteria use nitrous oxide as an electron acceptor for respiration, utilizing a dicopper active site.[47] This reaction is of particular interest due to the potency of nitrous oxide as a GHG and its deleterious effects on the ozone layer.[48] Several homogeneous systems have been developed to mimic this reactivity by catalytic hydrogenation of nitrous oxide.[49,50]

The denitrification pathway of the nitrogen cycle is an important set of reactions. These reactions not only are important in biology, where plants and bacteria use nitrogen oxides for synthesis and respiration, but also in synthetic chemistry where N-N bond formation is desired, or when fighting the advance of climate change induced by human activity.

1.5 Redox Active Ligands

Redox active ligands can accept (or donate) electrons, but this class of ligand generally has a clearly defined oxidation state, where as a ligand classified as redox non-innocent has an ambiguous oxidation state. Redox non-innocent ligands are not a new concept in coordination chemistry, with Jorgensen classifying ligands as "innocent" or "noninnocent" in 1966.[51] There are many different non-innocent ligands, however, potentially the most ubiquitous is the porphyrin. Many examples of porphyrins exist in biology with one example of this being compound I in cytochrome P450; this heme acts as a hydroxylation catalyst which involves a radical cation intermediate.[52] Though these radicals are generally short-lived, some examples of porphyrinoid radicals are very stable.[52]

Nitric oxide or nitrosyl as discussed earlier is another example of a common redox non-innocent ligand. Nitrosyl as a ligand is capable of assuming one of three different oxidation states, NO^+, $NO^\bullet$, and NO^-.[53] In metal mono-nitrosyl complexes, the oxidation state of the nitrosyl can sometimes be indicated by the bending of the M-N-O unit with decreasing bond angle indicating a more reduced nitrosyl.[54] In the case of dinitrosyl complexes, and particularly DNICs, structural analysis often falls short, requiring the use of the Enemark-Feltham notation because of the ambiguity of metal-ligand oxidation states.[55] The

notation $\{M(NO)_x\}^y$ is used to describe the metal nitrosyl unit as a whole with 'y' denoting the number of d-electrons shared between the metal and the nitrosyl(s). For example, a cationic $Fe(NO)_2$ unit bound to two methionines would have a Enemark-Feltham notation of $\{Fe(NO)_2\}^9$ because the iron has eight d-electrons, each nitrosyl has one electron, thiols are neutral ligands (L-type), and the overall charge is +1 so one is subtracted from the count to give nine. Much work has been done to elucidate the formal oxidation states of DNICs with the help of computation.[42]

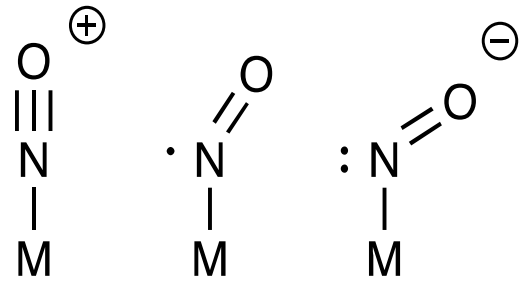

Figure 1.5.1. The three oxidation states of nitric oxide, showing an increasing M-N-O bond angle with reduction. Approximate ranges for M-N-O bond angles are as follows; $NO^+ > 165°$, $NO^\bullet > 135°$, $NO^- < 135°$.

Finally, the pyridinediimine (PDI) is an example of a redox-active ligand scaffold that has received much attention. The ability of the PDI to store electrons means that the redox chemistry of the complex is not limited only to what oxidation states are accessible to the metal center itself, but complimented by the ligand scaffold.[56] This ligand scaffold is not only a store for electrons, but also has a highly modifiable secondary sphere, the parts of the ligand that aren't directly involved in binding the metal center. Examples of this include crown-ethers used for anion reduction rate enhancements,[40] hydrogen bond donors that are able to stabilize an iron(II) hydroxo species,[57] and even Lewis bases that are able to enhance rate kinetics while also stabilizing reaction intermediates.[58]

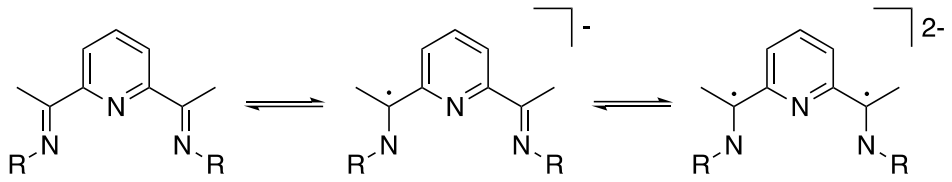

Figure 1.5.2. Three oxidation states of the PDI ligand scaffold which features a N,N,N coordination environment.

These, of course, are not the only examples of redox active ligands.[51] The examples here are important because often the early transition metals are limited in their oxidation states, these types of redox active ligands may lend themselves to enhancing the redox chemistry of the more abundant early metals while granting more noble metal-like properties.

1.6 Lanthanide Deoxygenation

Oxygen atom abstraction has been of interest as a possible route to denitrification, such as the use of the Mashima reagent to reduce nitrate to nitrosyl on a chromium center,[59] or a nickel center that forms a bimetallic complex.[14] The only work that has focused on reduction of nitrate on a lanthanide was shown only as a route to nitrite, the two electron reduced product.[35] There has been work conducted by Evans et. al. demonstrating $(Cp^*)_2Sm(THF)_2$ as a powerful reductant, capable of deoxygenating nitrous oxide to form a μ-O trivalent samarium complex.[60] Furthermore, it has been shown that divalent samarium is capable of forming N-N bonds from the reduction of nitro groups, which then can be further reduced to form aryl amines.[61] We reasoned that as the lanthanides are reasonably oxophilic,[62] it should be possible to complete the deoxygenation of nitrate to more useful or benign products.

1.7 Project Goals

This thesis will explore denitrification through two pathways, 1) the characterization of the reactivity of a lanthanide system that completes the denitrification pathway on a single metal center and 2) characterization of a Fe(PDI) system that reduces nitrite to nitrosyl which it then couples to release nitrous oxide. The former has shown potential to be an electro-catalytically active system, which has never before been seen in the literature for a lanthanide complex. The latter is applicable to the continued study of iron-nitrosyl complexes as they pertain to biological systems as well as the mechanism of N-N bond formation, which is of interest to synthetic chemists.

2.1 Nitrite Reduction

As described in section **1.4**, nitrite reduction is undertaken in natural systems by a class of enzymes known as nitrite reductases. These enzymes utilize either a dicopper active site or a d_1 heme to facilitate the reduction of nitrite to nitric oxide, a two proton and one electron process.[63] There are many examples of synthetic complexes that will reduce nitrite to nitric oxide, many of which are based on iron coordination complexes that form stable mono and di-nitrosyl complexes.[26,40,58] Studying this reaction as well as the products that are formed can give valuable insight into the activity of biological systems.

The iron-PDI complex, ^{pyrrol}PDIFe(CO)$_2$ (**1Fe(CO)$_2$**), can perform the reduction of two equivalents of nitrite at room temperature and pressure. The reaction is facilitated by the addition of a stoichiometric amount of acid; in this case, two protons per nitrite. The major product that is formed, [^{pyrrol}PDIFe(NO)$_2$]$^+$ (**[1Fe(NO)$_2$]$^+$**), is characterized as a {Fe(NO)$_2$}^{9} in the Enemark-Feltham notation.[55] This notation is useful to scientists studying metal nitrosyl complexes because the redox-noninnocence of the nitrosyl ligands makes formal assignment of metal and nitrosyl oxidation states nearly impossible. Using this notation, the iron-nitrosyl moiety is treated as a single entity with DNIC complexes having two accessible oxidation states. An {Fe(NO)$_2$}^{9} complex, as mentioned above, is the oxidized version of a DNIC which has 9 valence electrons, whereas the {Fe(NO)$_2$}^{10} would be the reduced version of a DNIC having 10 valence electrons.

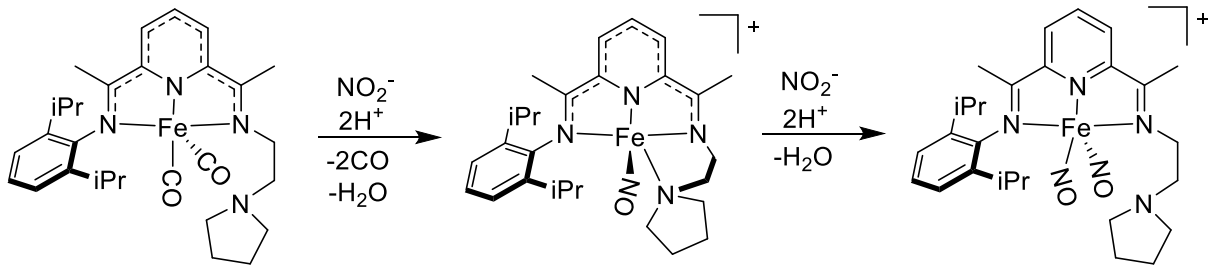

Scheme 2.1.1. A hemi-labile pyrrolidine in the secondary coordination-sphere (left; **1Fe(CO)$_2$**) allows for the isolation of a nitrite reduction intermediate complex (center; **[1Fe(NO)]$^+$**) with the ultimate formation of a {Fe(NO)$_2$}^{9} complex (right; **[1Fe(NO)$_2$]$^+$**).

The rate of nitrite reduction is sensitive to the groups present in the secondary-coordination sphere of the metal and can be increased through the addition of a Lewis acid encapsulated in a crown ether,[40]

or drastically increased by the addition of a proton relay such as is the case with **1Fe(CO)$_2$**.[58] The proton relay in the secondary-coordination sphere was found to be involved not only in assisting proton transfer to the active site, but also as a base that could interact with the metal center itself; this interaction is important in the stabilization of a nitrite reduction intermediate. The presence of a hemi-labile base in the secondary sphere, therefore, could stabilize other similar interactions because of the increase in coordination sites.

2.2 Dinuclear DNIC Synthesis and Characterization

Electrochemical analysis of **[1Fe(NO)$_2$]$^+$** shows two reversible events in MeCN at E ½ = -0.9063 and -1.8388 V, internally referenced to ferrocene (Fc/Fc$^+$ E ½ = 0.00 V), with the former event corresponding to the {Fe(NO)$_2$}$^{9/10}$ redox couple and the latter to the reduction of the PDI backbone. With this knowledge, work was undertaken to isolate the one electron reduced product, ^{Pyrrol}PDIFe(NO)$_2$ (**1Fe(NO)$_2$**). It was found that instead of the formation of the expected mono-nuclear product, ^{Pyrrol}PDIFe$_2$(NO)$_4$ (**1Fe$_2$(NO)$_4$**) was formed. Reduction of **[1Fe(NO)$_2$]$^+$** to form **1Fe$_2$(NO)$_4$** was carried out using the one-electron reductant cobaltocene (E ½ = -1.33 V in DCM) (**Figure 2.2.1**). Upon addition of a concentrated cobaltocene solution to a stirring DCM solution of **[1Fe(NO)$_2$]$^+$** a color change from brown to red/brown was observed as well as the formation of a bright yellow precipitate. Reaction completeness was monitored by transmission IR, following the strong, characteristic ν_{NO}. The solution was allowed to stir for 1 hour before being filtered through celite to remove the yellow precipitate, cobaltocenium hexafluorophosphate, and dried to yield crude product.

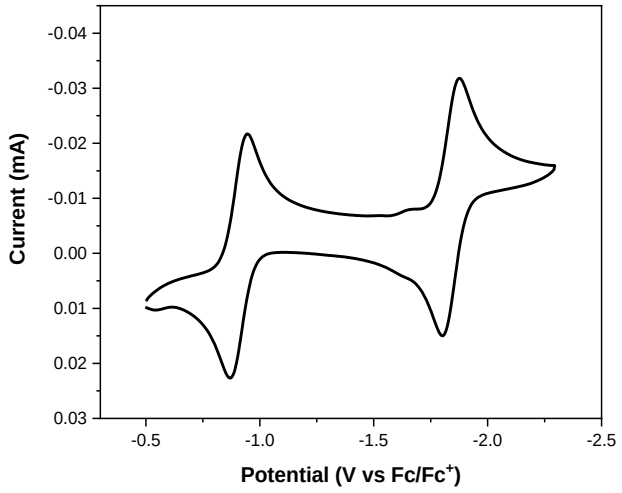

Figure 2.2.1. Cyclic voltammogram of **[1Fe(NO)$_2$]$^+$** (approximately 5 mM) in CH_3CN, glassy carbon working electrode, platinum wire counter electrode, and 0.1 M $TBAPF_6$ supporting electrolyte. OCP: -0.4 V.

Upon reduction, the ν_{NO} of the **[1Fe(NO)$_2$]$^+$** at 1785 and 1716 cm^{-1} (**Figure S1**) shift bathochromically approximately 92 cm^{-1} to 1688 and 1629 cm^{-1} (**Figure 2.2.2**). This shift is consistent with a one-electron reduction of the $Fe(NO)_2$ unit and caused by increased occupancy of the NO antibonding orbitals, weakening the bond.[26] The two observed ν_{NO} for **[1Fe(NO)$_2$]$^+$** split forming four distinct nitrosyl vibrations with an decreased $\Delta\nu_{NO}$ (57 and 61 Δcm^{-1} for **1Fe$_2$(NO)$_4$** versus 70 Δcm^{-1} for **[1Fe(NO)$_2$]$^+$**) which indicate the geometry around the iron centers, as well as the number of nitrosyl ligand, has changed. The identity of the nitrosyl vibrations was confirmed via ^{15}N labeling of the nitrosyl ligands in the synthesis of **[1Fe(NO)$_2$]$^+$** via $Na^{15}NO_2$, which resulted in a $\Delta\nu_{NO}$ of 34 cm^{-1} (calculated $\Delta\nu_{NO}$: 33 cm^{-1}).

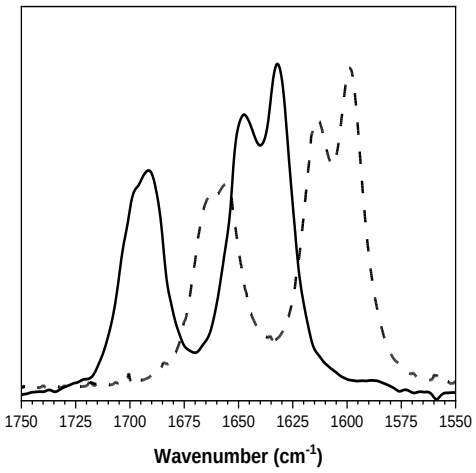

Figure 2.2.2. Transmission IR spectrum of **$1Fe_2(NO)_4$** in DCM with **$1Fe_2(^{15}NO)_4$** (dotted line).

The crude DCM solution of **$1Fe_2(NO)_4$** was layered with pentane to form dark red/brown crystals suitable for X-ray crystallography in 48% yield. The ORTEP image of **$1Fe_2(NO)_4$** (**Figure 2.2.3**) confirms the formation of a new complex featuring two, tetrahedral, dinitrosyl iron centers (τ_4 = 0.855 Fe(1) and 0.867 Fe(2)) (τ_4 = 1 for tetrahedral and = 0 for square planar). Formation of similar complexes was not observed for PDI ligands with no base in the secondary-coordination sphere or with bases that are too sterically encumbered to enter the van der Waals radius of the iron. Analysis of the C_{imine}-N_{imine} bonds between **$[1Fe(NO)_2]^+$** and **$1Fe_2(NO)_4$** (1.284 Å and 1.280 Å, respectively) indicate the PDI scaffold is not directly involved in the reduction. Comparison of the average C_{imine}-$C_{pyridine}$ bonds shows no significant difference (1.488 Å for **$[1Fe(NO)_2]^+$** and 1.475 Å for **$1Fe_2(NO)_4$**), however, these bonds are distorted in **$1Fe_2(NO)_4$** (Δ0.020 Å) because of the change in conformation and therefore comparison of these bonds between the two complexes should be avoided. The lack of C_{imine}-N_{imine} lengthening upon reduction indicates that the PDI ligand remains in the neutral oxidation state. This is in good agreement with the literature assignment of the E ½ = -0.9063 V redox event of **$[1Fe(NO)_2]^+$** belonging to the $\{Fe(NO)_2\}^{9/10}$ couple while the latter event likely belongs to the reduction of the PDI backbone. The nitrosyls on both iron centers are in an 'attracto' conformation and the average nitrosyl bond length increases by 0.015 Å while the Fe-N(O) bonds are observed to shorten by 0.046 Å, a result of the increased π-backbonding between the metal and nitrosyl.

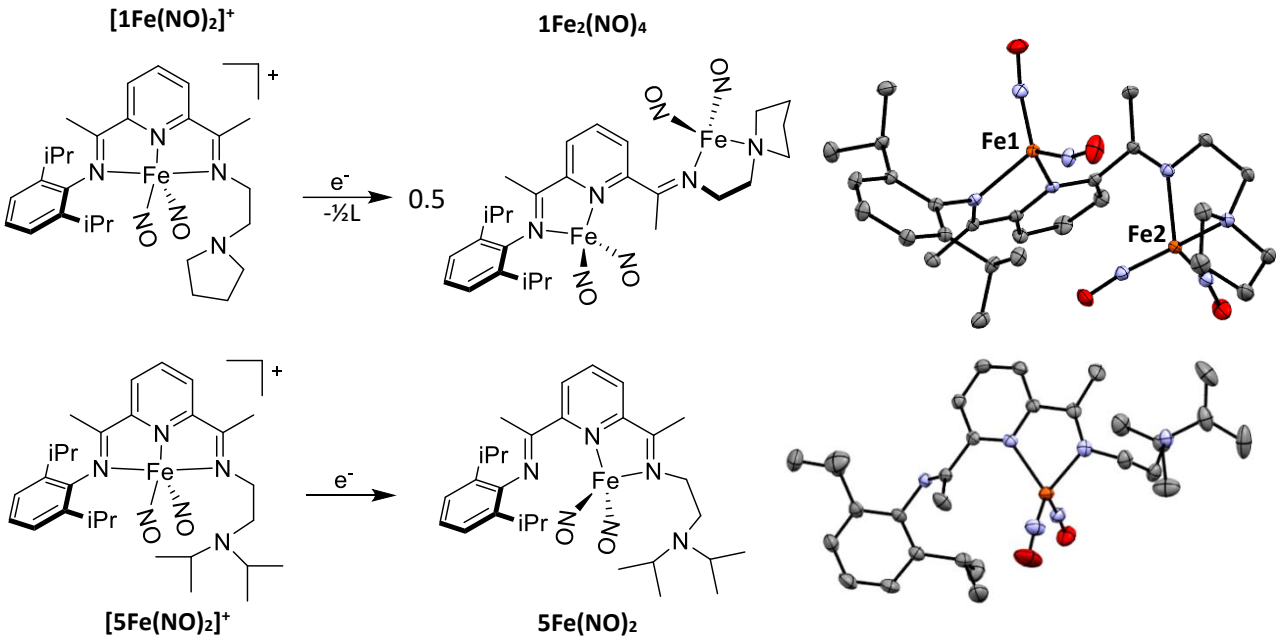

Figure 2.2.3. Reduction of **[1Fe(NO)$_2$]$^+$** to form **1Fe$_2$(NO)$_4$** with ORTEP view of **1Fe$_2$(NO)$_4$** (top) and synthesis of the {Fe(NO)$_2$}^{10} complex **5Fe(NO)$_2$** with a bulky pendant amine, preventing the formation of a dinuclear complex (bottom).

The ^{1}H NMR of **1Fe$_2$(NO)$_4$** in CD_2Cl_2 shows that the complex is diamagnetic (S = 0) (**Figure S20**), which is confirmed in the SQUID experiment seen in Figure **S55** and **S56**. The ^{15}N NMR of **1Fe$_2$(^{15}NO)$_4$**, shown in figure **2.2.4**, features four distinct signals around 380 ppm externally referenced to benzamide. This result is in contrast to the ^{15}N NMR spectra of other mono-nuclear {Fe(NO)$_2$}^{10} complexes that have been synthesized, which all show a single sharp ^{15}N signal, with similar shift to those of **1Fe$_2$(NO)$_4$**. The splitting of the ^{15}N signals in **1Fe$_2$(NO)$_4$** are thought to be a result of the sterically hindered iron-nitrosyl units, making exchange of the nitrosyls slow on the NMR timescale. Assignment of the nitrosyls to an iron center can be accomplished via a ^{1}H, ^{15}N heteronuclear multiple bond correlation (HMBC) experiment, where we observe long-range correlation with the imido-methyl protons, allowing for assignment seen in Figure **S35**.

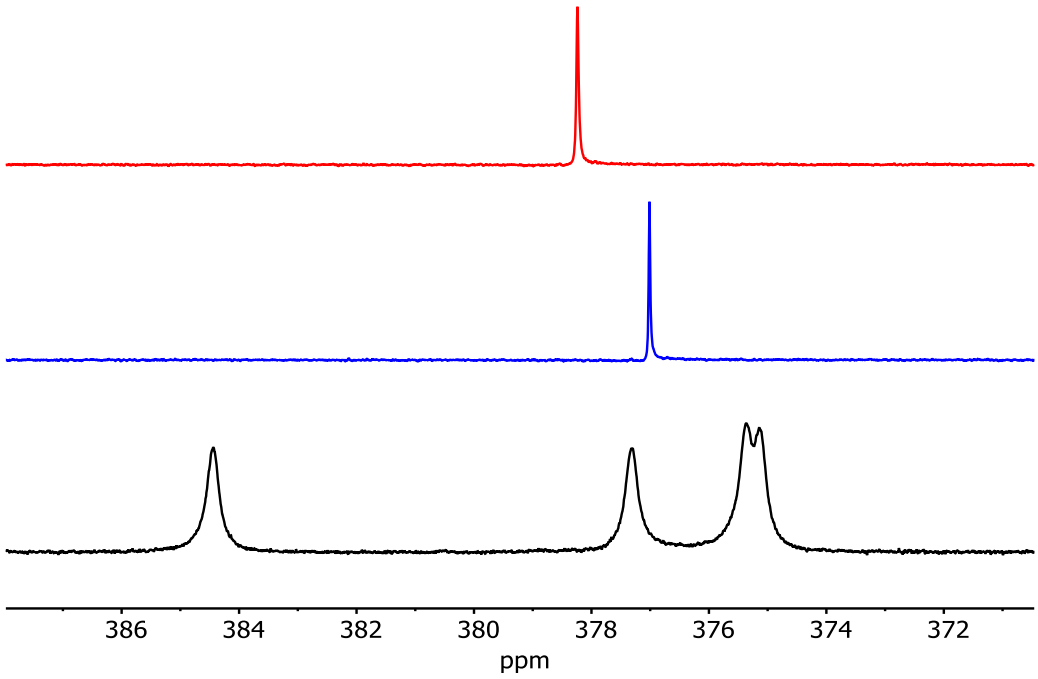

Figure 2.2.4. ^{15}N NMR spectra of **5Fe(NO)$_2$** (red), **2Fe(NO)$_2$** (blue), and **1Fe$_2$(NO)$_4$** (black) in $(CD_3)_2CO$.

The cyclic voltammogram of **1Fe$_2$(NO)$_4$** (**Figure 2.2.5**) shows two reversible events at E ½ = -0.5969 and -2.0017 V as well as an irreversible reduction and oxidation at -1.1418 and -0.7220 V, respectively. The reversible event at -0.5969 V is likely a $\{Fe(NO)_2\}^{9/10}$ couple, while the two irreversible events are attributed to formation of the dinuclear complex, with the pendant pyrrolidine either bound or free. The significant rearrangement of the complex (from mono- to di-nuclear) is likely the cause of the large ΔE^o between events. The final event, E ½ = -2.0017 V, represents the reduction of the PDI scaffold.

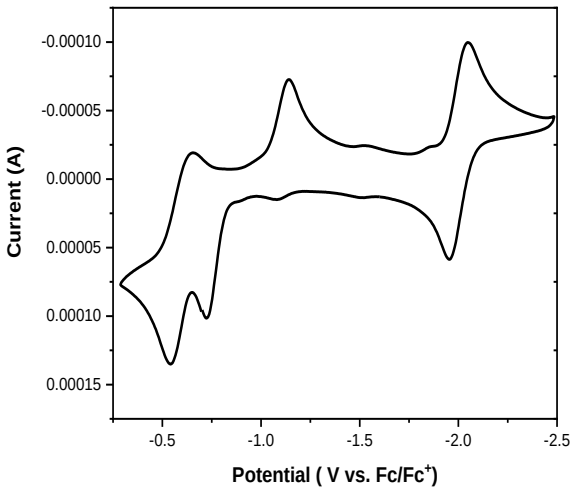

Figure 2.2.5. Cyclic voltammogram of **$1Fe_2(NO)_4$** (approximately 10 mM) in CH_3CN, glassy carbon working electrode, platinum wire counter electrode, and 0.1 M $TBAPF_6$ supporting electrolyte.

The Mössbauer spectrum of **$1Fe_2(NO)_4$** (**Figure 2.2.6**) shows an isomer shift (δ) of 0.186(3) mm/s, shifted from 0.330(5) mm/s for **$[1Fe(NO)_2]^+$**. This small shift is due to increased electron density at the iron center(s) and is consistent with the literature values for these types of compounds.[42] The change in the quadrupole splitting (ΔE_Q) between the two complexes, 0.932(8) mm/s and 0.670(8) mm/s for **$[1Fe(NO)_2]^+$** and **$1Fe_2(NO)_4$** respectively, is a result of the different geometries between the iron centers. As observed in the solid-state structures, **$[1Fe(NO)_2]^+$** exhibits a pseudo-square pyramidal geometry while **$1Fe_2(NO)_4$** is observed to be roughly tetrahedral. At liquid helium temperatures, a large change in the quadrupole splitting of **$1Fe_2(NO)_4$** is observed, this shift could be due to the proximity of the iron centers in the complex, though it may also be attributed to small ferrous impurities in the sample. Fitting of the 6 K Mössbauer spectrum with an assumed two iron sites gives an approximately 50/50 contribution to the observed spectrum.

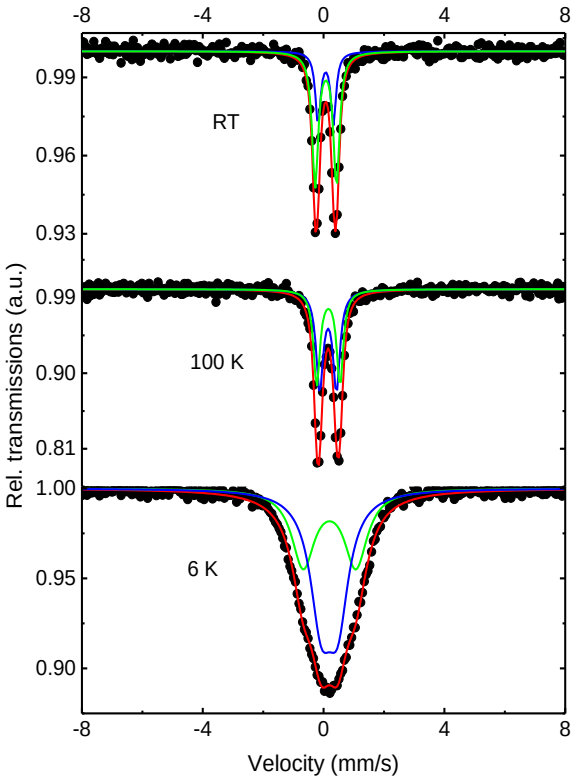

Figure 2.2.6. Zero-field Mossbauer spectra of **$1Fe_2(NO)_4$**. (RT); δ = 0.172(5), 0.176(5) mm/s, ΔE_Q = 0.51(4), 0.70(3) mm/s, Line width, Γ = 0.21(4), 0.25(2) mm/s. . (100 K); δ = 0.250(2), 0.260(5) mm/s, ΔE_Q = 0.56(3), 0.77(4) mm/s, Line width, Γ = 0.28(2), 0.26(3) mm/s. . (6 K); δ = 0.91(6), 0.88(9) mm/s, ΔE_Q = 0.298(7), 0.295(4) mm/s, Line width, Γ = 1.75(6), 0.55(3) mm/s.

2.3 N-N Coupling by a Dinuclear DNIC

The N-N bond formation reaction of bacterial nitric oxide reductase (bacNOR) to form one equivalent of nitrous oxide from two equivalents of nitric oxide is highly sought after reactivity for iron-nitrosyl chemistry.[26,29,30] Significant barriers exist to NO coupling on a DNIC, however, such as the highly covalent nature of the Fe-N(O) bond as well as a large physical distance between nitrosyl ligands preventing N-N coupling.[42]

Attempts to isolate the mixed-valance $\{Fe(NO)_2\}^{10}$-$\{Fe(NO)_2\}^9$ species with **$1Fe_2(NO)_4$** using 1 equivalent of the one-electron oxidant, ferrocenium hexafluorophosphate, consistently resulted in the

regeneration of complex **[1Fe(NO)$_2$]$^+$**. From this reaction approximately 46% of the nitrogen (nitrosyl) could be accounted for as DNIC. Oxidation of the complex via a strong proton source, HCl in ether, also resulted in the formation of **[1Fe(NO)$_2$]$^+$**, however, the counter-ion was found to be $[Fe(NO)_2Cl_2]^-$. The complex was found to be oxidized by other proton sources such as $[NEt_3H]^+$ in THF also resulting in the formation of **[1Fe(NO)$_2$]$^+$**.

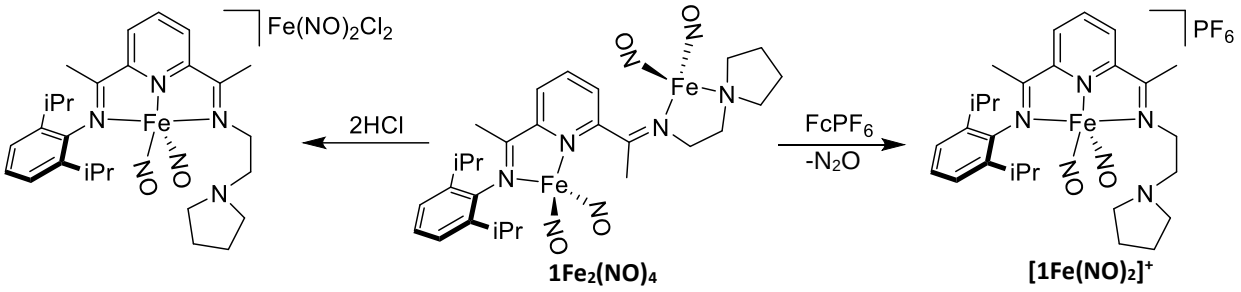

Scheme 2.3.1. Reaction of **1Fe$_2$(NO)$_4$** with HCl in ether or $FcPF_6$ reforms **[1Fe(NO)$_2$]$^+$** with differing counterions.

The headspace of the reaction between **1Fe$_2$(NO)$_4$** and ferrocenium hexafluorophosphate was investigated by gas-phase, transmission IR and found to contain nitrous oxide and no other nitrogen containing species. Nitrous oxide was confirmed to originate from the coupling of nitrosyl by labeling the nitrosyl ligands with ^{15}N as seen in **Figure 2.3.1**. The yield of nitrous oxide was quantified via gas chromatography (**Figure S52**) and found to be 87%, accounting for the missing nitrogen in the formation of**[1Fe(NO)$_2$]$^+$**. The identity of the non-DNIC iron species after reaction is suspected to be some form of iron oxide, though it has not yet been identified. As expected from the crystallographic data, the headspace IR analysis of the reaction of **1Fe$_2$(NO)$_4$** with HCl did not show formation of any gaseous nitrogen oxides.

Although the desired mixed-valence species was not isolated, the one-electron oxidation of **1Fe$_2$(NO)$_4$** does show that the complex exhibits novel reactivity through the coupling of nitrosyl and work was undertaken to try and understand this reactivity.

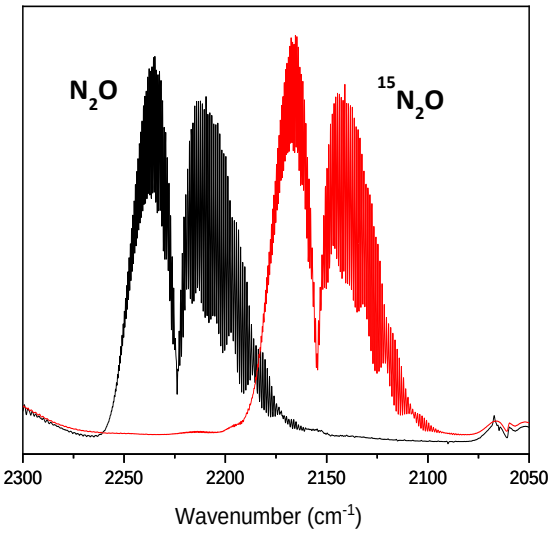

Figure 2.3.1. IR spectrum of **$1Fe_2(NO)_4$** oxidation head space via $FcPF_6$ (black) and **$1Fe_2(^{15}NO)_4$** oxidation (red).

2.4 N-N Coupling Mechanism Studies

Studies to understand the mechanism of nitric oxide coupling at the dinuclear active site of bacNOR are proposed to occur through of the three possible mechanisms shown in **Figure 2.4.1**.[44] The mechanism of nitric oxide coupling in bacNOR could involve either coupling of nitrosyl with exogenous nitric oxide, with Fe_B playing the role of a Lewis acid, coupling of nitrosyls across the two iron centers, or simply coupling of nitrosyl on a DNIC. A similar situation arises when investigating the N-N coupling observed in complex **$1Fe_2(NO)_4$**, where multiple reasonable mechanisms could be proposed. It could be possible that nitric oxide is liberated from the complex upon oxidation which triggers immediate coupling of the now free nitric oxide with a nitrosyl or, perhaps, the proximity of the nitrosyls makes N-N coupling favorable across iron centers without the release of free nitric oxide. In an attempt to eliminate some of the possible mechanisms, multiple control complexes were synthesized to study the reactivity of **$1Fe_2(NO)_4$** and its individual constituents, complexes **$2Fe(NO)_2$** and **$3Fe(NO)_2$** are described in greater detail in section **3.1**.

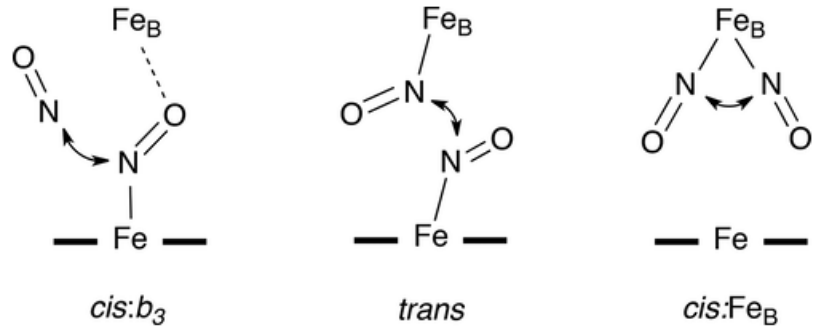

Figure 2.4.1. The three proposed mechanisms of the reductive coupling of nitric oxide by bacNOR.

Headspace analysis of the oxidation of **2Fe(NO)$_2$** in CH_2Cl_2 by ferrocenium hexafluorophosphate (**Figure 2.4.2**) shows trace amounts of nitric oxide and no other nitrogen oxides. Crystallizing the oxidation product showed that the $\{Fe(NO)_2\}^9$ complex was formed as a dimer with a bridging PF_4^- anion along with a PF_6^- in the unit cell to balance charge. Analyzing the reaction headspace after oxidation of the other mono-nuclear control compound, **3Fe(NO)$_2$**, showed formation of a trace amount of nitrous oxide as well as some carbon monoxide, the latter likely due to a small amount of $Fe(NO)_2(CO)_2$ contamination in the starting material. Crystallization of that oxidation product reveals a highly unusual, N,N coordinated, four-coordinate $\{Fe(NO)_2\}^9$ complex, no such complex can be found in the literature. It should also be noted that the product from the oxidation of **3Fe(NO)$_2$**, while stable enough to collect XRD data, is still a meta-stable complex even in the solid state, decomposing over the course of several weeks.

Knowing that neither of the mono-nuclear constituents of **1Fe$_2$(NO)$_4$**, **2Fe(NO)$_2$** and **3Fe(NO)$_2$**, were responsible for the observed evolution of nitrous oxide (**Figure S52** and **S53**), UV-vis was employed to monitor the reaction in an attempt to identify any long-lived reaction intermediates. Oxidation of **1Fe$_2$(NO)$_4$** by ferrocenium hexafluorophosphate in acetone, monitored by UV-vis spectroscopy shows the complete disappearance of the characteristic absorbances at 375 and 472 nm after about 5 min. Soon after, new absorbances appear at 594 and 728 nm, growing to a maximum after approximately 40 min. This absorbance is nearly identical to the MNIC complex, **[1Fe(NO)]$^+$**, and could point towards NO coupling

across iron centers as a possible mechanism for nitrous oxide evolution which would lead to an MNIC intermediate.

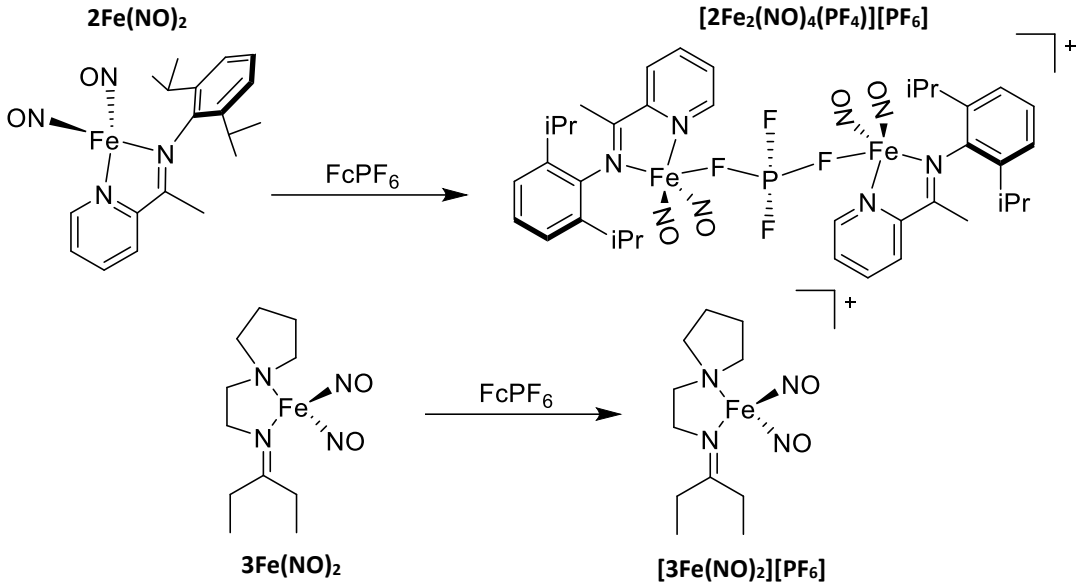

Figure 2.4.2. Control DNICs **2Fe(NO)$_2$** and **3Fe(NO)$_2$** reacting with ferrocenium hexafluorophosphate to for the cationic $\{Fe(NO)_2\}^9$ complexes, the synthesis and characterization of these complexes is described in section **3.1**.

Investigation of the possibility of free nitric oxide reacting with the complexes to form nitrous oxide was investigated by two routes. The first, direct reaction of the complex with nitric oxide gas was carried out with both **1Fe$_2$(NO)$_4$** and **2Fe(NO)$_2$** separately in THF. Both complexes exhibited what was assumed to be stoichiometric nitrous oxide evolution when introduced to nitric oxide and stirred overnight. The iron products from these reactions were, unfortunately, not able to be identified through crystallography. It was also found that complex **[1Fe(NO)]$^+$** reacts with nitric oxide nearly instantaneously in THF to form complex **[1Fe(NO)$_2$]$^+$.** These reactions show the potential for these DNIC complexes to react with nitric oxide, however, it should be noted that there was no attempt made to purify the gas before use leading to the possibility of higher nitrogen oxides being present leading to the observed reactivity.

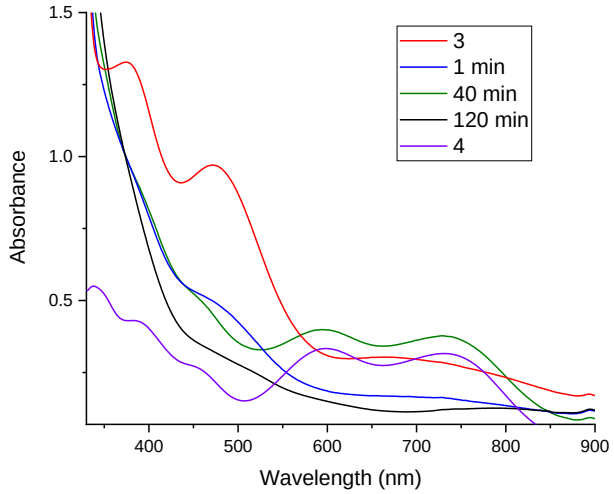

Figure 2.4.3. UV-Vis monitoring of the oxidation of **$1Fe_2(NO)_4$** by $FcPF_6$ in acetone, overlaid with a spectrum of **$[1Fe(NO)]^+$** showing the appearance and subsequent disappearance of a purposed MNIC intermediate. Times indicate the amount of time after injection of the oxidant.

To further confirm the role of nitric oxide in the coupling reaction, the use of a nitric oxide trapping agent, cobalt(II) tetraphenylporphyrin (CoTPP) was employed. It was found that with one equivalent of CoTPP present in solution nitrous oxide evolution was almost entirely eliminated. The solution IR measurements after reaction show three peaks attributed to nitrosyl vibrations at 1800, 1728, and 1688 cm^{-1}, the first two belonging to **$[1Fe(NO)_2]^+$** and the latter belonging to CoTPP(NO). It is of note, however, that if the CoTPP trapping agent was not in solution (i.e. trapping by vial-in-vial) there was no nitric oxide detected. If nitric oxide is released by the complex after one electron oxidation, it is exceptionally short lived before coupling to nitrous oxide.

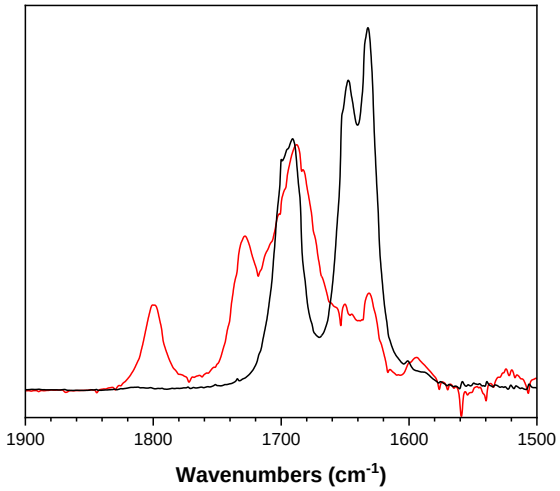

Figure 2.4.4. Solution IR measurement of **$1Fe_2(NO)_4$** with 1 eqivalent CoTPP (black) and after adding 1 equivalent $FcPF_6$ (red) showing the generation of **$[1Fe(NO)_2]^+$** (ν_{NO} 1800 and 1728 cm^{-1}) as well as CoTPP(NO) (ν_{NO}: 1687 cm^{-1}).

To further study the nitrous oxide evolution of dinuclear complexes, a symmetric PDI complex was synthesized, $^{bisPyrrol}PDIFe_2(NO)_4$ (**$4Fe_2(NO)_4$**). This complex features a pendant pyrrolidine and two $\{Fe(NO)_2\}^{10}$ iron centers. The electrochemistry of **$4Fe_2(NO)_4$** features two distinct, reversible $\{Fe(NO)_2\}^{9/10}$ couples (**Figure S38**) as opposed to that of **$1Fe_2(NO)_4$** which has one reversible and one irreversible couple. The root cause of the change in electrochemistry should be attributed to the second pyrrolidine in the secondary-sphere which is able to bind to the iron-nitrosyl unit in the N_{imine}, $N_{pyridine}$ coordination site to form a stable five-corrdinate $\{Fe(NO)_2\}^9$ DNIC. The electrochemical experiment is supported by the chemical oxidation of **$4Fe_2(NO)_4$** by one equivalent of ferrocenium hexafluorophosphate which forms the mixed valence $\{Fe(NO)_2\}^9$-$\{Fe(NO)_2\}^{10}$ complex. The headspace analysis of the one electron oxidation of **$4Fe_2(NO)_4$** contained no nitrogen oxides, indicating that the complex does not couple nitrosyl.

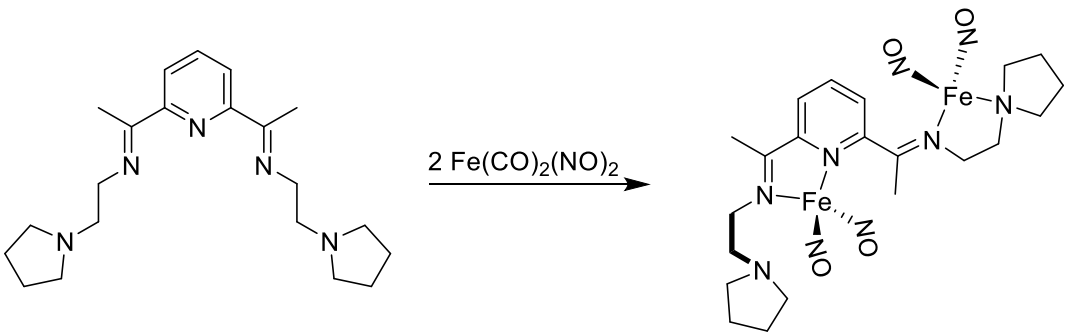

Scheme 2.4.1. Synthesis of **$4Fe_2NO_4$** forming a dinuclear DNIC with a pendant pyrrolidine.

Through these experiments, it appears that a simple mechanism is unlikely or that there are multiple mechanisms at play under different reaction conditions. It is possible that the reaction between these DNIC complexes and nitric oxide does not follow the same pathway that nitrosyl coupling between two discreet iron centers held in close proximity would follow.

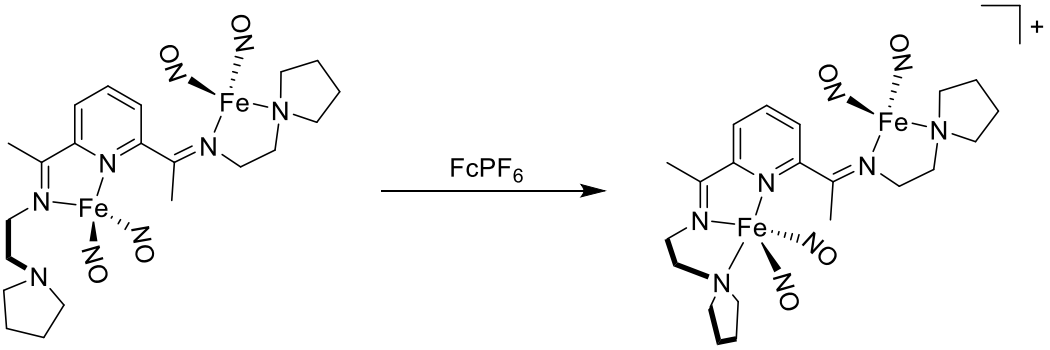

Scheme 2.4.2. Oxidation of **$4Fe_2NO_4$** forming **$[4Fe_2(NO)_4][PF_6]$** with no release or coupling of nitrosyl observed.

2.5 Conclusions and Future Work

Clearly, it can be concluded that the introduction of another metal center has a profound impact on the reactivity of these DNIC complexes and that one of the metal centers being meta-stable is a driver for nitrous oxide elimination from a DNIC. The ability of **$3Fe(NO)_2$** to exist as the cationic, four-coordinate **$[3Fe(NO)_2][PF_6]$** is highly unusual in DNIC chemistry and in stark contrast to **$2Fe(NO)_2$** which forms a five-coordinate complex upon oxidation with both counterions that were tested (PF_6^- and BF_4^-). This result

could be due to simple sterics around the iron in **3Fe(NO)$_2$** not allowing for a five-coordinate complex to form, or it could be due to the electronic effects of the pyridine mono-imine ligand driving instability in the four-coordinate **[2Fe(NO)$_2$]$^+$** complexes leading them to coordinate to anions.

These results demonstrate why **1Fe$_2$(NO)$_4$** is a complex of interest to study and that it will be a source of much exciting chemistry for some time to come. Work will be continued to further understand the reactivity of these DNIC systems as well as the mechanisms of said reactivity.

3.1 DNIC Control Complexes

Following the discovery of nitrous oxide evolution from **$1Fe_2(NO)_4$**, new mononuclear DNICs were synthesized to mimic the individual iron centers found in the dinuclear **$1Fe_2(NO)_4$**. These complexes were investigated as a means to further our understanding of the pathway of nitric oxide coupling observed in the dinuclear **$1Fe_2(NO)_4$** system. While these studies do not necessarily give a complete view of the reaction mechanism, they can be of value to understanding the reactivity of the notoriously stable DNIC.[42] The synthesis of these new mononuclear complexes lead to the isolation and characterization of new species along the chosen synthetic pathways. In this chapter, the synthesis and characterization of the **^{Ar}MIP** and **^{Pyrrol}Imine** complexes will be discussed as well as the reduction of the previously described $\{Fe(NO)_2\}^9$ DNIC, **$[5Fe(NO)_2]^+$**,[36] to form the mononuclear $\{Fe(NO)_2\}^{10}$ complex in the PDI ligand scaffold.

3.2 Synthesis and Characterization of ^{Ar}MIP Complexes

The mono-imine pyridine, ^{Ar}MIP (**L2**), ligand scaffold was synthesized by stirring 2-acetylpyridine and 2,6-diisopropyl aniline in MeOH overnight with a catalytic amount of formic acid. The free ligand was isolated by removing the MeOH and adding MeCN, then placing in the freezer overnight to yield crystalline ligand.

^{Ar}MIP$FeBr_2$ (**$[2FeBr_2]_2$**) was synthesized by stirring **L2** with 1 molar equivalent of iron(II) bromide in MeCN. This resulted in an almost immediate color change from yellow of the free ligand to red/purple. The solution was stirred overnight, then filtered through celite and layered with Et_2O to yield dark purple, X-ray quality crystals of **$[2FeBr_2]_2$**. The ORTEP view of **$[2FeBr_2]_2$** shows a dimeric structure, featuring bridging bromide ligands, making each iron center 5-coordinate.

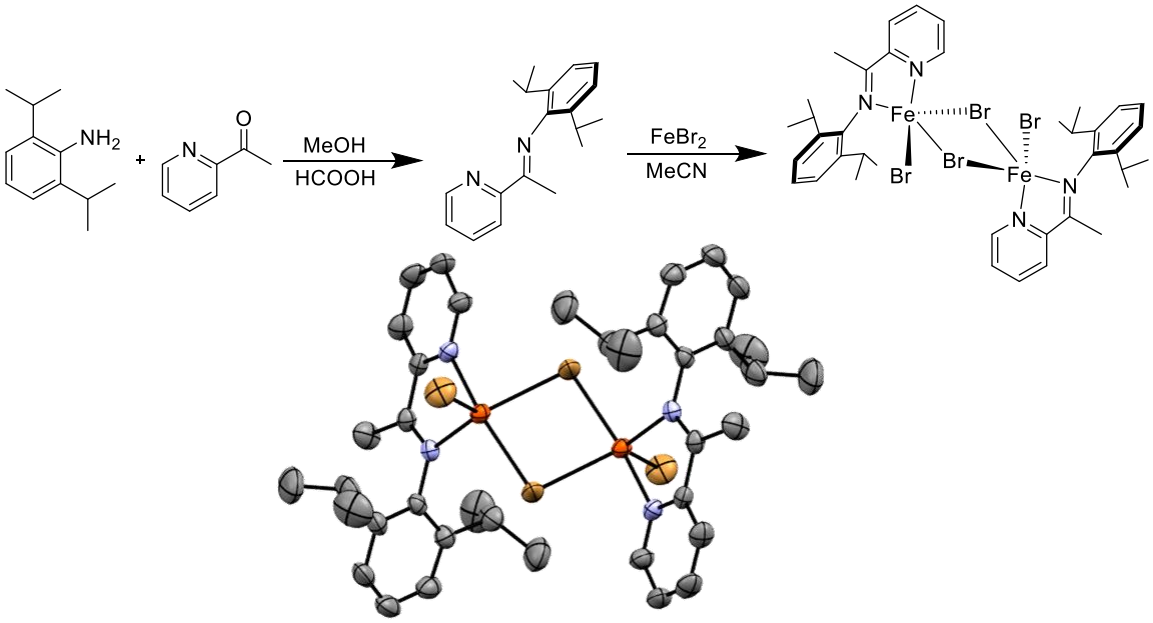

Figure 3.2.1. Synthesis of **L2** followed by metalation by $FeBr_2$ with the associated ORTEP view of **2FeBr$_2$**, the metallated complex, featuring a dimeric structure with bridging halides.

Reacting **[2FeBr$_2$]$_2$** with excess sodium amalgam, under an atmosphere of carbon monoxide in CH_2Cl_2 reveals a color change from red/purple to dark blue. After stirring for 48 hours, the solvent was removed *in vacuo* and the resultant blue solid was dissolved in Et_2O and filtered through celite to remove any mercury contamination. ATR-IR analysis of the blue product shows two vibrations assigned as ν_{CO} at 1984 and 1900 cm^{-1} with a shoulder around 1875 cm^{-1}, however, the transmission IR spectrum in Et_2O shows three distinct ν_{CO} at 2009, 1945, and 1930 cm^{-1}. This result indicates that the expected dicarbonyl species was not isolated, but instead a $Fe(CO)_3$ unit. The Et_2O solution was allowed to evaporate, leaving large, dark blue crystals of **2Fe(CO)$_3$**, suitable for X-ray diffraction.

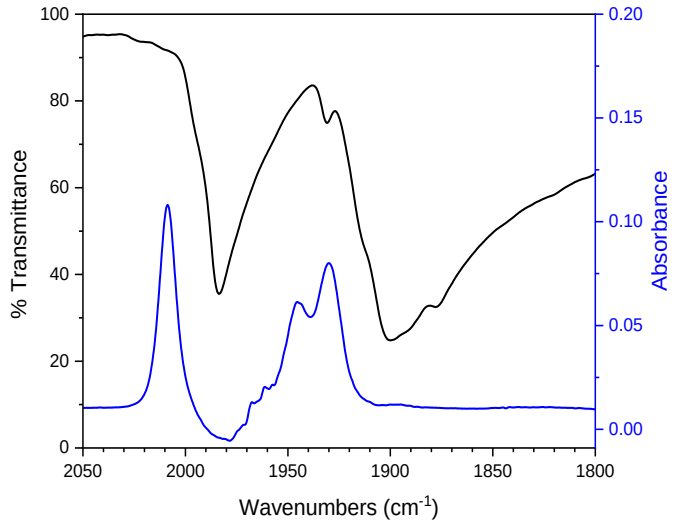

Figure 3.2.2. Solid state (ATR) IR spectrum of **2Fe(CO)$_3$** (black) with transmission IR of**2Fe(CO)$_3$** in Et_2O (blue).

The ORTEP of **2Fe(CO)$_3$** shows an iron center coordinated by one MIP ligand and three carbonyls, forming a slightly distorted trigonal bipyramid (τ_5 = 0.93) (τ_5 = 1 is trigonal bipyramidal and = 0 is square pyramidal) with the pyridine nitrogen and one carbonyl ligand in the axial position. The average CO bond length is 1.149 Å, slightly elongated from that of free CO (1.128 Å), and the average Fe-C(O) bond is 1.786 Å. These bonds are similar to what is observed in the dicarbonyl, **1Fe(CO)$_2$**, which features an average CO bond length of 1.155 Å and an average Fe-C(O) bond length of 1.783 Å. The N_{imine}-C_{imine} bond distance for **2Fe(CO)$_3$** is 1.323 Å and the C_{imine}-$C_{pyridine}$ bond length is 1.427 Å, 0.035 Å longer and 0.056 Å shorter than that of **[2FeBr$_2$]$_2$**, respectively. The elongation of the N_{imine}-C_{imine} and the shortening of the C_{imine}-$C_{pyridine}$ bonds show that the ligand is participating in the reduction.

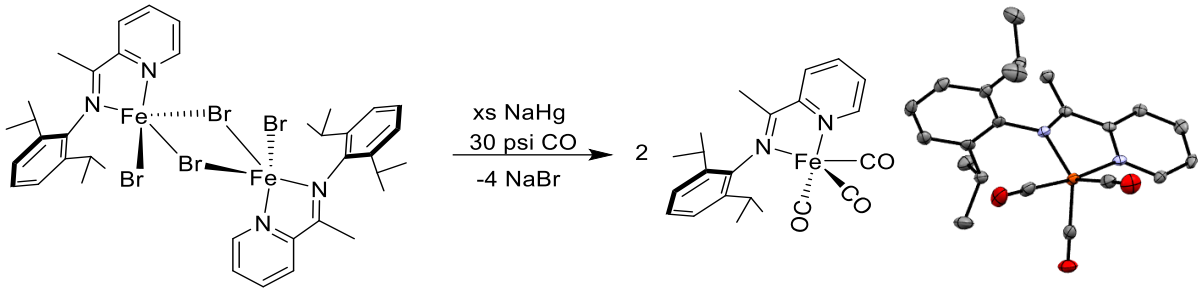

Figure 3.2.3. Synthesis and ORTEP image of **2Fe(CO)$_3$**.

The Mössbauer spectrum of **2Fe(CO)$_3$** (**Figure 3.2.4**) shows an isomer shift (δ) of -0.090 mm/s and a quadrupole splitting (ΔE_Q) of 1.912 mm/s. The isomer shift is similar to that of the two-electron reduced **1Fe(CO)$_2$** (δ = -0.089 mm/s), though the increased symmetry of **1Fe(CO)$_2$** gives a ΔE_Q of 1.197 mm/s. The formal oxidation assignments of **1Fe(CO)$_2$** have been determined as L^{2-}–Fe^{2+},[64] however, the presence of only a single imine in **2Fe(CO)$_3$** coupled with an additional carbonyl ligand makes the oxidation state assignment ambiguous. The nearly identical isomer shifts of **1Fe(CO)$_2$** and **2Fe(CO)$_3$** are unexpected if the formal assignment is Fe^{2+} for the latter complex given that the third carbonyl ligand should result in a significantly more oxidized iron center. More work will need to be conducted, including computations, to confidently assign formal oxidation states to the ligand and metal in **2Fe(CO)$_3$**, therefore, for simplicity it has been assumed that the complex is simply a two electron donor in the nitrite reduction reaction.

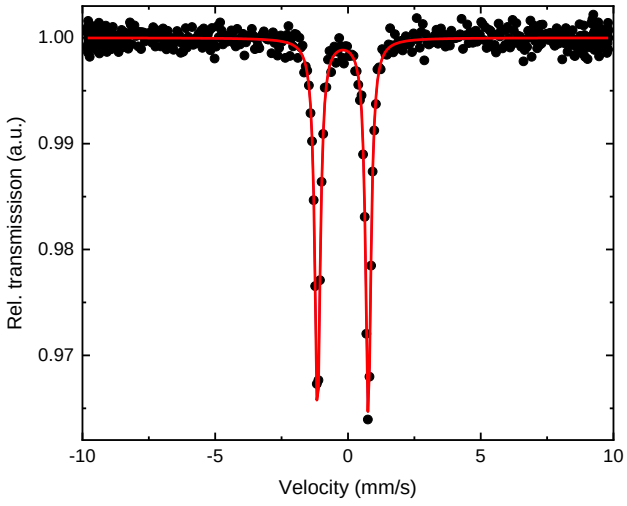

Figure 3.2.4. Zero-field Mössbauer spectrum of **2Fe(CO)$_3$.** Fitting parameters: Isomershift (δ) -0.090 mm/s; Quadrupole splitting (ΔE_Q) 1.912 mm/s; Line width (r) 0.25 mm/s.

The CV of **2Fe(CO)$_3$** in MeCN shows an irreversible reduction at -1.43 V as well as an irreversible oxidation at -0.49 V. The oxidation is roughly twice the area of the reduction, likely indicating that it is a two-electron process, which presumably liberates the CO ligands.

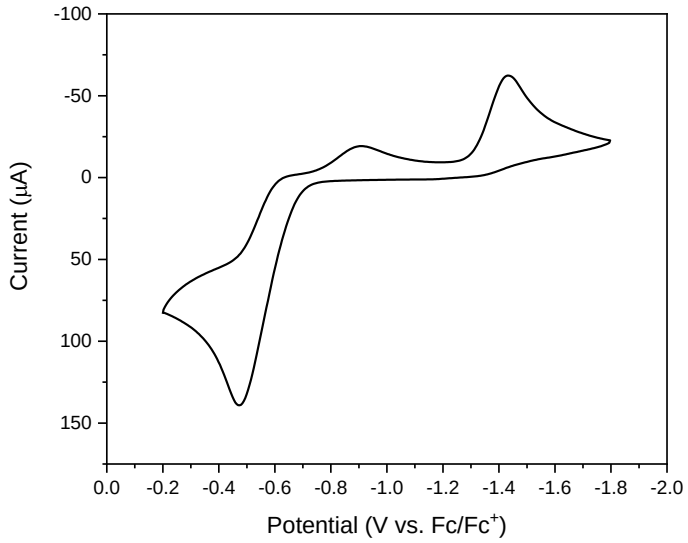

Figure 3.2.5. CV of **2Fe(CO)$_3$** (10 mM) in MeCN, glassy carbon working electrode, platinum wire counter electrode, 0.1 M $TBAPF_6$ supporting electrolyte.

Attempts to isolate **2Fe(CO)$_3$** as a dicarbonyl iron complex were carried out using SmI_2 in THF as a reductant and adding stoichiometric amounts of CO gas (2 CO per iron) to the reduction of **[2FeBr$_2$]$_2$**. The dicarbonyl species, we reasoned, would be more reactive and could lead to room temperature nitrate reduction. IR of a THF solution of the product, however, showed one υ_{CO} at 1859 cm^{-1}. The presence of a single υ_{CO} hinted at the formation of a mono-carbonyl species which was later confirmed by single-crystal XRD; the ORTEP shows an homoleptic iron mono-carbonyl, $^{Ar}MIP_2Fe(CO)$ (**2$_2$Fe(CO)**), which represents loss of half of the original iron to an undetermined species. The structure of the complex is reminiscent of a highly distorted porphyrin due to the N coordination mode; however, the metal center is nearly trigonal bipyramidal (τ_5 = 0.65, where τ_5 = 0 is square pyramidal). Efforts to further understand this new complex will be continued, including assignment of formal oxidation states of the iron and MIP ligands, as well as exploring the reactivity towards nitrogen reduction.

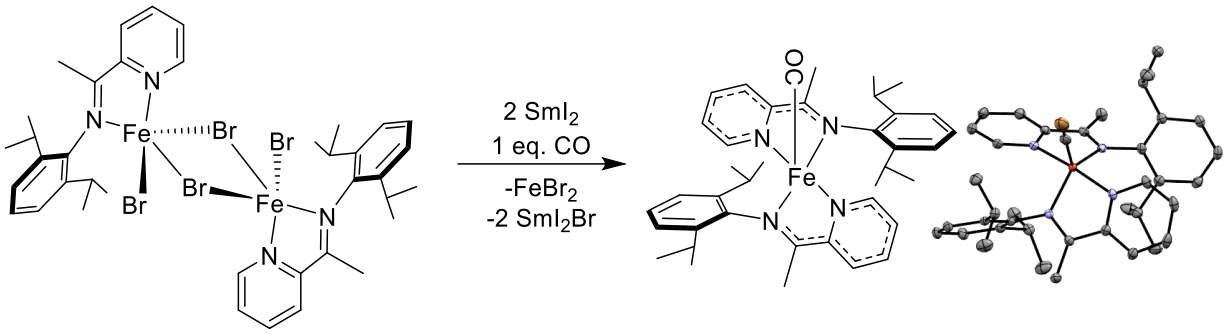

Figure 3.2.6. Synthesis and ORTEP view of **2_2Fe(CO)**.

With the understanding that **2Fe(CO)$_3$** is a two electron reduced iron complex, it was reasoned that it should be capable of similar reduction chemistry. Addition of 2 equivalents of nitrite and 4 equivalents of acid to a MeOH solution of **2Fe(CO)$_3$** resulted in loss of the blue color and formation of a reddish-brown precipitate. The precipitate was collected via filtration and washed with MeOH. The ATR-IR spectrum of the solid shows two strong vibrations at 1694 and 1646 cm^{-1} which shift to 1661 and 1612 cm^{-1} when the reaction is repeated using $^{15}NO_2^-$, confirming the identity as ν_{NO} (**Figure S3**). The solid was then dissolved in CH_2Cl_2 and pentane was diffused into the concentrated solution, giving dark red-brown crystals suitable for X-ray diffraction in a 35% yield, identified as **2Fe(NO)$_2$**. The ORTEP of **2Fe(NO)$_2$** shows an approximately tetrahedral DNIC (τ_4 = 0.89) in the MIP ligand scaffold. The N_{imine}-C_{imine} and C_{imine}-$C_{pyridine}$ bond lengths are 1.293 and 1.479 Å, respectively, indicating that the ligand is in the neutral oxidation state. Both nitrosyl ligands have a N-O bond length of 1.192 Å, elongated 0.04 Å from that of free nitric oxide (1.152 Å). The average Fe-N(O) bond is 1.648 Å. These bonds are in line with what is observed in compounds **4Fe(NO)$_2$** and **1Fe$_2$(NO)$_4$**, which are assigned as $\{Fe(NO)_2\}^{10}$ complexes. The isolation of a neutral $\{Fe(NO)_2\}^{10}$ from the reaction with nitrite was an unexpected result as the same reaction with the PDI-based complexes results in the formation of a cationic $\{Fe(NO)_2\}^9$ complex. The reason for this result is not currently understood, however, it potentially ties to the instability of the cationic, four-coordinate DNICs.

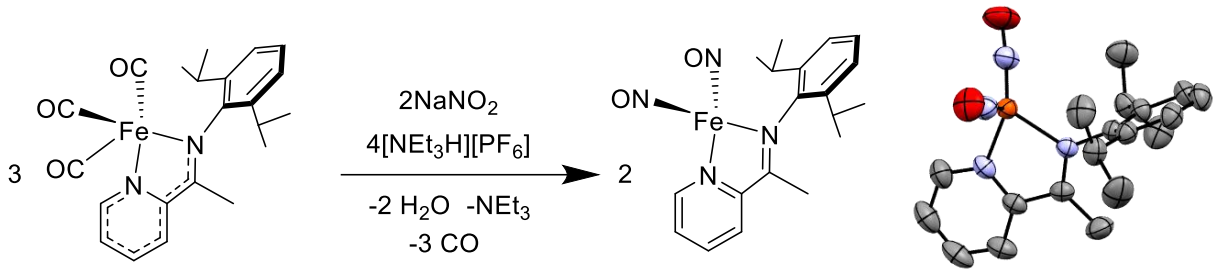

Figure 3.2.7. Nitrite reduction by **2Fe(CO)$_3$** to form complex **2Fe(NO)$_2$** with associated ORTEP.

Complex **2Fe(NO)$_2$** could also be synthesized via a secondary method by combining the free MIP ligand with $Fe(NO)_2(CO)_2$ in a one-to-one ratio in THF. This method gives the product in an 80% yield and is significantly more efficient than the synthesis through reduction of nitrite to nitrosyl.

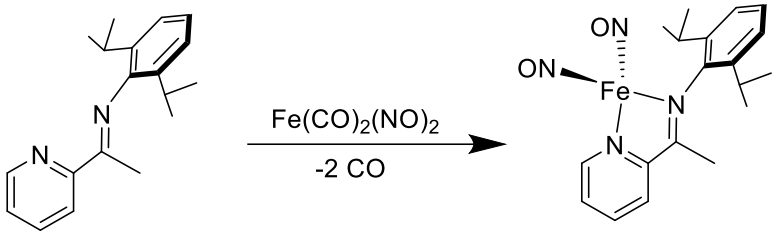

Scheme 3.2.1. Direct synthesis of **2Fe(NO)$_2$** via $Fe(CO)_2(NO)_2$.

The CV of **2Fe(NO)$_2$** in MeCN shows two reversible events at -0.4892 and -1.8439 V, respectively, the former belonging to the $\{Fe(NO)_2\}^{9/10}$ redox couple while the latter belongs to the reduction of the MIP scaffold; the OCP was -0.87 V. The results of this experiment are similar to that of the other DNICs that have been synthesized in the PDI ligand scaffold. The CV data of **2Fe(NO)$_2$** showed that the oxidized $\{Fe(NO)_2\}^9$ complex was potentially stable, and work was carried out to investigate this new compound.

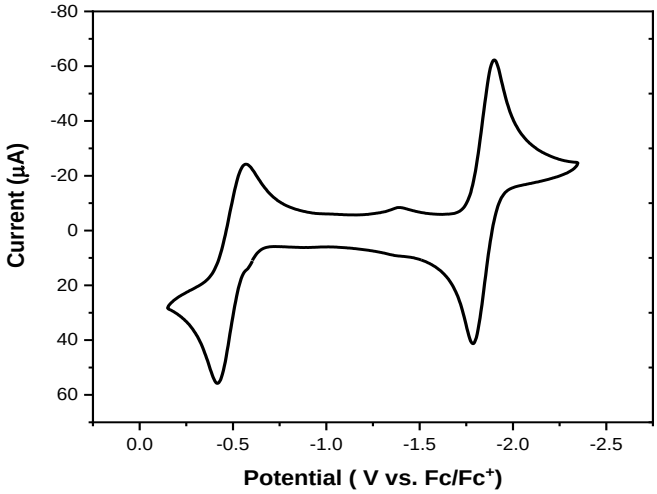

Figure 3.2.8. Cyclic Voltammogram of **$2Fe(NO)_2$** (5 mM) in MeCN, glassy carbon working electrode, platinum wire counter electrode, 0.1 M $TBAPF_6$ supporting electrolyte.

A solution of **$2Fe(NO)_2$** in CH_2Cl_2 was combined with one equivalent of $FcPF_6$ and allowed to stir overnight. The solution was then filtered through a celite plug and layered with Et_2O, yielding X-ray quality crystals of **$[2Fe_2(NO)_4(PF_4)][PF_6]$**. The IR spectrum of **$[2Fe_2(NO)_4(PF_4)][PF_6]$** shows three distinct ν_{NO} at 1839, 1757, and 1699 cm^{-1} which shift to 1795, 1723, and 1667 cm^{-1} when labeled with ^{15}N (**Figure S8**). The significant hypsochromic shift of the ν_{NO} suggest that the iron-nitrosyl unit has been oxidized by one electron to the $\{Fe(NO)_2\}^9$ complex. The appearance of a third nitrosyl stretch would also lead to the conclusion that the symmetry of the metal has changed, which is confirmed by the single-crystal XRD structure.

The crystal structure of **$[2Fe_2(NO)_4(PF_4)][PF_6]$** shows a dimeric complex featuring a bridging PF_4^- (tetrafluorophosphite), which presumably resulted from a decomposed PF_6^- anion. The average N-O bond is 1.168 Å, 0.024 Å shorter than that of **$2Fe(NO)_2$**, indicative of less electron donation from the metal. While the N_{imine}-C_{imine} and C_{imine}-$C_{pyridine}$ bonds do contract and elongate, respectively, the change is not significant, indicating that the MIP scaffold remains neutral, much as expected. The bridging PF_4^- has an average P-F bond distance of 1.48 Å, while the free PF_6^- shows longer P-F contacts with an average of 1.60 Å. The molecular geometry of the PF_4^- is highly distorted from the of the free anion, with τ_4 = 0.92 compared to $\tau_{4(\text{free anion})}$ = 0.65.[65]

Another variant of the oxidized **2Fe(NO)$_2$** can be isolated through the use of a different counterion, in the case of $FcBF_4$, **[2Fe(NO)$_2$][BF$_4$]** can be isolated through the same methods as . The ORTEP view of **[2Fe(NO)$_2$][BF$_4$]** shows two stereoisomers of a five-coordinate DNIC with a BF_4^- bound to the iron through a bridging F atom either anti to the pyridine or imine N atoms. The N_{imine}-C_{imine} and C_{imine}-$C_{pyridine}$ bonds as well as the N-O bond lengths are virtually indistinguishable from those of **[2Fe$_2$(NO)$_4$(PF$_4$)][PF$_6$]**.

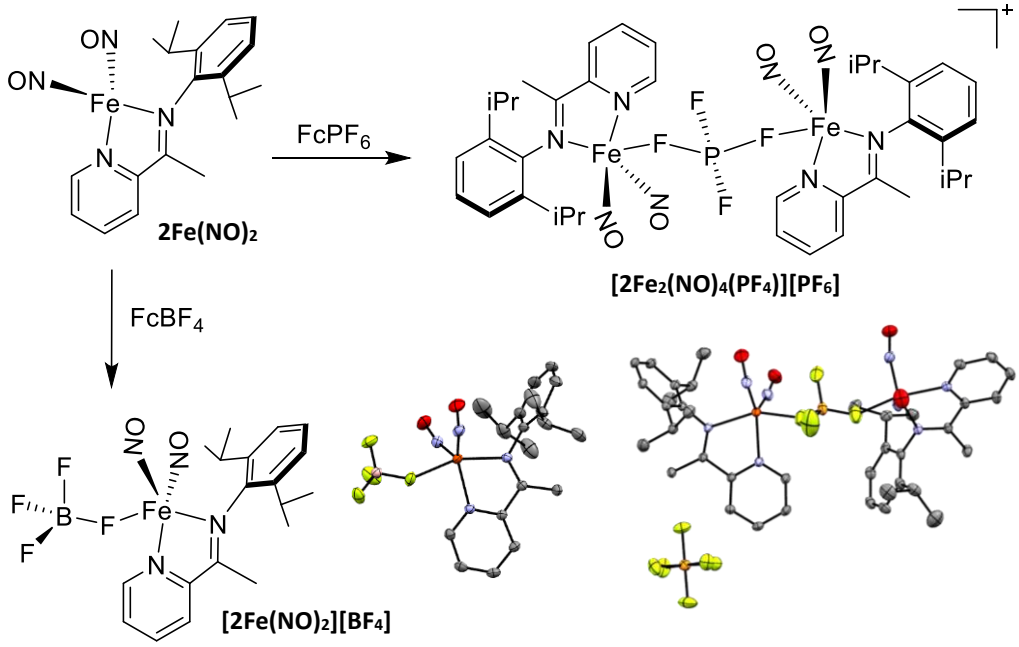

Figure 3.2.9. Oxidation of **2Fe(NO)$_2$** by ferrocenium with differing counterions to form **2Fe(NO)$_2$(BF$_4$)** (down) and **[2Fe$_2$(NO)$_4$(PF$_4$)][PF$_6$]** (right) with their associated ORTEP images.

3.3 Synthesis and Characterization of Mono-Imine DNIC

Synthesis of the Schiff-Base ligand of **3Fe(NO)$_2$** was carried out via reaction of 3-pentanone with one equivalent of 1-(2-aminoethyl) pyrrolidine heated in an oil bath under nitrogen for 24 hours. The product was then distilled under reduced pressure, discarding the initial distillates, to afford the product ^{Pyrrol}Imine (**L3**) as a light-yellow oil confirmed by IR ($\nu_{C=N}$: 1665 cm^{-1}) and NMR (**Figure S24**). This pure ligand is then added to one equivalent of $Fe(NO)_2(CO)_2$ in THF and allowed to stir for 2 hours. The reaction mixture is concentrated and passed through a neutral alumina plug before being layered with pentane to yield crystalline **3Fe(NO)$_2$**.

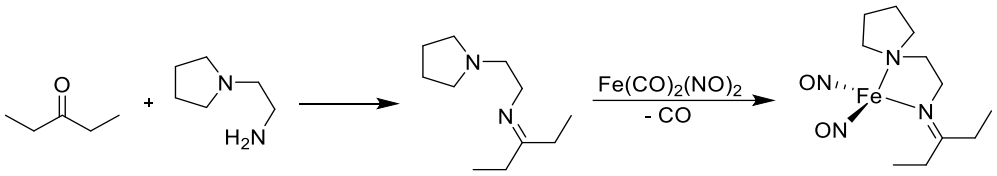

Scheme 3.3.1. Synthesis of the Schiff-Base complex **3Fe(NO)$_2$**.

The IR spectrum of **3Fe(NO)$_2$** shows two ν_{NO} at 1690 and 1638 cm^{-1} in THF. Oxidation of the complex by $FcPF_6$ in THF results in a hypsochromic shift to 1819 and 1749 cm^{-1}, respectively. The PF_6^- salt, **[3Fe(NO)$_2$][PF$_6$]**, was isolated by slow diffusion of Et_2O into the THF solution. The CV of **3Fe(NO)$_2$** shows one event, a $\{Fe(NO)_2\}^{9/10}$ redox couple, centered at -0.517 V, almost identical to that of **2Fe(NO)$_2$**, however, lacking the MIP ligand reduction event at -1.84 V.

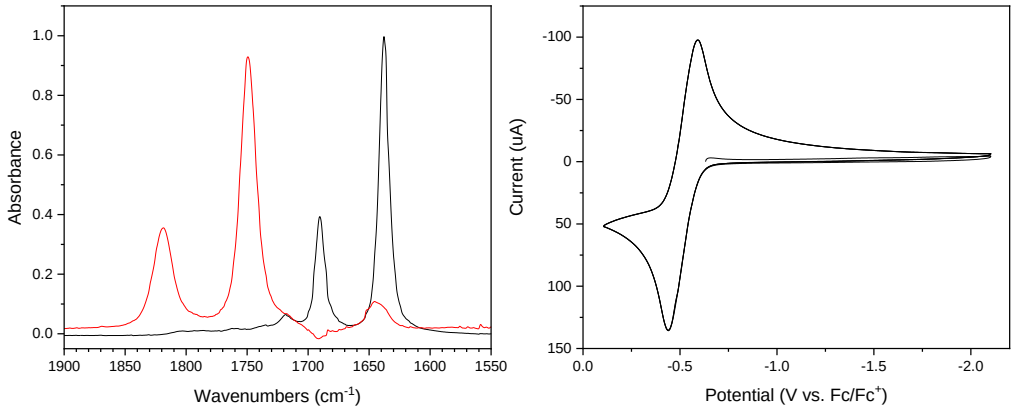

Figure 3.3.1. Transmission IR spectra of **3Fe(NO)$_2$** (black) and **[3Fe(NO)$_2$][PF$_6$]** (red) in THF and CV of **3Fe(NO)$_2$** (10 mM) in MeCN, glassy carbon working electrode, platinum wire counter electrode, 0.1 M $TBAPF_6$.supporting electrolyte.

The ORTEP views of **3Fe(NO)$_2$** and **[3Fe(NO)$_2$][PF$_6$]** show tetrahedral (τ_4 = 0.91 and 0.90), N,N coordinated DNICs. The N-O bond length shortens, as expected, upon oxidation from 1.192 Å in **3Fe(NO)$_2$** to 1.162 Å in **[3Fe(NO)$_2$][PF$_6$]**. The isolation of **[3Fe(NO)$_2$][PF$_6$]** is unprecedented as cationic four-coordinate DNICs are considered to be highly unstable[26] as observed by the decomposition of

[3Fe(NO)$_2$][PF$_6$] over several weeks, even in the solid state. Attempts to isolate **[3Fe(NO)$_2$]$^+$** with a more-coordinating BF_4^- counterion for better stability were unsuccessful.

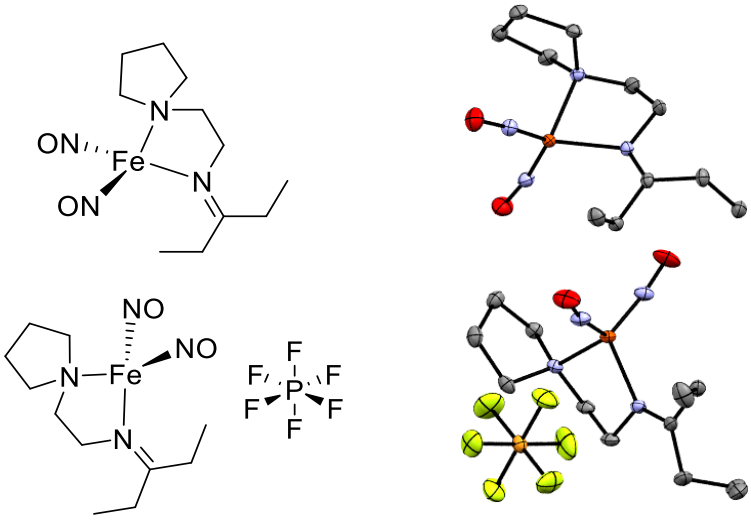

Figure 3.3.2. ChemDraw and ORTEP views of **3Fe(NO)$_2$** (top) and **[3Fe(NO)$_2$][PF$_6$]** (bottom).

3.4 Mono-Nuclear PDI {Fe(NO)$_2$}^{10} Synthesis and Characterization

The cationic {Fe(NO)$_2$}^{9} complex [^{DIDPA}Fe(NO)$_2$][PF$_6$] (**[5Fe(NO)$_2$]$^+$**) was characterized previously by our group.[41] As with the other cationic DNICs, **[5Fe(NO)$_2$]$^+$** can be reduced by one electron to form the neutral, four-coordinate {Fe(NO)$_2$}^{10} complex, **5Fe(NO)$_2$**. Reaction of **[5Fe(NO)$_2$]$^+$** with one equivalent of cobaltocene in DCM resulted in an immediate color change from brown to red. The product could then be crystallized by evaporation of a concentrated Et_2O solution to yield dark, red-brown, X-ray quality crystals.

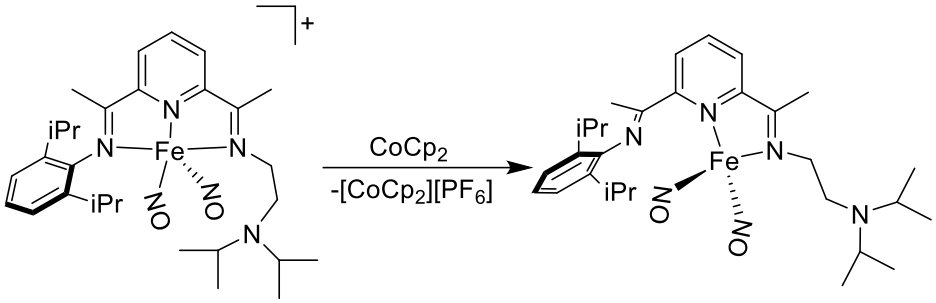

Scheme 3.4.1. One electron reduction of **[5Fe(NO)$_2$][PF$_6$]** to form **5Fe(NO)$_2$**.

The ATR-IR spectrum of **5Fe(NO)$_2$** shows a bathochromic shift of approximately 91 cm^{-1} in the ν_{NO} as well as a significant narrowing of the $\Delta\nu_{NO}$ (from 72 to 51 cm^{-1}) indicating a change in geometry of the Fe(NO)$_2$ unit from square pyramidal to approximately tetrahedral. Upon labeling of the nitrosyls with ^{15}N the stretching frequency shifts 34 cm^{-1} (calculated 33 cm^{-1}), confirming their identity.

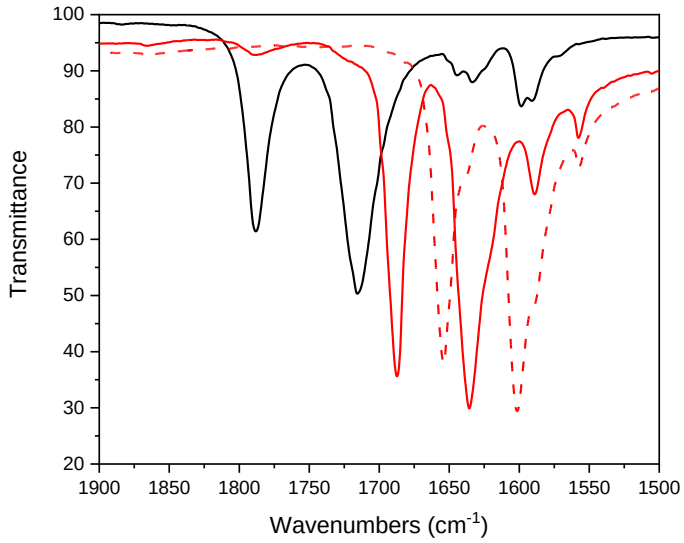

Figure 3.4.1. Nitrosyl stretches of **[5Fe(NO)$_2$]$^+$** (black) and **5Fe(NO)$_2$** (red) with **5Fe(^{15}NO)$_2$** shown by a red, dashed line.

The ORTEP view of **5Fe(NO)$_2$** shows a single iron center best described as trigonal pyramidal (τ_4 = 0.87, where 0.85 is pure trigonal pyramid and τ_4 = 1 is tetrahedral). The average NO bond increases 0.038 Å while the average Fe-N(O) bond shortens 0.036 Å from that of **[5Fe(NO)$_2$]$^+$**. The C_{imine}-N_{imine} bonds remain

almost identical (Δ 0.004 Å) between the two complexes and the C_{imine}-$C_{pyridine}$ bonds lengthen slightly (0.016 Å) in **5Fe(NO)$_2$**. As with the complexes described previously, the crystallographic data indicates that the reduction is best described as metal-centered with the ligand remaining in the neutral form.

Oxidation of **5Fe(NO)$_2$** by one equivalent of ferrocenium hexafluorophosphate resulted in the reformation of **[5Fe(NO)$_2$]$^+$** with no release of any nitrogen species into the reaction headspace.

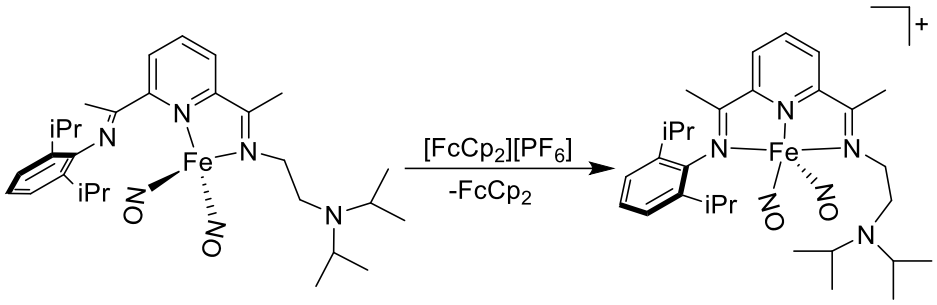

Scheme 3.4.2. One electron oxidation of **5Fe(NO)$_2$** to form **[5Fe(NO)$_2$][PF$_6$]** .

3.5 Conclusions and Future Work

Both the ^{Ar}MIP (**L2**) and ^{Pyrrol}Imine (**L3**) ligands form novel complexes with iron, both as iron carbonyl adducts as well as DNICs. The pyridine mono-imine, **L2,** demonstrates modularity in coordination between the single chelate **2Fe(CO)$_3$** and the homoleptic **2$_2$Fe(CO)**, the latter of which features a highly activated carbonyl, with a stretching frequency roughly 40 cm^{-1} lower than that of **2Fe(CO)$_3$**. The ^{Ar}MIP ligand features similar redox activity to that of the PDI complexes, though, its capabilities have yet to be fully explored; other reduction reactions could be possible given the more open coordination around the metal center, not only with iron but other metal centers as well.

The DNICs formed in the ^{Ar}MIP scaffold behave as classical complexes and form five-coordinate {Fe(NO)$_2$}^{9} DNICs where the ^{Pyrrol}Imine ligand is able to adopt an unusual four-coordinate geometry. This reactivity is poorly understood at this time, however, more work with similar Schiff-Bases could highlight

the role of sterics in these reactions. Modification of the ^{Ar}MIP ligand at the 6 position of the pyridine with bulky groups could lead to similar activity to that of the ^{Pyrrol}Imine when forming the $\{Fe(NO)_2\}^9$ DNICs. The research of these ligands is still in its infancy and work will be continued to discover new and exciting reactivity.

4.1 Photochemical CO Release by Glycol Complexes

The ability to isolate highly reduced complexes such as **1Fe(CO)$_2$**, which are then able to facilitate reduction reactions is dependent on the use of electron withdrawing substituents, in this case CO, to stabilize the intermediate two-electron reduced complex. Carbon monoxide is highly stabilizing due to is ability to act as a π-acceptor, however, this increase in stability has the cost of the complex then acting as a weaker reductant as well as the CO ligands taking two potential binding sites for substrate. Because of these obstacles reducing more difficult nitrogen oxides such as nitrate and nitrous oxide remain a challenge for iron-PDI systems. We rationalized that photochemical release of CO by use of a more labile secondary-sphere interaction could lead to activation of a more diverse set of substrates.

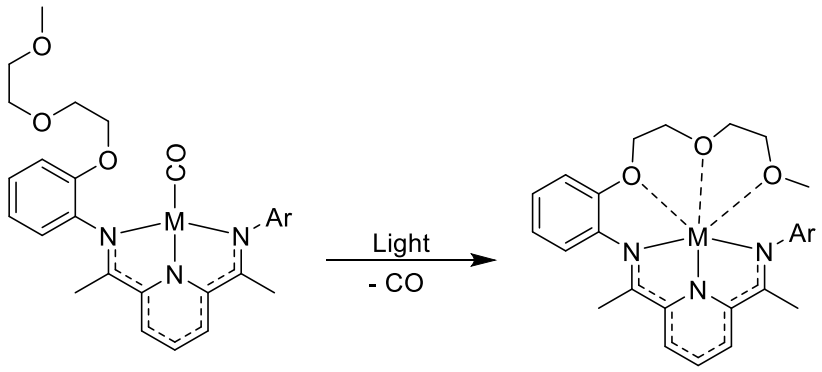

Scheme 4.1.1. Generic scheme showing CO release by light with a pendant glycol protecting a reduced metal center.

Photolysis reactions were carried out in 25 mL quartz side-arm flasks inside of a mercury lamp light box (λ_{max} = 365). Initial photolysis reactions were carried out using the previously described dicarbonyl complex, **5Fe(CO)$_2$**.[66] In anhydrous THF, **5Fe(CO)$_2$** was dissolved and loaded into a quartz side-arm flask sealed with a Teflon stopper. This solution was then freeze-pump-thawed three times to remove any dissolved gasses. The tube was then irradiated for 2 hours at room temperature without stirring. The headspace was analyzed by gas-phase IR which showed liberation of CO gas. With this positive control, work was undertaken to synthesize complexes with glycols in the secondary coordination sphere.

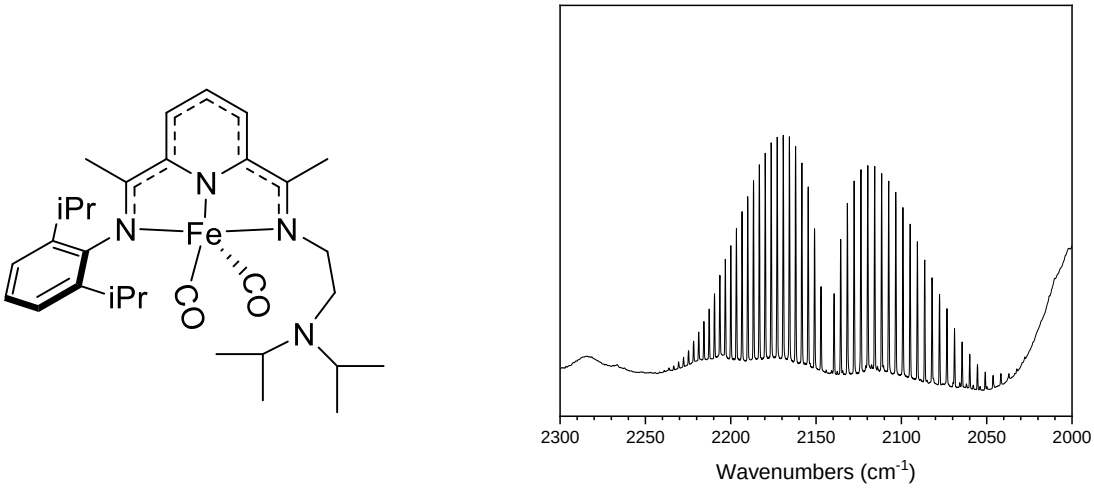

Figure 4.1.1. Headspace after photolysis of **5Fe(CO)$_2$** showing release of CO with chemdraw (left).

Pendant glycol **PEG4** was synthesized by first tosylating tetraethylene glycol monomethyl ether with para-toluenesulfonyl chloride in THF. This product was then reacted with 2-nitrophenol to produce the tetraethylene glycol-2-nitrobenzene. To remove the nitro group, reduction was carried out using 5% palladium on carbon under 40 psi of hydrogen in EtOH to yield the free amine which could then be condensed on to the PDI ligand scaffold via metal-templated Schiff-Base condensation. The resultant blue complex, ^{PEG4}PDIFeBr$_2$ (**6FeBr$_2$**) could then be reduced by sodium amalgam under 30 psi of CO gas to yield the two-electron reduced **6Fe(CO)$_2$**. **6Fe(CO)$_2$** was finally purified via neutral alumina column and eluted with THF/Pentane (70:30). The final product was isolated as a green oily solid and characterized via ^{1}H NMR, as single crystals suitable for XRD have yet to be isolated.

Photolysis of **6Fe(CO)$_2$** in Et$_2$O for several hours did not result in the loss of CO as it did with **5Fe(CO)$_2$**. Instead, the complex was found to be stable to UV irradiation. The ATR-IR of the solid after irradiation showed no loss of υ_{CO} intensity. This result was unexpected and highlight that secondary-sphere interactions likely play a role in CO ligand lability.

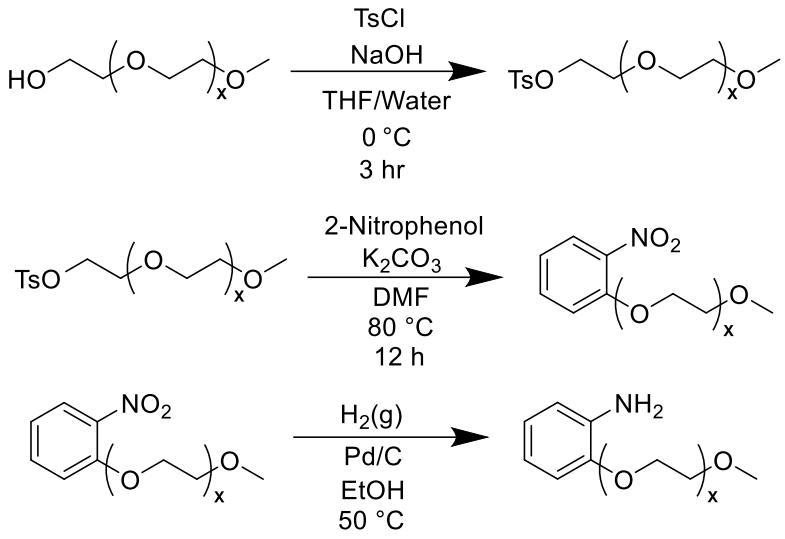

Figure 4.1.2. Synthesis of a generic glycol which can be added to the PDI ligand scaffold through a metal templated condensation.

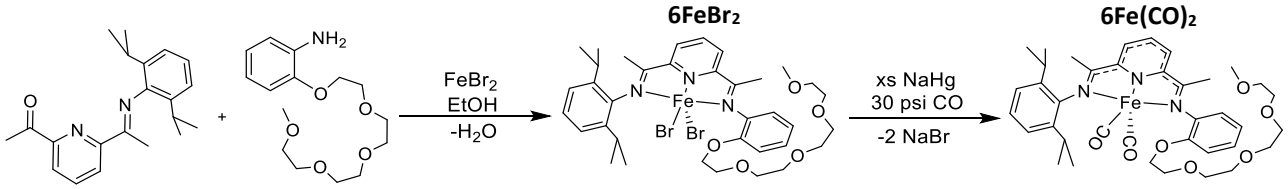

Scheme 4.1.3. Metal-templated Schiff-Base condensation to form complex **$6FeBr_2$** followed by reduction by NaHg under CO to form **$6Fe(CO)_2$**.

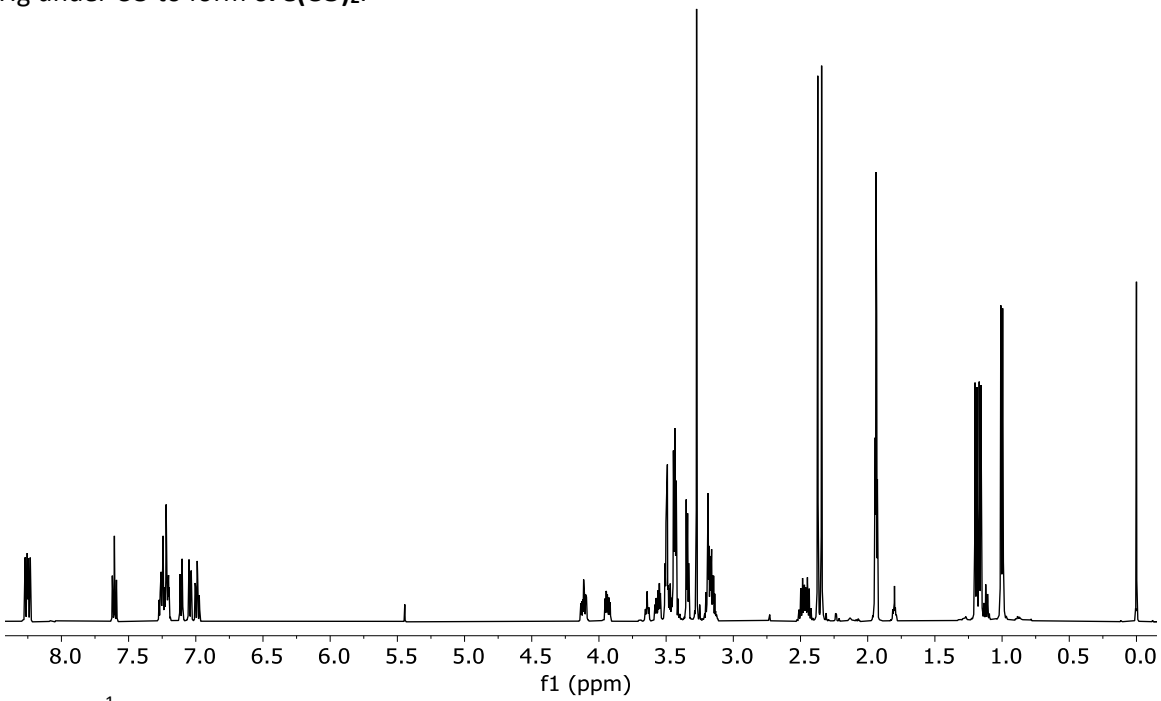

Figure 4.1.2. ^{1}H NMR (500 MHz) spectrum of **$6Fe(CO)_2$** in CD_3CN, internally referenced to TMS.

4.2 Glycol Salt Binding Studies

In previous work, our group demonstrated that crown-ethers in the secondary-sphere were able to bind Lewis-acids such as sodium (in a 15-crown-5-ether).[40] That work showed that Na^+ binding in a benzo-15-crown-5-ether was quite strong ($K_{Na^+} > 10^5\ M^{-1}$) with a essentially negligible 50 mV shift in the E ½ of the complexes CV. The net result was enhancement of the initial rate of nitrite reduction which was presumed to be due to the electrostatic interaction of the Lewis-acid and the nitrite anion effectively luring substrate into the active site.

Given the success of the benzo-15-crown-5 complex we reasoned that it would be possible to conduct similar chemistry with complexes like **6Fe(CO)₂** with a glycol that could form an *in situ* crown-ether type interaction with Lewis-acids that could perform two functions, 1) the glycol could interact with the metal center effectively blocking it from binding substrate until a Lewis-acid was introduced to open the active site and 2) the glycols could then act as the crown-ether did in previous work to enhance the rate of reaction with small molecules.

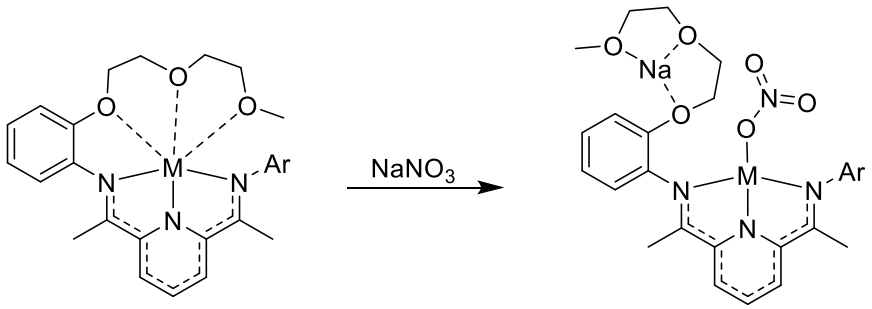

Scheme 4.2.1. An example of the predicted behavior of a reduced, glycol protected complex in the presence of a target molecule.

To test the ability of Lewis-acid binding ^{1}H NMR salt-binding studies were conducted with the PEG_4 glycol **6Fe(CO)₂** as well as the PEG-3 glycol, ^{PEG3}PDIFe(CO)$_2$ (**7Fe(CO)₂**). NMR titrations of the two complexes were conducted in CD_3CN with $NaPF_6$ and $LiBPh_4$ for **6Fe(CO)₂** and **7Fe(CO)₂** respectively. The salts were titrated into J-young NMR tubes with a known amount of complex in approximately 0.1 molar equivalent

injections. After each injection, an NMR spectrum was collected, monitoring the downfield shift of the glycol protons caused by the electron-withdrawing Na^+ or Li^+. Unfortunately, the binding studies showed an exceptionally weak interaction between the glycols and the cations. This lead to the BindFit software used to calculate binding constants to fail to give any valid solutions for a one-to-one, host-guest interaction. Although the glycol complexes failed to show strong interaction with Lewis-acids in solution, there are other complexes such as a pendant 15-crown-5-ether that we know have strong interactions with the target molecules. These complexes have been synthesized by our group previously and will be studied for this type of chemistry in future works.

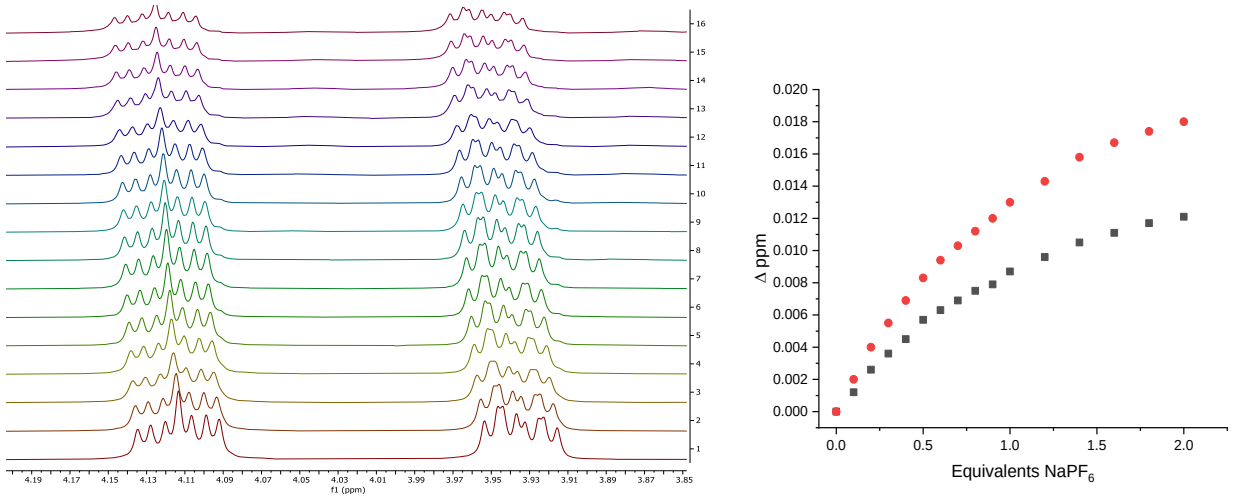

Figure 4.2.1. NMR salt binding study of **6Fe(CO)$_2$** with $NaPF_6$ in CD_3CN, plot on right represents the change in chemical shift (ppm) of selected glycol protons due to the introduction of Na^+. BindFit calculates a 1:2 binding with $K_{Na^+} = 139\ M^{-1}$.

4.3 CO Capture and Release on Iron

Reduction of CO_2 emissions to fight climate change is a major focus of many groups. Often reduction is meant in the context of redox reactions, with the intent of recycling the carbon into useful synthetic materials through chemistry such as Fischer-Tropsch synthesis of alkanes.[67,68] Our group has demonstrated ligand based, chemical reduction of CO_2 along with subsequent release of CO, regenerating the starting material,[69] however, we have yet to demonstrate this electrochemically. Iron PDI complexes

such as **1Fe(CO)$_2$** are desirable candidates because of our ability to isolate and fully characterize the starting and ending materials.

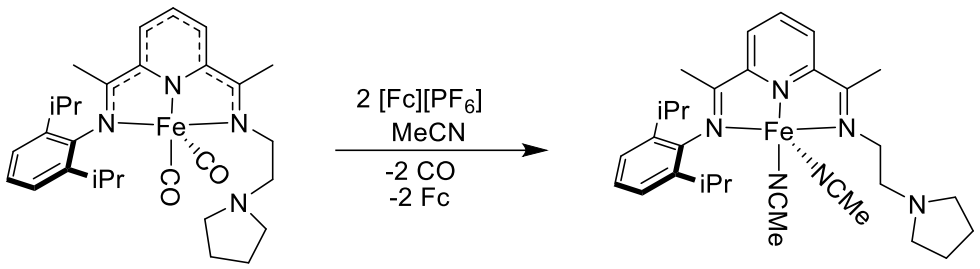

Scheme 4.3.1. Two electron oxidation of **1Fe(CO)$_2$** to form **1Fe(PF$_6$)$_2$**.

Chemical isolation of [^{Pyrrol}PDIFe(MeCN)$_2$][PF$_6$]$_2$ (**1Fe(PF$_6$)$_2$**), was carried out by oxidation of **1Fe(CO)$_2$** by two equivalents of FcPF$_6$ in MeCN. Upon addition of the oxidant to a MeCN solution of **1Fe(CO)$_2$** a color change from dark green to red was observed along with vigorous bubbling. The IR of the red product shows the disappearance of the υ_{CO} of **1Fe(CO)$_2$** at 1952 and 1887 cm^{-1} indicating the release of the carbonyl ligands, accompanied by the appearance of a strong peak at 833 cm^{-1}, from PF$_6^-$ and two peaks indicative of bound MeCN at 2310 and 2275 cm^{-1}. Slow diffusion of Et$_2$O into a MeOH solution of **1Fe(PF$_6$)$_2$** yields purple, X-ray quality crystals of the (bis)hexafluorophosphate salt with one MeCN bound to the iron and one MeOH bound to the iron, engaged in a H-bond with the pyrrolidine ($N_{pyrrolidine}$-H_{MeOH} 1.699 Å). Shortening of the imine C=N bond from 1.328 Å of **1Fe(CO)$_2$** to 1.280 Å in **1Fe(PF$_6$)$_2$** indicates that the PDI scaffold is in its neutral oxidation state.

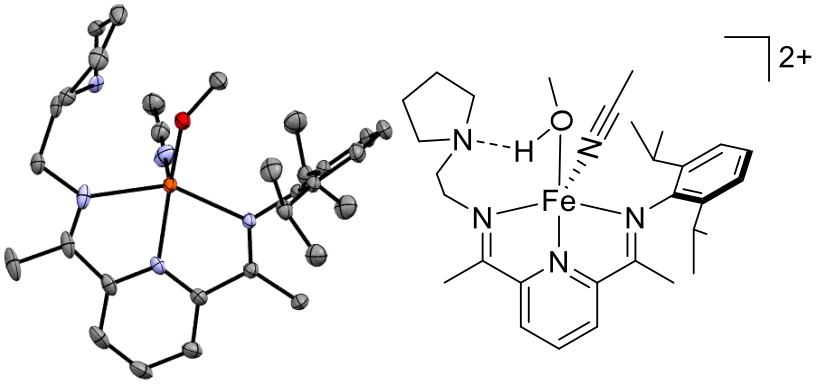

Figure 4.3.1. ChemDraw and ORTEP view of **1Fe(PF$_6$)$_2$**, both PF$_6^-$ counterions have been excluded for clarity. One MeCN has be exchanged for a MeOH from the crystallization solvent.

Once satisfied that the desired compound could be isolated chemically, work was undertaken to produce the same results electrochemically. In an electrochemical H-cell, **1Fe(CO)$_2$** was loaded into one side with a Pt mesh working electrode and a Ag|$AgNO_3$ reference. The other side of the cell was loaded with a large excess of sacrificial oxidant, $FcPF_6$, and a coiled Pt wire counter electrode. The two sides of the cell, separated by a fine glass frit, were filled with 0.1 M $TBAPF_6$ MeCN electrolyte solution to equal heights to slow diffusion of compound across the frit. A CV experiment was conducted to identify the potentials of the redox events of the complex versus the reference. An irreversible oxidation was identified at roughly -0.5 V, which is attributed to loss of CO. Bulk electrolysis (BE) was carried out at 0 V (versus reference). After 3 hours of BE, 3.7 C of charge had been passed representing oxidation of 76.3% of **1Fe(CO)$_2$** by equation **4.1**. The headspace of the cell was sampled for IR analysis and was found to contain CO gas, indicating the formation of **1Fe(PF_6)$_2$**.

$$mol = \frac{Charge\ Passed\ (C)}{96485\frac{C}{mol} \times \#\ electrons} \quad (\mathbf{4.1})$$

To demonstrate CO could be reversibly trapped by the complex, the reverse BE experiment was then conducted using **1Fe(PF_6)$_2$** as a starting material and ferrocene as a sacrificial reductant in the place of $FcPF_6$. An initial CV of the complex was collected followed by flushing of the headspace with CO for 10 minutes at a moderate flow rate. After the headspace was flushed another CV was collected with a new reduction at E ½ = -1.09 V (versus reference), corresponding to formation of a new complex. BE carried out at -1.4 V for 3 hours, passing 3.641 C (representing a faradaic yield of 67%) , which resulted in a color change from red to dark green. IR analysis of the solution after BE shows two vibrations at 1952 and 1887 cm^{-1}, assigned as υ_{CO} belonging to **1Fe(CO)$_2$**.

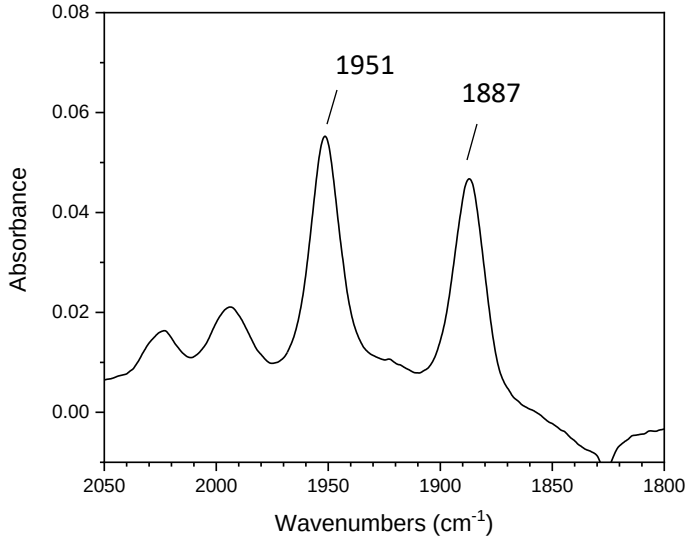

Figure 4.3.2. Transmission IR spectrum of cell solution after BE of **1Fe(PF$_6$)$_2$** under an atmosphere of CO in MeCN to form **1Fe(CO)$_2$** (ν_{CO}: 1951 and 1887 cm^{-1}).

Following the success of CO capture and release of **1Fe(PF$_6$)$_2$** and **1Fe(CO)$_2$** respectively, tests for CO_2 reduction were then conducted. A MeCN solution of **1Fe(PF$_6$)$_2$** was loaded into an H-cell. A CV of the solution was collected before and after sparging the cell headspace with CO_2, resulting in no change. BE was carried out on the CO_2 saturated solution at -2.0 V resulted in no formation of **1Fe(CO)$_2$** and no CO was detected in the cell headspace. Attempts to utilize a O atom acceptor to facilitate reactivity were conducted using TMSCl or $HNEt_3^+$, however, adverse side reactions in the former or proton reduction remain major obstacles to successful CO_2 reduction.

4.4 Urea Complexes for Nitrate Activation

The urea containing complex ^{EthylUrea}PDIFeBr$_2$ (**8FeBr$_2$**) was synthesized via metal templated condensation of 1-(2-aminoehtyl)-3-phenylurea with iron(II) bromide in anhydrous ethanol. The product is then dissolved in CH_2Cl_2 and filtered through celite. Diffusion of Et_2O into a concentrated DCM solution of **8FeBr$_2$** yielded X-ray quality blue crystals. A second pendant urea complex, ^{PhenylUrea}PDIFeBr$_2$ (**9FeBr$_2$**),

was also synthesized by the same method as **8FeBr₂** with a phenyl group in place of the ethyl linking the complex and urea group. A single crystal suitable for X-ray diffraction of **9FeBr₂** has not yet been grown.

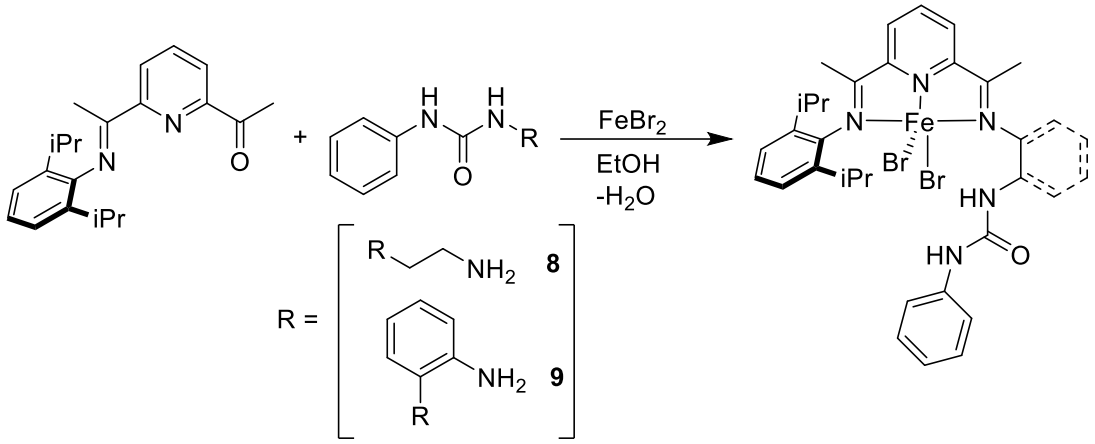

Scheme 4.4.1. Synthesis of the urea complexes **8FeBr₂** and **9FeBr₂**. The dashed ring shows **9FeBr₂**.

Both **8FeBr₂** and **9FeBr₂** can be reduced by excess NaHg under a CO atmosphere to isolate the respective direduced iron carbonyl complexes, **8Fe(CO)₂** and **9Fe(CO)₂**, respectively. A single crystal of **9Fe(CO)₂,** suitable for XRD was grown by slow evaporation of a concentrated Et_2O solution. The solid-state structure of **9Fe(CO)₂** features an average C_{imine}-N_{imine} bond distance of 1.365 Å as well as a C_{imine}-$C_{pyridine}$ bond distance of 1.397 Å, indicating the pyridine scaffold is in the direduced, 2-, state. This result is corroborated by the ^{1}H NMR spectra of **8Fe(CO)₂** and **9Fe(CO)₂**, both of which appear to be diamagnetic.

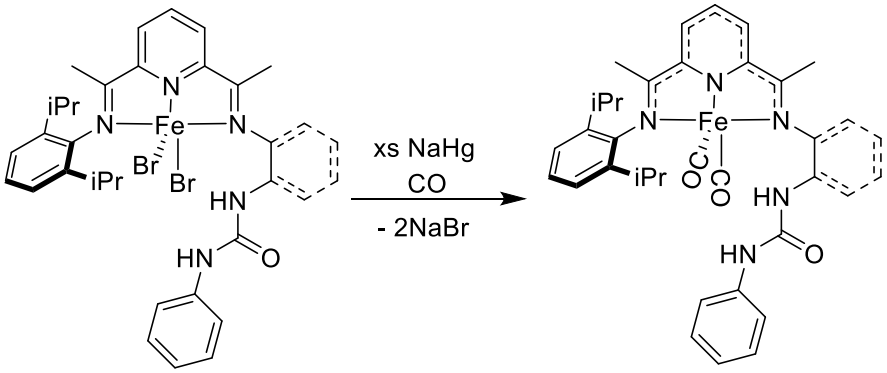

Scheme 4.4.2. Reduction of the urea complexes **8FeBr₂** and **9FeBr₂** to form the iron carbonyls **8Fe(CO)₂** and **9Fe(CO)₂**, respectively.

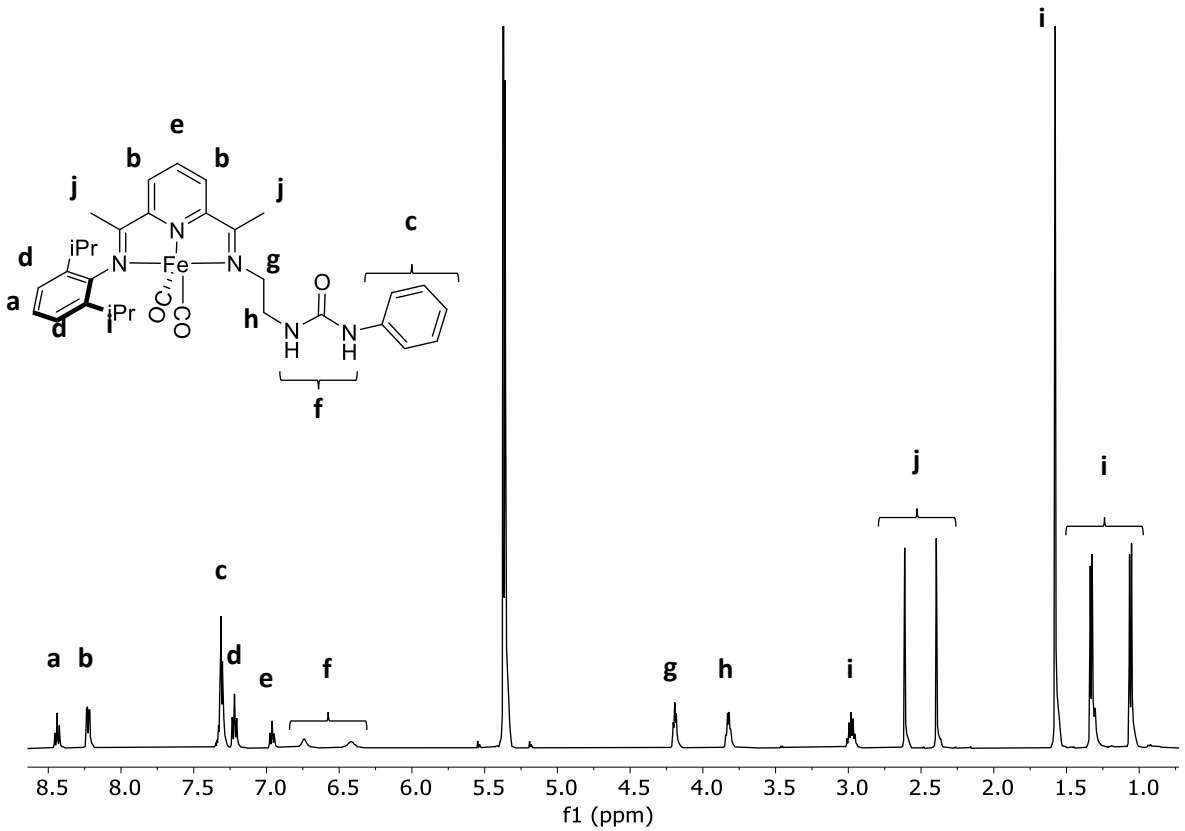

Figure 4.4.1. ^{1}H NMR (500 MHz) of **8Fe(CO)$_2$** in CD_2Cl_2.

To investigate the binding of nitrate at an iron center without a urea group present, a control compound was used. The complex **1Fe(CO)$_2$** was used as a control complex for this study, first by oxidizing with two equivalents of $FcPF_6$ in MeCN to yield **1Fe(PF$_6$)$_2$**, then introducing two equivalents of NO_3^- to give the η^1: η^2 bis(nitrate) complex, **1Fe(NO$_3$)$_2$**. **1Fe(NO$_3$)$_2$** was then crystallized from vapor diffusion of Et_2O into a concentrated MeCN solution. The structure shows that the pendant pyrrolidine has been protonated, which is suspected to be due to the presence of adventitious water, which can be difficult to remove from tetrabutylammonium salts ($TBANO_3$ was used in this reaction).

Work has now been undertaken to isolate the nitrate bound variants of **8Fe(CO)$_2$** and **9Fe(CO)$_2$** through the methods used for **1Fe(NO$_3$)$_2$**. These complexes are expected to have a significantly stronger interaction with the nitrate anion, which will hopefully lead to ultimate nitrate reduction on iron.

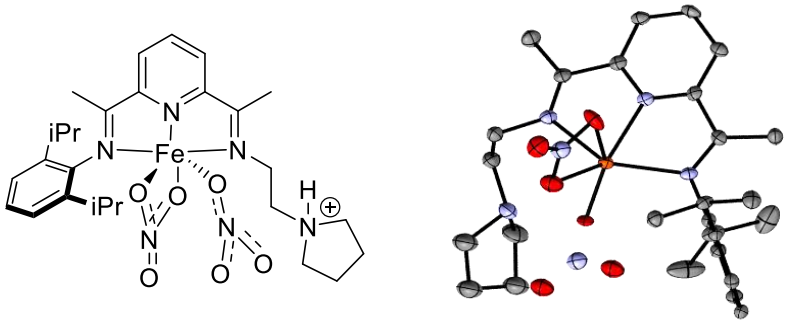

Figure 4.4.2. ChemDraw and ORTEP of **1Fe(NO$_3$)$_2$** showing nitrate binding.

5.1 Lanthanides as Reductants for Nitrogen Oxides

Divalent samarium, Sm(II), is known to be a useful reductant in many organic transformations, such as reduction of aryl and alkyl nitro compounds to from N-N bonds.[61] Likewise, Sm(II) has shown activity towards the reduction, or reductive disproportionation, of the GHG CO_2.[70] Bis(pentamethyl)cyclopentadienyl samarium, $SmCp^*_2$, was found to be capable of activating dinitrogen as well as reducing nitrogen oxides such as the potent GHG nitrous oxide by Evans et. al.[60,71] Of all the lanthanides, Sm(II) is the most reductive that can be isolated under normal chemical conditions with a E ½ of -1.55 V (versus normal hydrogen electrode).[72] In light of this work, we reasoned that samarium should have the power to reduce other nitrogen oxides along the denitrification pathway (**5.1**), eliminating the potent GHG products as well as the aquatic pollutants from agricultural run-off. Utilizing samarium diiodide (SmI_2) as a reductant, it was found that reduction of these nitrogen species is possible, and the products of the reactions were quantified.

$$NO_3^- \xrightarrow{2e^-} NO_2^- \xrightarrow{e^-} NO \xrightarrow{e^-} \tfrac{1}{2} N_2O \xrightarrow{e^-} \tfrac{1}{2} N_2 \qquad \textbf{(5.1)}$$

In the investigation of nitrogen reduction by this lanthanide system, it should be noted that the only other synthetic system capable of completing the reduction of nitrate to dinitrogen, which was mentioned briefly in chapter 1. This system, a (PNP)Ni complex synthesized by Gwak et. al., which proposes a system that is potentially catalytic, utilizing carbon monoxide as an O-atom acceptor.[32] While this system is a significant advancement in the reduction of nitrogen oxides, the reactions suffer from low yields and required multiple reaction steps and vessels, which we hoped to address in this work.

The reaction of SmI_2 with nitrate was tested at two different reaction stoichiometries under an atmosphere of argon. The first, reaction was carried out using one molar equivalent of SmI_2 per nitrate (1:1), the second stoichiometry tested was six molar equivalents of SmI_2 per nitrate (6:1). A similar set of reactions were carried out with nitrite, with both 1:1 and 4:1 molar ratios of SmI_2 to nitrite being tested. These reaction stoichiometries were chosen because it should require 5 and 3 electrons to reduce nitrate and nitrite to half an equivalent of dinitrogen, respectively due to the oxidation state of the nitrogen in either species. Through the use of these two different stoichiometries identification of stable reaction intermediates (in the 1:1 reactions for both nitrate and nitrite) would be possible and could give insights into the mechanism of the reactions, while the 6:1 and 4:1 reactions would ensure that the NO_x^- was fully reduced and the remaining Sm(II) could then be quantified using UV-vis spectroscopy.

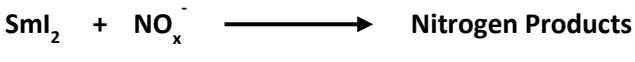

SmI_2		NO_3^-
1	:	1
6	:	1
		NO_2^-
1	:	1
4	:	1

Figure 5.1.1. A generic reaction between SmI_2 and a nitrogen oxide with the tested stoichiometries shown.

5.2 Ion Chromatography

Products of the reduction reactions were evaluated in the solution phase using ion chromatography (IC). Using this instrumentation, we were able to detect anions relevant to the reaction: nitrate (NO_3^-), nitrite (NO_2^-), and iodide (I^-). Ion chromatography samples were prepared by removing all the reaction solvent (THF) and then redissolving the resultant solid in nano-pure water. These solutions were then filtered through 0.22 μm polypropylene filters to remove any insoluble material.

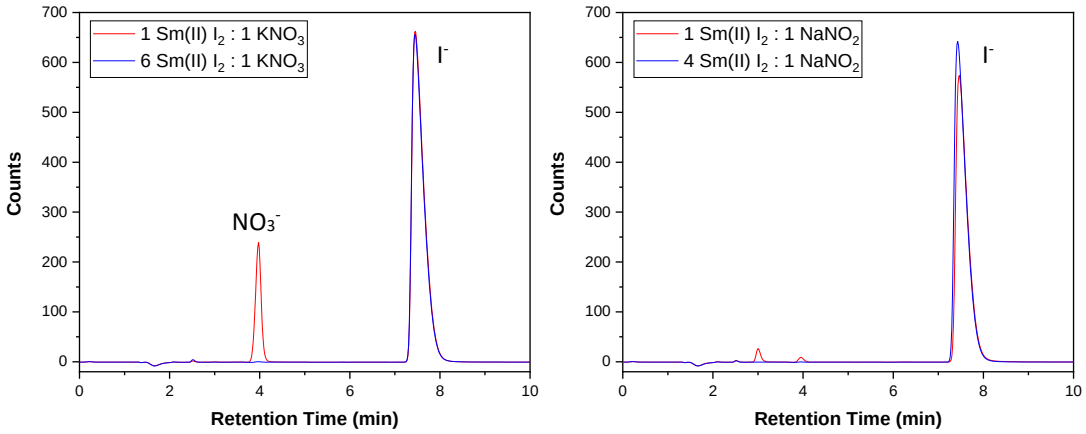

Figure 5.2.1. IC chromatographs of nitrate (left) and nitrite (right) reductions showing the 1:1 reactions in red and the excess SmI_2 reactions in blue.

The IC from the nitrate 1:1 (SmI_2:NO_3^-) reaction contained some nitrate; however, no nitrite was detected. The 1:1 reaction consumed approximately 14% of the nitrate in the reaction. The nitrate 6:1 (SmI_2:NO_3^-) reaction did not contain any detectable nitrate or nitrite. The absence of nitrite in either reaction is a potential clue in the reaction mechanism of SmI_2, possibly hinting that this reaction is not following the denitrification pathway as expected.

Unlike the nitrate reductions, the nitrite samples all showed complete, or near complete, consumption of the nitrite in both reaction stoichiometries. The complete consumption of nitrite should not be possible in the 1:1 reaction as the amount of SmI_2 added is only enough to convert the nitrite to nitric oxide (a one electron process), which does not follow the observed reactivity (dinitrogen, nitrous oxide, and nitric oxide are all observed in the headspace). This result would indicate that there is secondary reactivity taking place to result in the consumption of the nitrite considering the IC experiment will detect any nitrite present, even if it is complexed with the Sm^{3+} product.

5.3 Reaction Headspace Analysis

In addition to analyzing the ion content of the reactions, the headspaces were also sampled after allowing the compounds to react for 48 hours in the dark under an atmosphere of argon. Gas-Phase transmission IR and gas chromatograph equipped with a thermal conductivity detector (GC-TCD) were utilized to test for the presence of gaseous nitrogen oxides for the former and elemental nitrogen via the latter. Using the GC-TCD we are able to detect gasses that are not IR active, and can separate nitrogen and oxygen from the atmosphere to ensure that the system is leak free as seen in Figure **S52**.

GC analysis of the 1:1 nitrate reduction reaction shows the presence of nitrous oxide and nitrogen gas, along with some hydrogen production which was found to be unavoidable and likely due to small amounts of water that were present in the glovebox atmosphere or adsorbed to the reagents. Hydrogen production tracked with the starting nitrogen oxide salt content due to the reduction of water by SmI_2. If the reaction stoichiometry was changed to 6:1 (SmI_2:NO_3^-) , it was observed that the only product in the headspace was nitrogen gas. A similar result occurs when nitrite is used in place of nitrate at a stoichiometry of 4:1 (SmI_2:NO_2^-) , where the only detected product is dinitrogen. In the case of the 1:1 nitrite reaction, however, it is observed that not only are nitrous oxide and nitrogen present, but also nitric oxide. The presence of nitric oxide is exclusive to the nitrite 1:1 reactions and hints to a potentially different mechanism of nitrite reduction versus nitrate reduction.

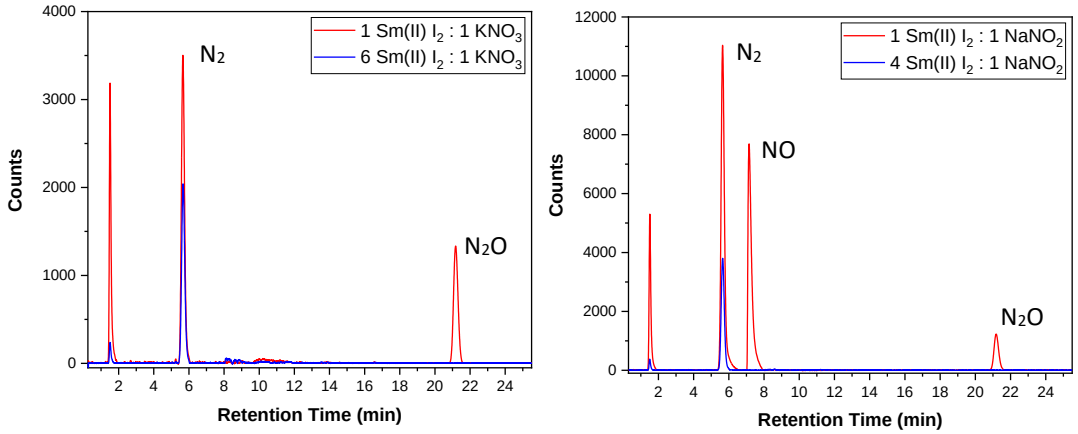

Figure 5.3.1. GC chromatographs of nitrate (left) and nitrite (right) reductions showing the 1:1 reactions in red and the excess SmI_2 reactions in blue.

Table 5.3.1. The gaseous products of NO_x^- reduction by different SmI_2 ratios.

SmI_2		NO_3^-	Gaseous Products
1	:	1	N_2O, N_2
6	:	1	N_2
		NO_2^-	
1	:	1	NO, N_2O, N_2
4	:	1	N_2

Through analysis of the reaction headspace of these nitrogen reductions, it was found that not only is SmI_2 capable or reducing nitrate, but it is also capable of reducing gaseous nitrogen oxides, particularly nitrous oxide, a notoriously long-lived greenhouse gas. The 1:1 reaction stoichiometries were useful in determining that nitrous and nitric oxides were reaction intermediates in the denitrification of nitrate and nitrite, while the lack of these gasses in the excess SmI_2 reactions shows that they are also viable substrates for reduction. The reduction of these oxides was found to produce near quantitative amounts of nitrogen gas when stoichiometric amounts of SmI_2 were used in control experiments as seen in **Table 5.3.2** (**Figure S48** and **S49**). These experiments used pure gas (either nitrous or nitric oxide) to demonstrate SmI_2's versatility in nitrogen reduction or deoxygenation.

Table 5.3.2. N_2 yields and nitrogen oxide consumption calculated via GC and IC for all nitrogen oxides tested.

Sm^{2+} : $N_xO_y^{n-}$	$N_xO_y^{n-}$	Gaseous Products	% N_2 Yield	% $N_xO_y^{n-}$ Consumed
2 : 1	N_2O	N_2	97	100
1 : 1	N_2O	N_2	65	69
4 : 1	NO_2^-	N_2	66	100
1 : 1	NO_2^-	N_2, NO, N_2O	151	97
			51	97
6 : 1	NO_3^-	N_2	80	100
1 : 1	NO_3^-	N_2, N_2O	66	14
			14	14

5.4 Iodine Quantification

The yields of nitrogen from the nitrite 1:1 reaction was initially found to be much higher, roughly 151%, than was possible given that divalent lanthanides are known one electron donors. There was also an observed very strong absorbance in the UV-vis spectrum of the nitrite 1:1 reduction not seen in any of the other reduction experiments. This result prompted further investigation into the identity of this highly absorbing species.

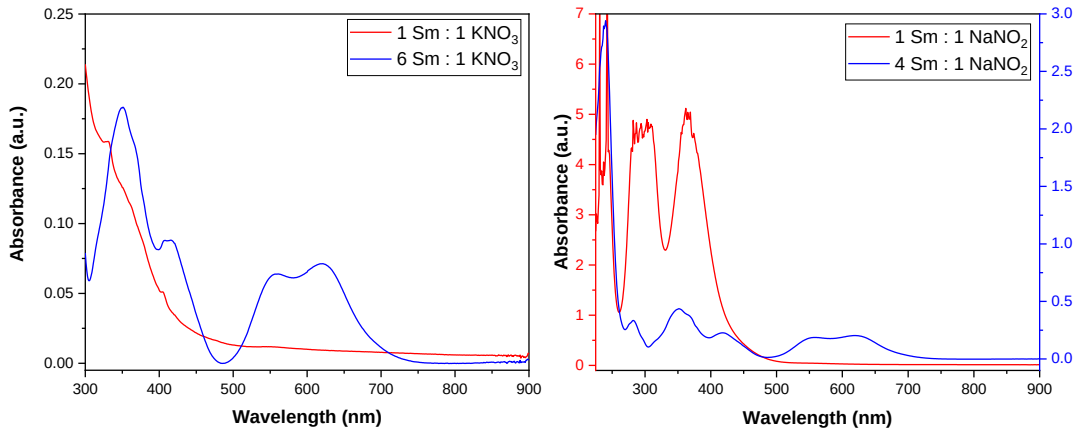

Figure 5.4.1. UV-vis plots of nitrate (left) and nitrite (right) reaction solutions after reacting for 2 days. The 1:1 reactions are shown in red and the excess SmI_2 reactions are shown in blue. Absorbances as 557 and 621 nm are characteristic of SmI_2 in THF.

Using a standard starch-iodine test it was confirmed that the strong absorbance noted in the nitrite 1:1 reduction was elemental iodine. Iodine quantification was carried out using a sodium thiosulfate titration of the reaction solution. It was determined that iodine was being produced in 26% yield, which when acting as a $2e^-$ reductant (one e^- from each iodide), lowers products, NO and N_2O, accounting for the rest of the reaction products. The reaction for the reduction of nitrite by iodide is shown in equation **5.2**, where the two oxygen atoms are presumed to bind to an undetermined samarium product.

$$2NO_2^- + 2I^- \rightarrow 2NO + 2O^{-2} + I_2 \qquad \textbf{(5.2)}$$

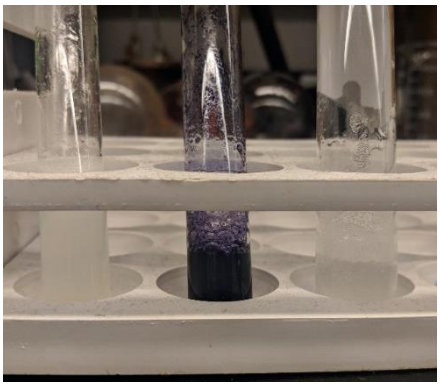

Figure 5.4.2. Starch test for iodine. Nitrate 1:1 (left), nitrite 1:1 (center), and sodium iodide blank (right). The purple color of the center reaction mixture indicates the presence of iodine while the colorless solutions show no iodine.

5.4 Conclusions and Future Work

This work has demonstrated that the divalent lanthanide, samarium diiodide, is capable of completing the denitrification of nitrate in a single pot. Though there does exist another system that is capable of the same reactivity, the yield of nitrogen has been significantly improved by the use of samarium. While the reduction of nitrogen oxides gives near quantitative yields of dinitrogen, when the appropriate reaction stoichiometry is used, there are still significant barriers to employing samarium as a true catalyst. The driving force for nitrogen reduction with samarium can likely be attributed to its

oxophilicty, which will assist in the difficult first step of reaction, nitrate reduction. Overcoming this issue will require a compatible O-atom acceptor that can deoxygenate any samarium-oxo species that are produced in the reaction inside of an electrochemical cell, for example.

Work on further studies of deoxygenation and reduction reactions using soluble Sm^{2+} will be continued as well as investigation of the potential for an electrochemical system for nitrate reduction that employs samarium as the catalyst.

6.1 Conclusions

The synthesis and characterization of a novel dinuclear DNIC, **$1Fe_2(NO)_4$**, has been described. Upon oxidation, the DNIC reductively couples nitric oxide to release nitrous oxide. Synthesis of various other DNIC complexes, both mono- (**$2Fe(NO)_2$** and **$3Fe(NO)_2$**) and di-nuclear (**$4Fe_2(NO)_4$**), were also described. These complexes were used to give insight into the mechanism of nitric oxide couple in the dinuclear DNIC system. From these experiments, it was observed that the mono-nuclear DNICs do not couple or release nitric oxide upon oxidation with ferrocenium. It was also observed that stabilization of the mixed valence, dinuclear DNIC by addition of a pendant base which is able to form the stable, five-coordinate $\{Fe(NO)_2\}^9$ center also stopped nitrous oxide evolution. These studies highlight that nitrous oxide evolution is an effect of the proximity of two DNICs which independently are inert. Further studies will be conducted to elucidate the mechanism of nitric oxide coupling in these DNIC systems.

The synthesis and characterization of complexes with pendant glycols was reported, however the work is still in the early stages. These complexes were tested for their ability to bind alkali earth metals by ^1H NMR binding studies. An early study of electrochemical generation of iron carbonyl complexes was reported. These complexes are able to be isolated through chemical means, though the generation of these species through electrochemical means could lead to the development of a family of switchable carbon dioxide reduction electrocatalysts. It was shown that carbon monoxide capture and release was possible with these complexes, however, more work will need to be conducted to determine favorable conditions for electrochemical reduction of carbon dioxide. There was also a series of pendant urea complexes reported. These complexes will be studied for their ability to activate small molecules by means of hydrogen bonding of the urea group. These works are all in their infancy and will be studied in future work.

A divalent samarium complex was found to be capable of the complete denitrification of nitrate to nitrogen gas. The reaction was found to be stoichiometric in the reduction of all the nitrogen oxides in the denitrification pathway with Sm^{2+} being a one electron reductant except for the reduction of nitrite where it was found that iodide was a suitable reductant and samarium could act as an oxygen atom

acceptor which lead to the formation of moderate amounts of nitric oxide, which could then be further reduced to form nitrous oxide and finally elemental nitrogen. This system is representative of one of two synthetic systems capable of complete denitrification and the only system that can complete the reaction in a single pot.

S.1 General Considerations

All reagents were purchased from commercial sources and used without further purification. Dry and air-free solvents were obtained with a PureSolv solvent still (Vac Atmospheres Inc.). Nanopure water was achieved by a Millipore Milli-Q Advantage A-10 Nanopure system. Gases were purchased from AirGas inc. The asymmetric PDI ligand **[(ArN=C(CH3))C2H3N((CH3)C=O] (Ar= 2,6-i Pr-C6H3)**,[73] **1Fe(CO)$_2$**, **[1Fe(NO)$_2$]$^+$**, **[5Fe(NO)]$^+$**,[58] and **5Fe(CO)$_2$**,[66] were synthesized according to literature procedures. Air sensitive reagents were handled in an inert-atmosphere glovebox filed with either N_2 or Ar, or on a Schlenk line following standard air-free technique. It should be noted that any hazardous reagents (sodium amalgam (NaHg), nitric oxide, phenyl isocyanate, etc.) should be handled with extreme care to avoid exposure due to their toxic nature. All reactions carried out in a pressurized vessel were shielded with a polycarbonate blast shield in case of rupture.

FT-IR

IR spectra were collected on a Thermo iS10 FT-IR spectrometer. Attenuated total reflectance (ATR) IR spectra were collected on a single-bounce diamond ATR accessory. Solution-phase IR spectra were collected in a liquid IR cell equipped with CaF_2 windows at 2 cm^{-1} resolution. Gas-phase IR were collected with a Pike Technologies short-pathlength (100 mm) gas transmission cell fitted with CaF_2 windows, resolution was set to 0.5 cm^{-1} and 32 scans.

NMR

All NMR spectra were collected on a Bruker Avance III 500 MHz instrument. Spectra were referenced to the solvent signal for all ^1H and ^{13}C experiments, benzamide (118 ppm) was used as an external reference for ^{15}N spectra. ^1H NMR salt titrations were carried out by dissolving the glycol to be titrated in CD_3CN (20 mM) and adding 0.5 mL to a J-Young NMR tube. An initial spectrum was collected and then the tube was brought back into a glovebox where 0.1 equivalents of $NaPF_6$ in CD_3CN (40 μL) was added. The tube was then resealed and shaken vigorously for 30 seconds and allowed to equilibrate for 5 minutes before taking

another spectrum. This process was repeated until the titration was complete and the binding constants were calculated using the BindFit software (supramolecular.org).

Electrochemistry

CV were collected with a Pine WaveNow potentiostat with a glassy carbon working electrode and a platinum wire counter electrode. A non-aqueous silver nitrate reference was used in all experiments except those where a silver pseudo-reference was used; the CV were then internally referenced to ferrocene except where noted. Tetrabutylammonium hexafluorophosphate was employed as a supporting electrolyte at 0.1 M for all experiments.

Mössbauer

Mössbauer spectra were collected on a constant acceleration spectrometer (Wissel GMBH, Germany) in a horizontal transmission mode using a 50 mCi ^{57}Co source. For room temperature measurements approximately 150 mg of sample was loaded into an acrylic sample holder and covered with Paratone-N oil to prevent oxidation. Data collection was between 2 and 7 days to get a statistically significant spectrum. Low temperature measurements were collected in vacuum with no oil in the sample. Isomer shifts were normalized to that of metallic iron and spectra were fitted assuming Lorentzian line shapes using the NORMOS (Wissel GMBH) least-squares fitting program.

Gas Chromatography

GC chromatographs were collected on an SRI 8610C GC equipped with a thermal conductivity detector (TCD). The carrier gas was argon, and the column was a 10 m Agilent Carboxen-1000. Reaction headspaces were sampled using Hamilton gas-tight syringes to sample 0.5 mL of headspace. Gas calibration was carried out by injecting pure gases into vials of known volume and sampling 0.5 mL of the vial contents. The oven temperature profile was as follows: 30 °C for 8 minutes then ramp at 20 °C min^{-1} until the temperature is 200 °C, finally hold for 12 min. Retention times (in minutes) are as follows; H_2: 1.5, O_2: 5.3, N_2: 5.6, NO: 7.2, N_2O: 21.2.

Ion Chromatography

Ion chromatograms were collected on a Agilent 1100 series HPLC with a simple anion column and a Waters 432 conductivity detector. After NO_x^- rection with SmI_2 was complete, all the reaction solvent was removed *in vacuo*. The resultant solid was then dissolved in 100 mL of nanopure water. 1 mL of this solution was then diluted to 10 mL total volume with more nanopure water. This solution was then passed through a 0.22 μm, polypropylene membrane, syringe filter. Calibrations was completed using external standards made from $NaNO_2$ of KNO_3. Ion retention times (in minutes) are as follows; NO_2^-: 3.02, NO_3^-: 3.98, I^-: 7.45.

UV-vis

UV-vis spectra were collected on a JASCO V-670 spectrometer at room temperature in a 1 cm quartz cuvette (Starna Cells). Samarium reactions were analyzed by collecting 100 μL of reaction solution and diluting to 10 mL with anhydrous THF. Oxidation monitoring was conducted using a 6-cell autosampler which allowed for stirring of the solution by a small magnetic stir bar. The compound was dissolved in acetone and loaded into the cuvette which was capped with a rubber septum. A starting spectrum was collected, then one equivalent of oxidant was added via acetone solution through the septum under stirring. Spectra were then collected for 120 minutes (one spectrum every two minutes). Spectra were collected with both a solvent baseline as well as a dark correction at a scan rate of 400 nm min^{-1} with a near-IR resolution of 4 nm and an ultraviolet-visible resolution of 2 nm, sampled every 1 nm.

Iodine Titration

A 22.4 mM solution of sodium thiosulfate was prepared in deionized water and loaded into a burette. The THF reaction solution was added directly to 90 mL deionized water with three rinses of the reaction vessel with water. To the reaction solution was added 3 mL starch indicator solution in deionized water causing the solution to take on an almost black, purple-blue color. The solution was then titrated with the sodium thiosulfate solution until colorless, the endpoint.

Crystallography

Reflection data was collected on a Rigaku Oxford Diffraction (ROD) XtaLABPRO equipped with a Pilatus P200K hybrid photon counting (HPC) detector and fine-focused Mo Kα1 radiation. Data was collected at 100 K with data collection strategies to ensure completeness and desired redundancy determined using CrysAlis^{PRO}. Data processing was done using CrysAlis^{PRO} and structures were solved via intrinsic phasing methods using ShelXT and subjected to a least-squares refinement with ShelXL within the Olex2 software.

S.2 Synthesis

DNIC Synthesis via $Fe(CO)_2(NO)_2$

The synthesis of neutral $\{Fe(NO)_2\}^{10}$ DNICs can achieved in much better yields by combining the ligand of choice with $Fe(CO)_2(NO)_2$ using one of two methods. Both methods require the use of $[Fe(CO)_3(NO)][Na(18\text{-}c\text{-}6)]$ which is synthesized by reacting one molar equivalent of $[Na(18\text{-}c\text{-}6)][NO_2]$ with $Fe(CO)_5$ in THF. This product, a yellow solid once the solvent is removed, can then be stored for long periods of time and is used without purification.

Method 1 one-pot synthesis: In a glovebox, $[Fe(CO)_3(NO)][Na(18\text{-}c\text{-}6)]$ (0.5 g; 1.09 mmol) is dissolved in ca. 12 mL THF. In a 250 mL Schlenk flask, $NOBF_4$ (0.1277 g; 1.09 mmol) is added along with a stir bar, and the flask is fitted with a rubber septum. A vacuum line is attached to the stopcock of the flask and a static vacuum is applied, then the THF solution is added rapidly through the septum with stirring set to high. Immediately upon contact, the solution turns from orange to red and bubbling is observed, this solution is stirred for 30 minutes before adding the desired ligand (1.0 mmol for a mono-nuclear complex or 0.5 mmol for a di-nuclear complex) and continuing stirring for 2 hours. The solution volume is then reduced to near saturation and the mixture is passed through ca. 15 cm of neutral alumina in a transfer pipette (0.85 cm diameter) and the dark red/brown product is collected. The THF solution can then be concentrated and layered with a suitable solvent (e.g., pentane) to yield crystalline product. If this method is not suitable, which is the case for particularly polar ligands that do not chromatograph well (for example complexes with unbound amines) use method 2.

Method 2 distillation: In a glovebox, $NOBF_4$ (0.1277 g; 1.09 mmol) is loaded into a 25 mL round-bottom flask. In a scintillation vial, $[Fe(CO)_3(NO)][Na(18\text{-}c\text{-}6)]$ (0.5 g; 1.09 mmol) is dissolved a minimal amount of THF (about 10 mL). In a 50 mL round-bottom flask, the desired ligand (1.0 mmol or 0.5 mmol depending on the complex) is added along with 5 mL THF. The round-bottom flasks are then connected to a vacuum distillation head and the thermometer port and vacuum connection are plugged with rubber septa. The scintillation vial that contains the $[Fe(CO)_3(NO)][Na(18\text{-}c\text{-}6)]$ solution is also fitted with a rubber septum and everything is brought out of the glovebox. On the Schlenk line, the distillation apparatus is flushed with inert gas while the $NOBF_4$ is chilled in an ice bath along with the scintillation vial for 10 minutes. Then, the THF solution is mixed with the $NOBF_4$ by injecting through the thermometer port septa as rapidly as possible. This solution is allowed to stir for 30 minutes before the distillate side of the apparatus is frozen in liquid nitrogen and vacuum is applied to the system by means of a needle through the vacuum adapter septum. By this method, the red $Fe(CO)_2(NO)_2$ is vacuum distilled onto the frozen ligand solution without the use of heat which will decompose the reactant. Once the distillation is complete, the apparatus is allowed to warm to room temperature and the distillate is stirred for 2 hours after which the solvent is removed *in vacuo* and the apparatus is brought back into the glovebox where the solid product can be redissolved in THF, filtered through celite if desired, and layered with a suitable solvent (e.g., pentane) to produce crystalline product.

^{pyrrol}PDIFe$_2$(NO)$_4$ (1Fe$_2$(NO)$_4$)

In an inert atmosphere glovebox, **[1Fe(NO)$_2$]$^+$** (0.3635 g; 0.535 mmol) was added to a 20 mL scintillation vial, dissolved in 5 mL of CH_2Cl_2 and placed in a glovebox freezer for 30 minutes. A second vial was loaded with bis-cyclopentadieneyl cobalt(II) (0.1012 g; 0.535 mmol) and also dissolved in 5 mL of DCM and placed in the freezer. After both solutions were cooled, the bis-cyclopentadieneyl cobalt(II) solution was added dropwise under strong stirring to the **[1Fe(NO)$_2$]$^+$** solution and allowed to stir for 30 minutes by which time a yellow precipitate had formed and the solution had become red-brown. The reaction solution volume was then reduced by half *in vacuo* and filtered through celite to remove the yellow cobalt(III) product. The filtrate was then layered with pentane to yield X-ray quality crystals of **1Fe$_2$(NO)$_4$**. Yield: 48%.

^{Ar}MIP (L2)

2-Acetylpyridine (0.5000 g; 4.13 mmol) and 2,6-Diisopropyl aniline (0.7318 g; 4.13 mmol) were combined in 50 mL of anhydrous MeOH. The solution was stirred for 15 minutes before adding 0.5 mL formic acid catalyst. Upon addition of the formic acid the solution began to turn from colorless to golden-yellow. Stirring was continued overnight at ambient temperature (16 hours). The solvent was then removed *in vacuo* to yield the crude product as a yellow oil. The oil was then mixed with 40 mL MeCN and placed in a freezer for 24 hours to yield large, square crystals of **L2**. The crystals were collected by vacuum filtration and washed with ice-cold MeCN (3 x 10 mL) to yield pure product. Yield: 57%.

[^{Ar}MIPFeBr$_2$]$_2$ ([2FeBr$_2$]$_2$)

In an inert-atmosphere glove box, a scintillation vial was charged with **L2** (0.1500 g; 0.535 mmol) and anhydrous $FeBr_2$ (0.1154 g; 0.535 mmol), followed by 10 mL of MeCN. The mixture immediately turned dark-red, and a precipitate started forming. The suspension was allowed to stir for 4 hours at which point 15 mL Et_2O was added. The precipitate was then collected by vacuum filtration and washed with Et_2O (3 x 10 mL) to give **[2FeBr$_2$]$_2$** as a red powder. To obtain X-ray quality crystals, 150 mg of **[2FeBr$_2$]$_2$** was dissolved in MeCN and allowed to vapor diffuse with Et_2O by the vial-in-vial method.

^{Ar}MIPFe(CO)$_3$ (2Fe(CO)$_3$)

In an inert-atmosphere glove box, **[2FeBr$_2$]$_2$** (0.4961 g; 1.00 mmol) was loaded into a Fischer-Porter tube with 5 wt% NaHg (0.9656 g; 2.1 mmol Na) and 10 mL CH_2Cl_2. The tube was then immediately charged with 40 psi of carbon monoxide and stirred for 48 hours, during which time the solution turned from a red suspension to dark blue. The solvent was then removed *in vacuo* and 10 mL of Et_2O was added. The blue Et_2O solution was filtered through celite and the solvent was allowed to evaporate to yield large blue crystals of **2Fe(CO)$_3$** suitable for X-ray diffraction.

ArMIP$_2$Fe(CO) (2$_2$Fe(CO))

In an inert-atmosphere glove box, **[2FeBr$_2$]$_2$** (0.2500 g; 0.504 mmol) was added to a 100 mL side-arm flask was combined with 12 mL SmI_2 solution in THF (0.1 M); upon addition of the SmI_2 solution an immediate color change from blue to green took place. The headspace of the flask was then partially removed on a Schlenk line and 12.3 mL (0.252 mmol) of carbon monoxide was added via gas-tight syringe. The reaction was allowed to stir for 16 hours and then the solvent was removed *in vacuo*. The solid was then triturated in 15 mL MeCN and filtered. The filtrate was discarded and the solid was washed off the filter with Et_2O and allowed to evaporate to yield X-ray quality crystals of **2$_2$Fe(CO)**.

^{Ar}MIPFe(NO)$_2$ (2Fe(NO)$_2$)

In a 20 mL scintillation vial, **2Fe(CO)$_3$** (0.1383 g; 0.329 mmol), $NaNO_2$ (0.0454 g; 0.658 mmol), and NEt_3H PF_6 (0.3253 g; 1.32 mmol) were added, followed by about 10 mL of anhydrous MeOH. The reaction was stirred for 16 hours, at which point a red-brown precipitate had formed. The precipitate was collected via vacuum filtration and rinsed with 5 mL of MeOH. The filter was then washed with minimal DCM to collect the product as a dark red solution, which was layered with pentane to afford X-ray quality crystals of **2Fe(NO)$_2$**. Yield: 38%.

^{Pyrrol}Imine Ligand

Molecular sieves, 4Å, (10 g) were added to a 30 mL pressure vial followed by 3-pentanone (2.49 g; 28.9 mmol) and 1-(2-amionethyl) pyrrolidine (3.00 g; 26.3 mmol) under an atmosphere of nitrogen. The vial was then capped and heated to 80 °C for 48 hours. The vial was then emptied into a filter to remove the sieves and the sieves were washed with anhydrous Et_2O (3 x 20 mL). The solvent was removed by rotary evaporator to yield the crude, dark-yellow oil. The resultant oil was then vacuum distilled, discarding approximately the first 1 mL of distillate and stopping the distillation before dryness was achieved to yield **^{Pyrrol}Imine** as a light-yellow oil.

^{Pyrrol}ImineFe(NO)$_2$ (3Fe(NO)$_2$)

A frozen THF solution of **^{Pyrrol}Imine** was combined with approximately one equivalent of $Fe(CO)_2(NO)_2$ by distilling the latter on to the frozen **^{Pyrrol}Imine**. The mixture was then allowed to warm to room

temperature and stir for 2 hours, by which point the solution had turned from red to green. The green solution was then evaporated to *ca.* 5 mL and layered with pentane to yield X-ray quality crystals of **3Fe(NO)$_2$**. Yield: 46%.

[^{Pyrrol}PDIFe(MeCN)$_2$][PF$_6$]$_2$ (1Fe(PF$_6$)$_2$) In a 25 mL side-arm flask, **1Fe(CO)$_2$** (0.1500 g; 0.283 mmol) and $FcPF_6$ (0.1872 g; 0.566 mmol) were combined and the flask was fitted with a stopper and rubber septum. Through the septum, 5 mL of MeCN was added leading to immediate evolution of gas. The solution was allowed to stir for 1 hour before removing the solvent *in vacuo*. The resultant solid was then triturated in 10 mL Et_2O, loaded onto a celite filter, and washed with 5 mL of Et_2O. The solid was washed off the filter using minimal MeCN and dried. X-ray quality crystals of **1Fe(PF$_6$)$_2$** were grown by vapor diffusion of Et_2O into a concentrated MeOH solution.

Tosyl tetraethyleneglycol monometyl-ether

In a round-bottom flask, tetraethylene glycol monomethyl ether (5.0 g; 24 mmol) was combined with NaOH (1.44 g; 36 mmol) in 70 mL of THF and 10 mL water. The mixture was chilled in an ice bath for 15 minutes before dropwise addition of a THF solution (10 mL) of p-toluenesulfonyl chloride (5.21 g; 27 mmol). The reaction was allowed to stir on ice for 3 hours, then 25 mL of ice water was added and the mixture was loaded into a separatory funnel. The solution was then extracted three times with CH_2Cl_2 (3 x 125 mL). The organic layer was then washed with 0.1 M HCL (100 mL), followed by brine, and finally dried over anhydrous $MgSO_4$ before removing the solvent via rotary evaporator to yield the product, **Tosyl tetraethyleneglycol monometyl-ether**, as a colorless oil.

1-Nitro-(2-tertaethyleneglycol monomethyl-ether) benzene

In a 250 mL Schlenk flask, **Tosyl tetraethylene glycol monometyl-ether** (8.1214 g; 22.4 mmol) was combined with 2-nitrophenol (3.1171 g; 22.4 mmol) and K_2CO_3 (6.1935 g; 44.8 mmol) in 40 mL DMF. The flask was then put under a positive pressure of nitrogen and heated to 80 °C for 12 hours. The solution was then allowed to cool to approximately room temperature before adding 50 mL of water and transferring the solution to a separatory funnel. The solution was then extracted with CH_2Cl_2 three times

(3 x 100 mL). The organic layer was washed with water, then brine, and dried over $MgSO_4$. The solvent was removed via rotary evaporator to yield crude **1-Nitro-(2-tertaethylene glycol monomethyl ether) benzene**. If necessary, the product may be purified by column chromatography (silica; 5% MeOH, CH_2Cl_2).

1-Amino-(2-tetraethylene glycol monomethyl ether) benzene

In an inert-atmosphere glovebox, a Fischer-Porter bottle was loaded with **1-Nitro-(2-tertaethylene glycol monomethyl ether) benzene** (2.85 g; 10 mmol), palladium on carbon (5 mol%) and 20 mL EtOH. The bottle was fitted with a pressure gauge and flushed with H_2 then pressurized to 40 psi. With strong stirring the vessel was heated in a sand bath to 50 °C. Reaction progress was monitored by the consumption of H_2, and the bottle was repressurized multiple times until the pressure no longer dropped after stirring for 30 minutes. The bottle was then sparged with N_2 to remove any H_2 present and the solution was filtered through a glass frit to remove the palladium on carbon. The solvent was removed *in vacuo,* yielding the product, **1-Amino-(2-tetraethylene glycol monomethyl ether) benzene**, as a colorless oil.

^{PEG4}PDIFeBr$_2$ (6FeBr$_2$)

In a 250 mL Schlenk flask, $FeBr_2$ (0.3580 g; 1.66 mmol) and [(ArN=C(CH3))C2H3N((CH3)C=O] (0.5353 g; 1.66 mmol) were dissolved in 40 mL EtOH (200 proof, absolute). The flask was placed under a positive pressure of nitrogen and heated to 80 °C for 30 minutes before adding an EtOH solution of **1-Amino-(2-tetraethylene glycol monomethyl ether) benzene** (0.4238 g; 1.66 mmol) through the septum. The reaction was then allowed to stir for 12 hours. The solvent was then removed *in vacuo* to yield a blue solid which was used without further purification.

^{PEG4}PDIFe(CO)$_2$ (6Fe(CO)$_2$)

In a Fischer-Porter tube, **6FeBr$_2$** (0.3253 g; 0.420 mmol) and 5 wt% NaHg (0.5064 g; 0.881 mmol Na) were added along with 10 mL CH_2Cl_2. The tube was fitted with a pressure gauge and charged with ~40 psi carbon monoxide and stirred for 48 hours. After stirring the reaction solution had turned from dark blue to forest green, at which point the solvent was removed *in vacuo*. The resultant green solid was dissolved in Et_2O and carefully filtered through celite and then the solution was concentrated to near saturation. The

concentrated solution was loaded onto a neutral alumina column which was washed with Et_2O, then CH_2Cl_2, finally the product was eluted with 70:30 THF: pentane. The product was found to be pure by NMR, however, efforts to grow a single crystal suitable for X-ray diffraction were unsuccessful.

^{EthylUrea}PDIFeBr$_2$ (8FeBr$_2$)

In a 250 mL Schlenk flask, $FeBr_2$ (0.2293 g; 1.06 mmol) and [(ArN=C(CH3))C2H3N((CH3)C=O] (0.3492 g; 1.06 mmol) were dissolved in 40 mL EtOH (200 proof, absolute). The flask was placed under a positive pressure of nitrogen and heated to 80 °C for 30 minutes before adding an EtOH solution of 1(2-aminoethyl)-3-phenylurea (0.1906 g; 1.06 mmol) through the septum. The reaction was then allowed to stir for 12 hours. The solvent was then removed *in vacuo* and the crude solid was dissolved in CH_2Cl_2 and filtered through celite. The solvent was then removed to yield the product as a blue powder. Crystals of **8FeBr$_2$** suitable for X-ray diffraction were grown from vapor diffusion of Et_2O into a concentrated MeCN solution.

^{EthylUrea}PDIFe(CO)$_2$ (8Fe(CO)$_2$)

In a Fischer-Porter tube, **8FeBr$_2$** (0.2133 g; 0.306 mmol) and 5 wt% NaHg (0.37 g; 0.643 mmol Na) were added along with 10 mL CH_2Cl_2. The tube was fitted with a pressure gauge and charged with ~40 psi carbon monoxide and stirred for 48 hours. After stirring the reaction solution had turned from dark blue to forest green, at which point the solvent was removed *in vacuo*. The resultant green solid was dissolved in Et_2O and carefully filtered through celite. The Et_2O solution was allowed to evaporate to yield a green, oily solid.

1-(2-aminophenyl)-3-phenylurea

In a 250 mL round-bottom flask, o-diaminobenzene (1.081 g; 10 mmol) was dissolved in 70 mL of dry acetone. The flask was fitted with a rubber septum and flushed with argon for 15 minutes while chilling in an ice bath. An acetone solution (10 mL) of phenyl isocyanate (1 g; 0.84 mmol) was then added under strong stirring. The solution was allowed to stir for 2 hours at which point a white precipitate had formed.

The solution was vacuum filtered to collect the solid and then washed with cold acetone (3 x 15 mL). The white solid was then crystallized from hot CH_2Cl_2 to yield pure **1-(2-aminophenyl)-3-phenylurea.**

^{PhenyUrea}PDIFeBr$_2$ (9FeBr$_2$)

In a 250 mL Schlenk flask, $FeBr_2$ (0.3580 g; 1.66 mmol) and [(ArN=C(CH3))C2H3N((CH3)C=O] (0.5353 g; 1.66 mmol) were dissolved in 40 mL EtOH (200 proof, absolute). The flask was placed under a positive pressure of nitrogen and heated to 80 °C for 30 minutes before adding an EtOH solution of **1(2-aminophenyl)-3-phenylurea** (0.3773 g; 1.66 mmol) through the septum. The reaction was then allowed to stir for 12 hours. The solvent was then removed *in vacuo* to yield a blue solid which was used without further purification.

^{PhenylUrea}PDIFe(CO)$_2$ (9Fe(CO)$_2$)

In a Fischer-Porter tube, **9FeBr$_2$** (0.5934 g; 0.794 mmol) and 5 wt% NaHg (0.96 g; 1.67 mmol Na) were added along with 10 mL CH_2Cl_2. The tube was fitted with a pressure gauge and charged with ~40 psi carbon monoxide and stirred for 48 hours. After stirring the reaction solution had turned from dark blue to forest green, at which point the solvent was removed *in vacuo*. The resultant green solid was dissolved in Et_2O and carefully filtered through celite. The Et_2O solution was allowed to evaporate yielding green crystals of **9Fe(CO)$_2$** suitable for X-ray diffraction.

^{Pyrrol}PDIFe(NO$_3$)$_2$ (1Fe(NO$_3$)$_2$)

In a scintillation vial, **1Fe(PF$_6$)$_2$** (0.0405 g; 0.0478 mmol) was dissolved in 5 mL MeCN. To this solution tetrabutylammonium nitrate (0.0146 g; 0.0478 mmol) was added, resulting in an immediate color change from red to purple. The solution was stirred overnight before removal of the stir bar and layering with Et_2O. After two days, the layering yielded purple-blue crystals of **1Fe(NO$_3$)$_2$** suitable for X-ray crystallography. The pyrrolidine of the structure is protonated likely due to water adsorbed to the TBA^+ salt, as they are appreciably hygroscopic.

S.3 DNIC Oxidations

One-Electron Oxidation of $1Fe_2(NO)_4$

In a 25 mL side-arm flask, **$1Fe_2(NO)_4$** (0.0521 g; 0.0801 mmol) and ferrocenium hexafluorophosphate (0.0265 g; 0.0801 mmol) were added, and the flask was fitted with a stopper and rubber septum. Through the septa, 5 mL of acetone was added, and the reaction was allowed to stir for 16 hours. The reaction headspace was analyzed by GC-TCD and found to contain N_2O as a product of the oxidation (86% yield based on 1 N_2O/1 Complex), which was confirmed by gas-phase IR ($\nu_{ON(N)}$ 2224 cm^{-1}). The acetone was then removed *in vacuo* and the solid was redissolved in CH_2Cl_2 and filtered through celite. The CH_2Cl_2 solution was concentrated and layered with Et_2O to yield crystals of the mono-nuclear $\{Fe(NO)_2\}^9$ complex, **$[1Fe(NO)_2]^+$**.

$[^{Ar}MIPFe(NO)_2][PF_6$ or $BF_4]$

In a 25 mL side-arm flask **$2Fe(NO)_2$** (0.0500 g; 0.126 mmol) and oxidant (either $FcPF_6$ or $FcBF_4$) (0.126 mmol) were combined, and the flask was fitted with a stopper and rubber septa. Through the septa, 5 mL of THF was added, and the stopper was fully closed. The reaction was allowed to stir for 16 hours before the solvent was removed *in vacuo*. The resultant solid was then washed with Et_2O (3 x 5 mL) and redissolved in THF and layered with pentane to yield X-ray quality crystals of either **$[2Fe_2(NO)_4(PF_4)][PF_6]$** or **$2Fe(NO)_2(BF_4)$**.

$[^{Pyrrol}ImineFe(NO)_2][PF_6]$ ($[3Fe(NO)_2][PF_6]$)

In a 25 mL side-arm flask **$3Fe(NO)_2$** (0.0650 g; 0.218 mmol) and $FcPF_6$ (0.0722 g; 0.218 mmol) were combined and the flask was fitted with a stopper and rubber septa. Through the septa, 5 mL of THF was added, and the stopper was fully closed. The reaction was allowed to stir for 16 hours before the solvent was removed *in vacuo*. The solid was redissolved in CH_2Cl_2 and filtered through celite before layering with Et_2O to yield crystalline **$[3Fe(NO)_2][PF_6]$**.

One-Electron Oxidation of $5Fe(NO)_2$

In a 25 mL side-arm flask, **$5Fe(NO)_2$** (0.0565 g; 0.100 mmol) and ferrocenium hexafluorophosphate (0.0331 g; 0.100 mmol) were added, and the flask was fitted with a stopper and rubber septum. Through the septum, 5 mL CH_2Cl_2 was added, and the reaction was allowed to stir for 16 hours. The reaction headspace was analyzed by gas-phase IR and found to contain no detectable N_xO_y species. The reaction solution was then filtered through celite, the volume was reduced by half, and layered with Et_2O which afforded the cationic $\{Fe(NO)_2\}^9$ complex in 68% yield.

S.4 Supplemental Figures

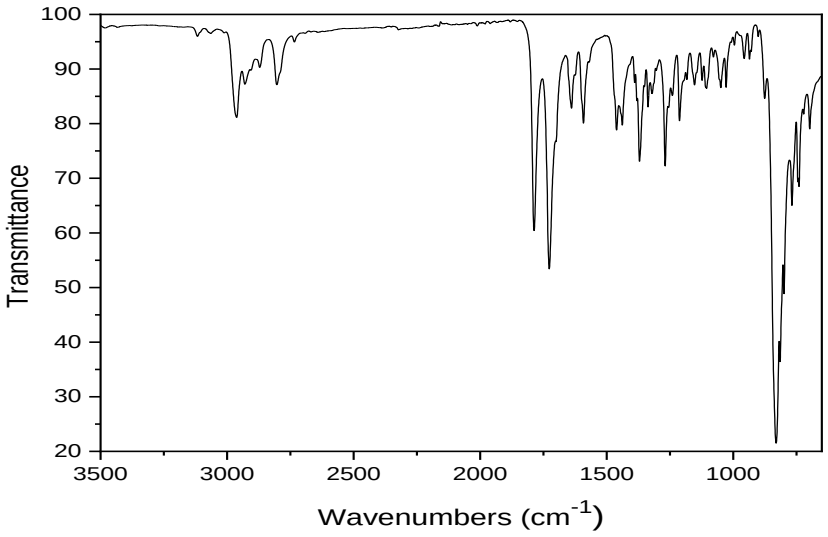

Figure S1. ATR-IR spectrum of **[1Fe(NO)$_2$]$^+$**.

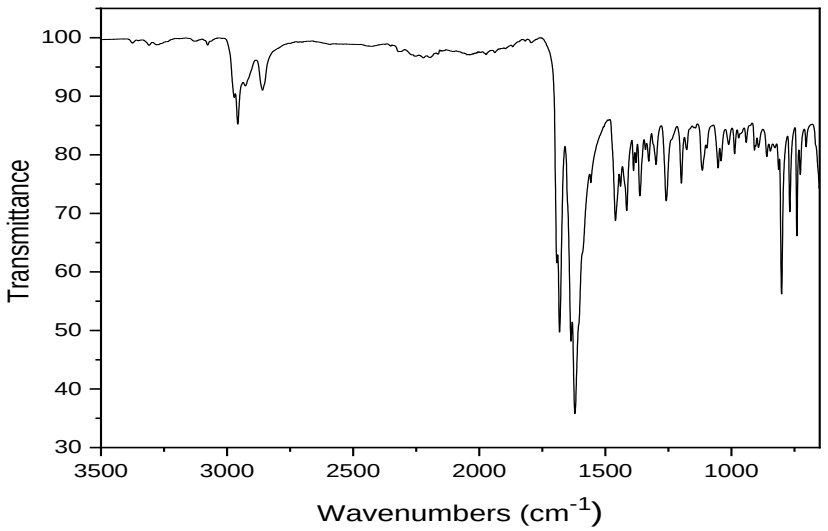

Figure S2. ATR-IR spectrum of **1Fe$_2$(NO)$_4$**.

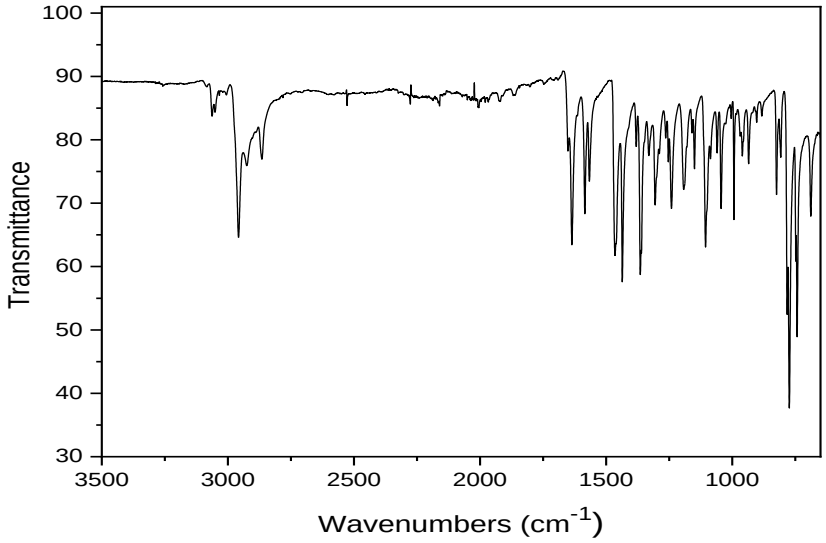

Figure S3. ATR-IR spectrum of ^{Ar}MIP (**L2**).

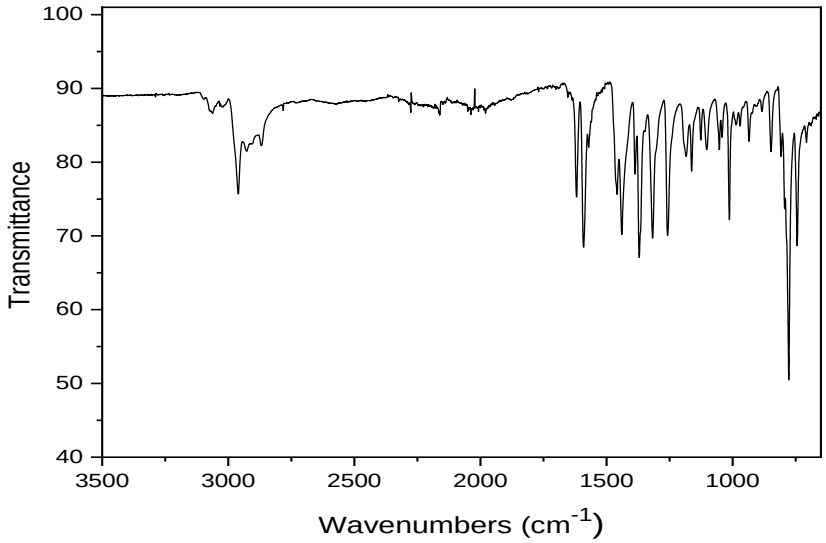

Figure S4. ATR-IR spectrum of **[2FeBr$_2$]$_2$**.

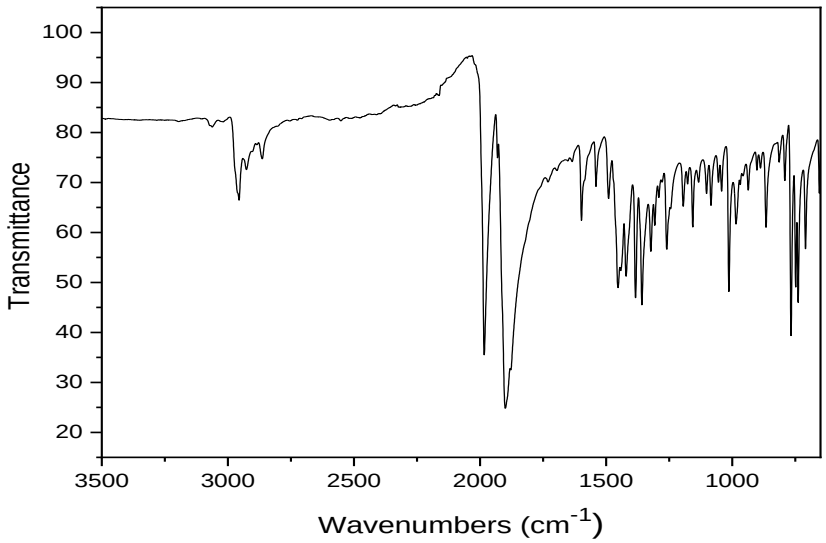

Figure S5. ATR-IR spectrum of **2Fe(CO)$_3$**.

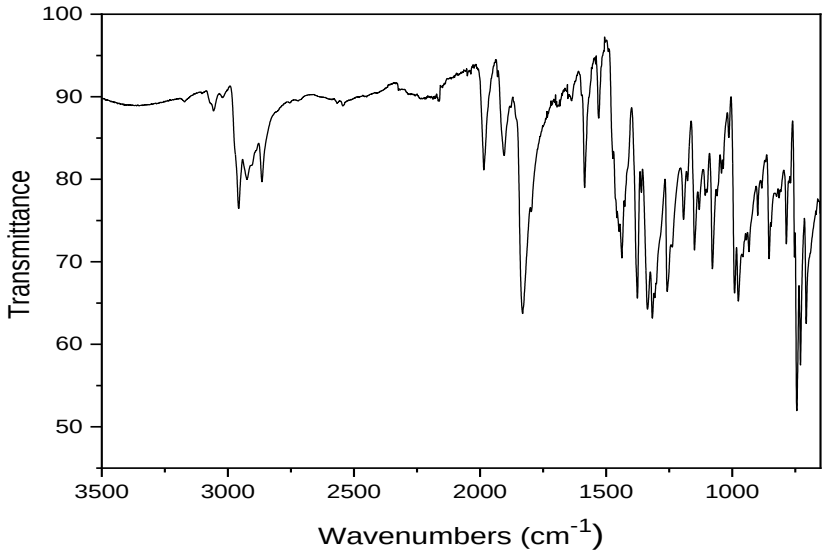

Figure S6. ATR-IR spectrum of **2$_2$Fe(CO)** , a small amount of **2Fe(CO)$_3$** is present as evidenced by the carbonyl stretches at 1985 and 1904 cm^{-1}.

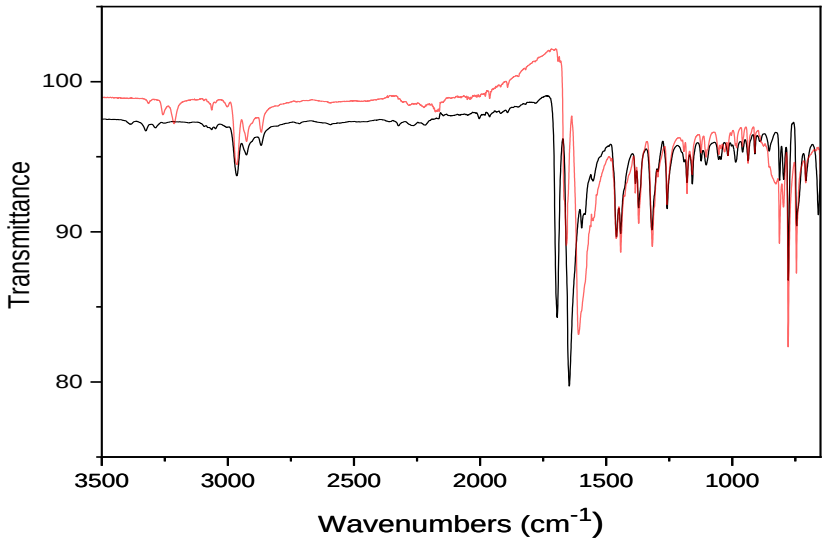

Figure S7. ATR-IR spectrum of **$2Fe(NO)_2$** with ^{15}N labeling of the nitrosyls shown in red.

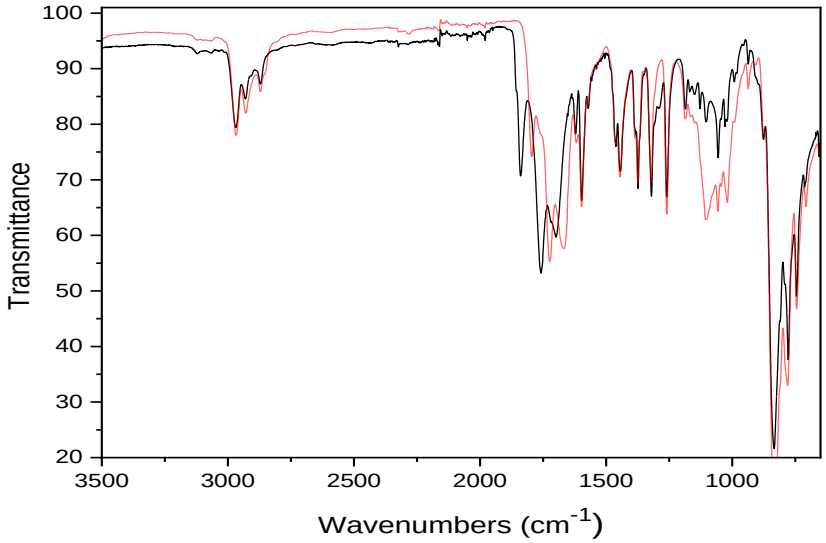

Figure S8. ATR-IR spectrum of **$[2Fe_2(NO)_4(PF_4)][PF_6]$** with ^{15}N labeling of the nitrosyls shown in red.

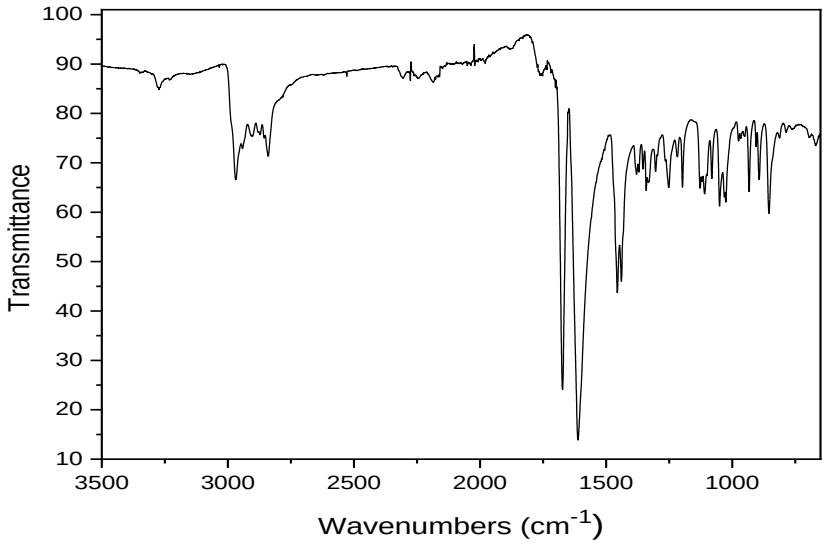

Figure S9. ATR-IR spectrum of **3Fe(NO)$_2$**.

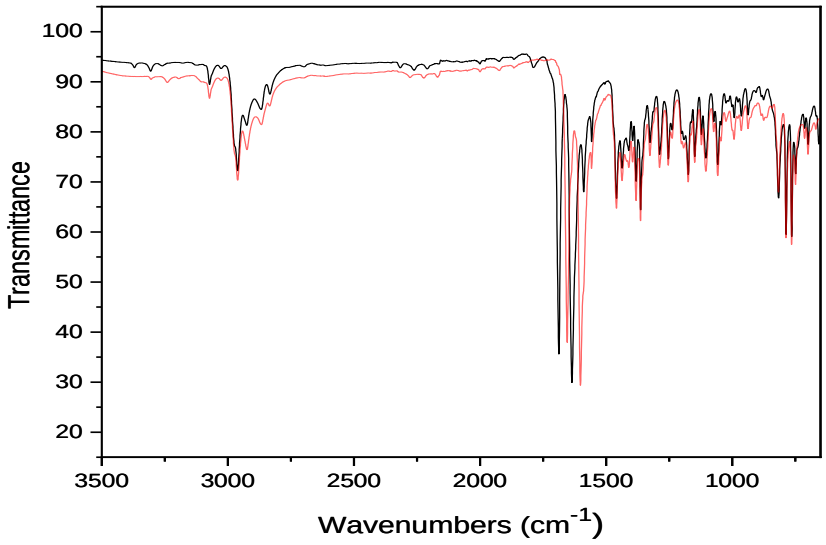

Figure S10. ATR-IR spectrum of **5Fe(NO)$_2$** with ^{15}N labeling of the nitrosyls shown in red.

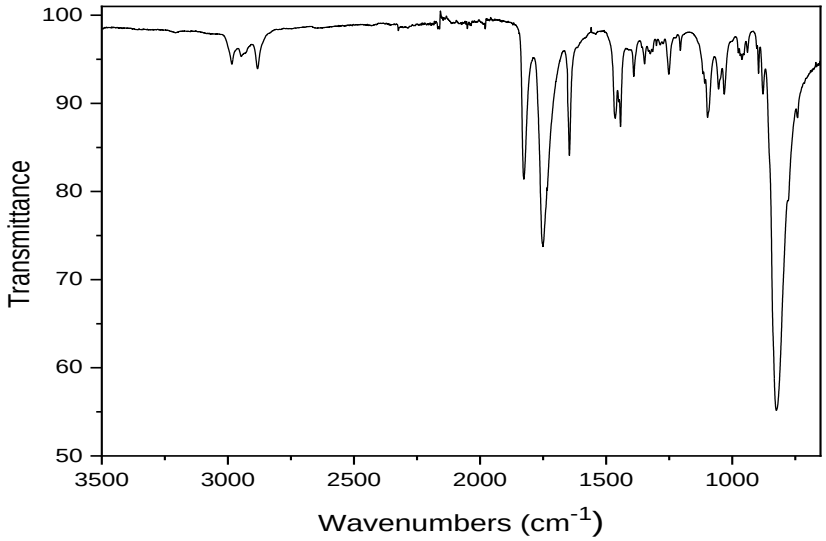

Figure S11. ATR-IR spectrum of **[3Fe(NO)$_2$][PF$_6$]** ($\nu_{C=N}$: 1646 cm^{-1}).

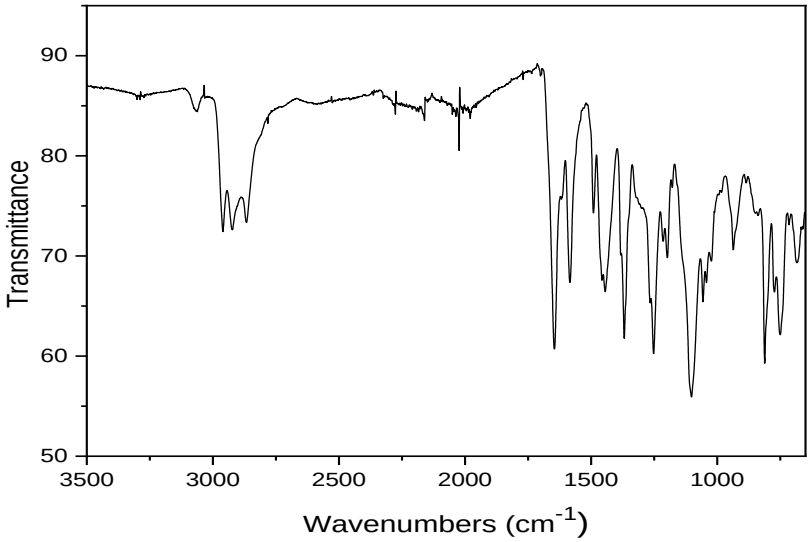

Figure S12. ATR-IR spectrum of **6FeBr$_2$.**

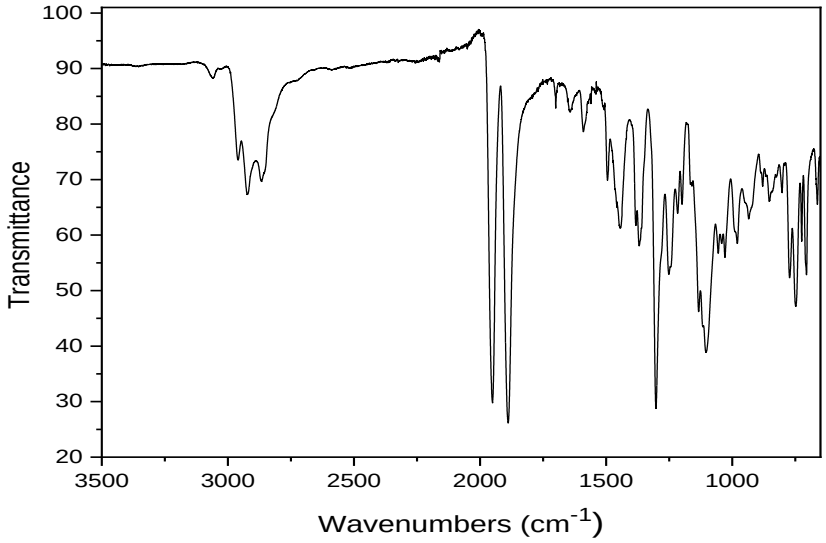

Figure S13. ATR-IR spectrum of **6Fe(CO)$_2$.**

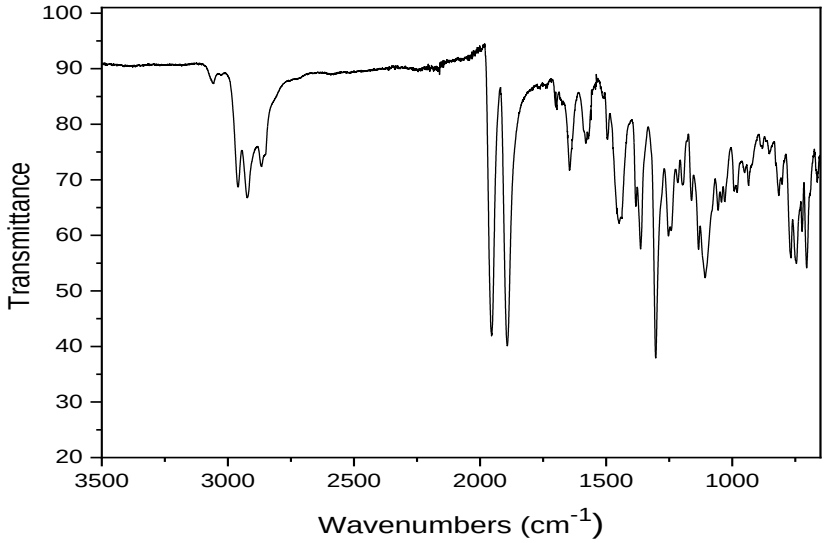

Figure S14. ATR-IR spectrum of **7Fe(CO)$_2$.**

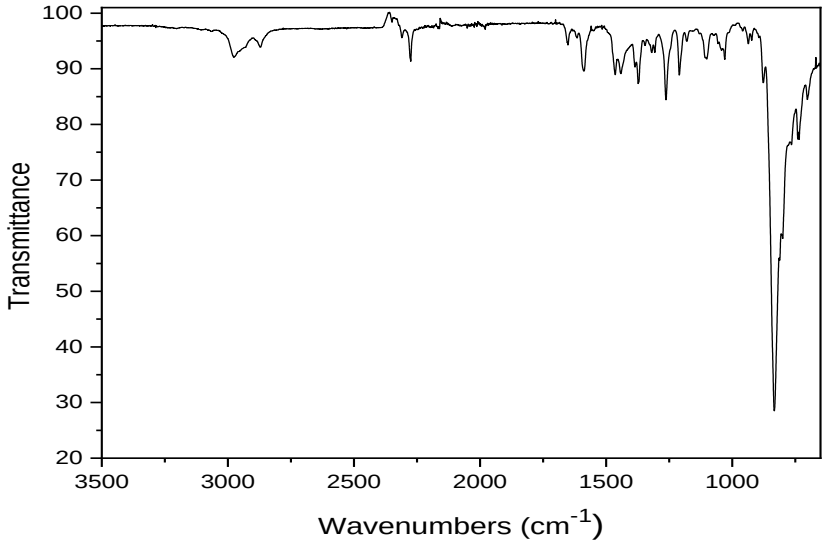

Figure S15. ATR-IR spectrum of **1Fe(PF_6)$_2$.**

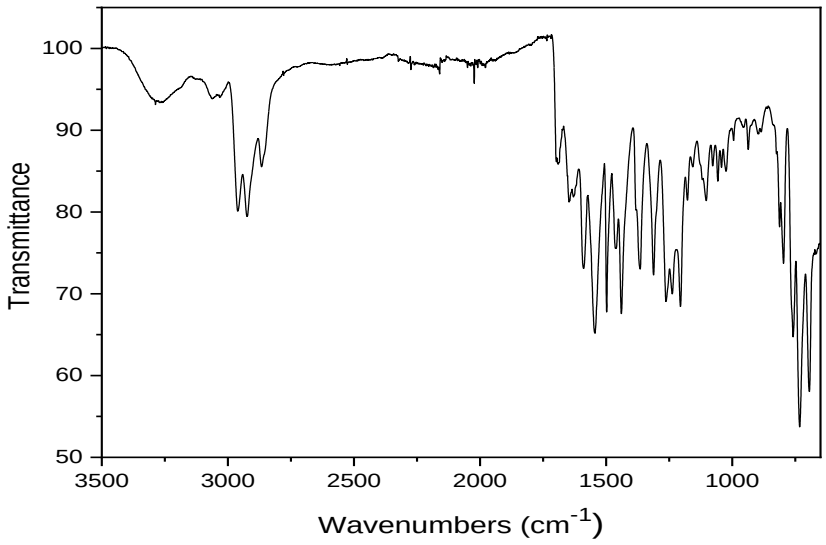

Figure S16. ATR-IR spectrum of **8FeBr_2.**

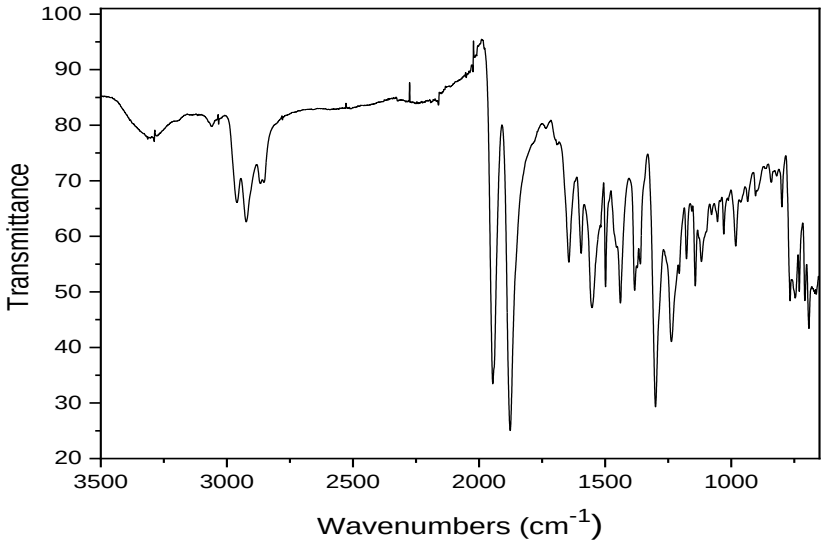

Figure S17. ATR-IR spectrum of **8Fe(CO)$_2$.**

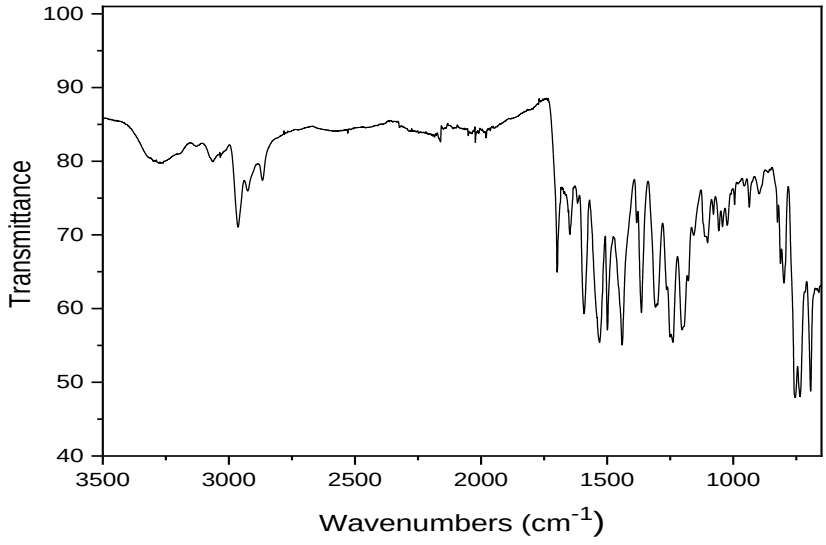

Figure S18. ATR-IR spectrum of **9FeBr$_2$.**

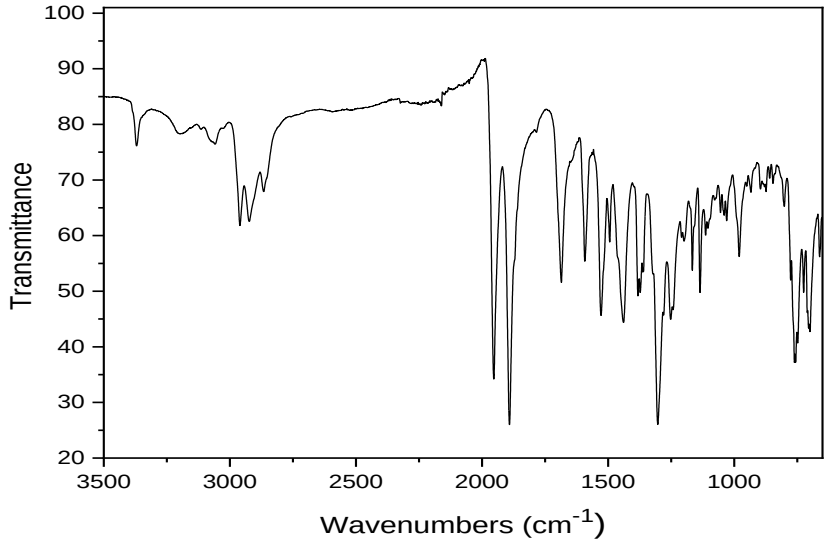

Figure S19. ATR-IR spectrum of **9Fe(CO)$_2$.**

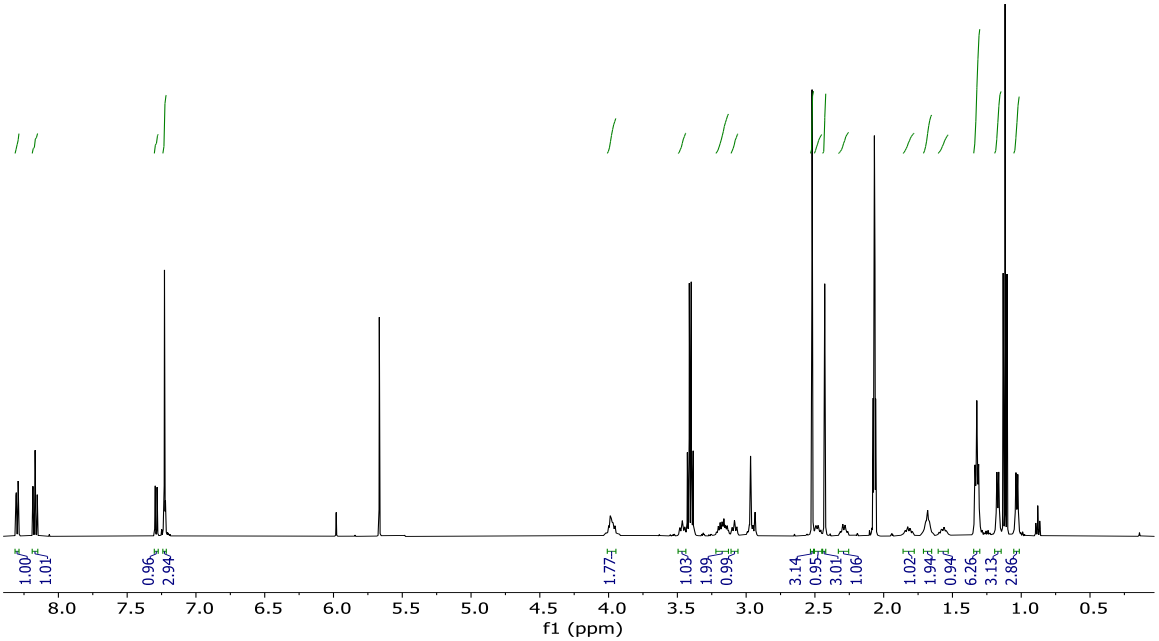

Figure S20. ^{1}H NMR (500 MHz) spectrum of **1Fe$_2$(NO)$_4$** in CD_3CN, CH_2Cl_2 and Et_2O contamination are present.

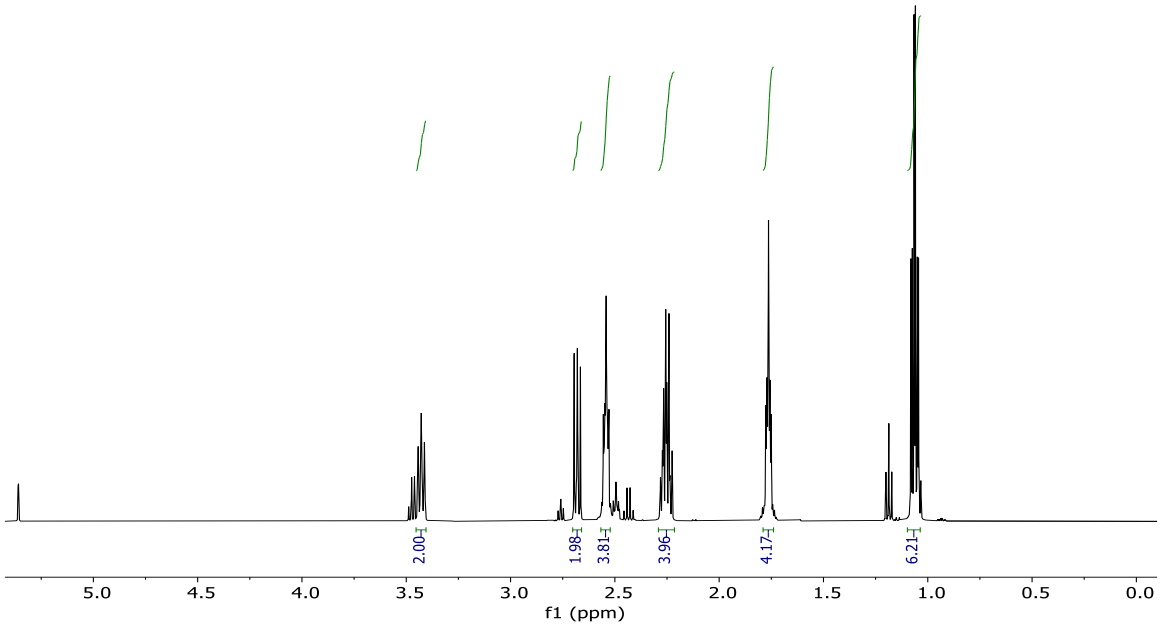

Figure S21. ^{1}H NMR (500 MHz) spectrum of ^{Pyrrol}Imine ligand in CD_2Cl_2.

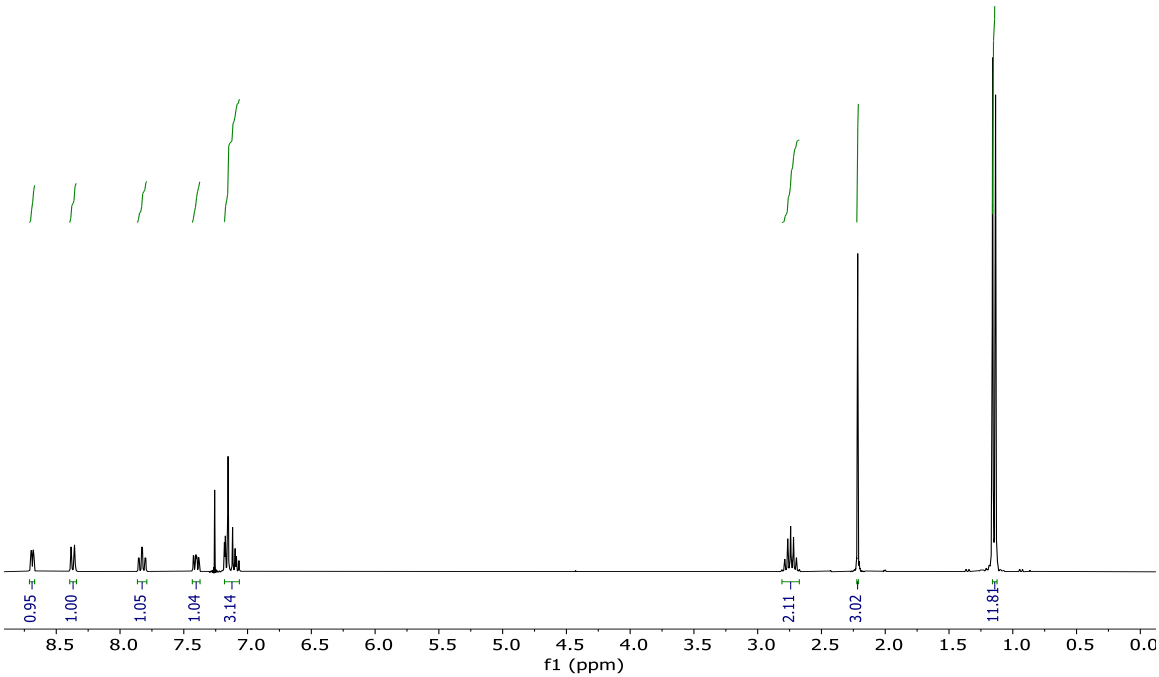

Figure S22. ^{1}H NMR (500 MHz) spectrum of ^{Ar}MIP (**L2**) ligand in $CDCl_3$.

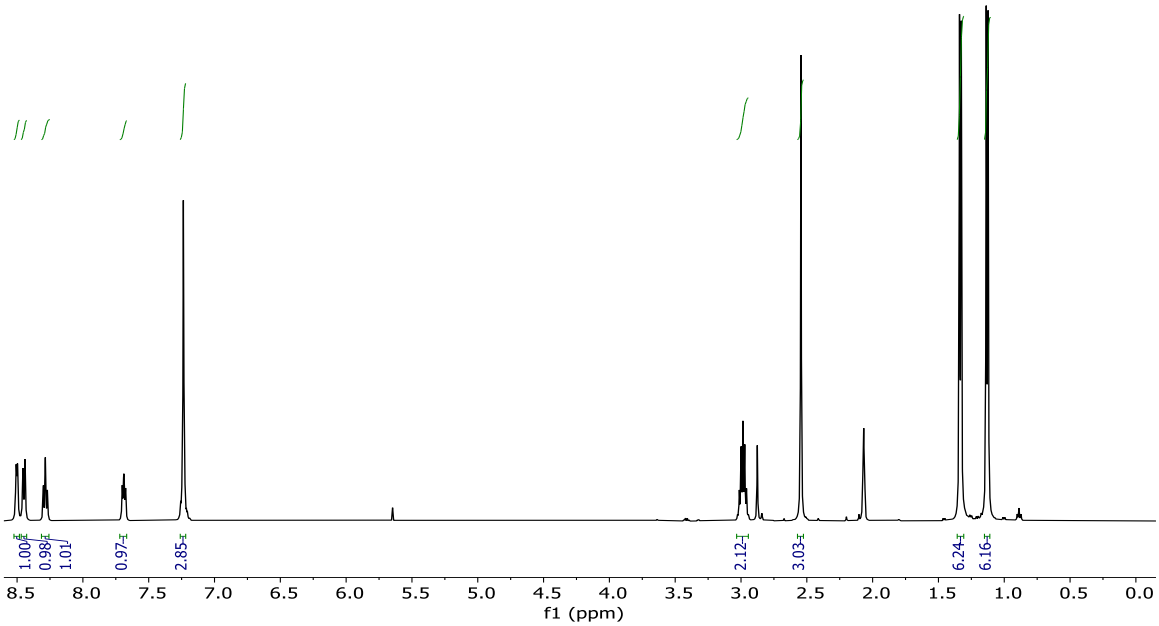

Figure S23. ^{1}H NMR (500 MHz) spectrum of **2Fe(NO)$_2$** in $(CD_3)_2C=O$.

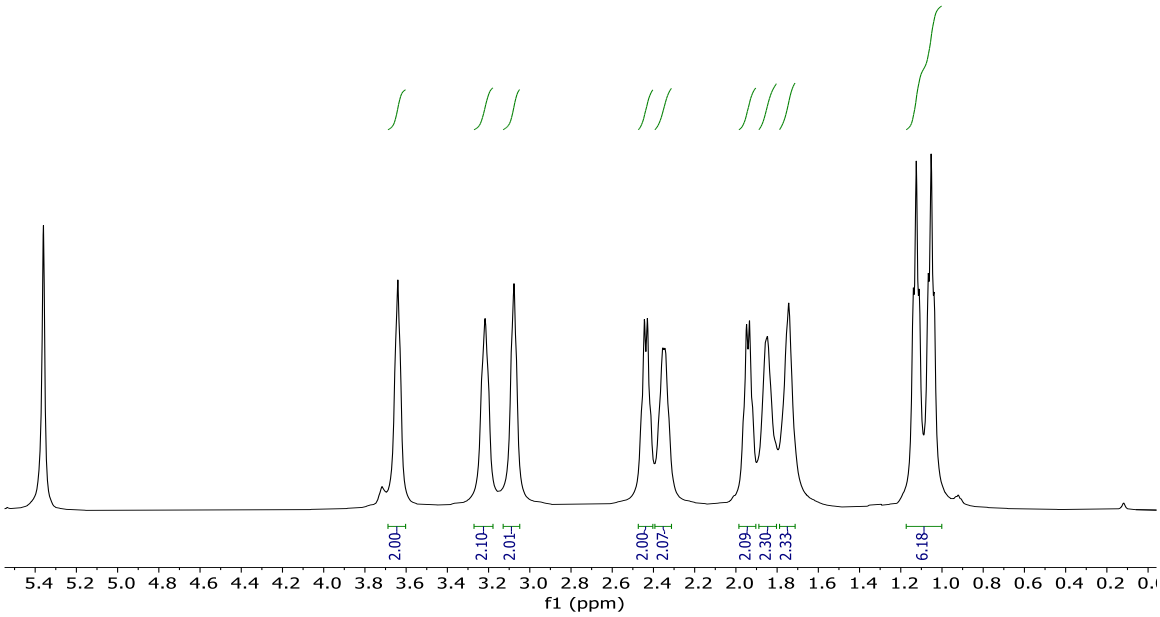

Figure S24. ^{1}H NMR (500 MHz) spectrum of **3Fe(NO)$_2$** in CD_2Cl_2.

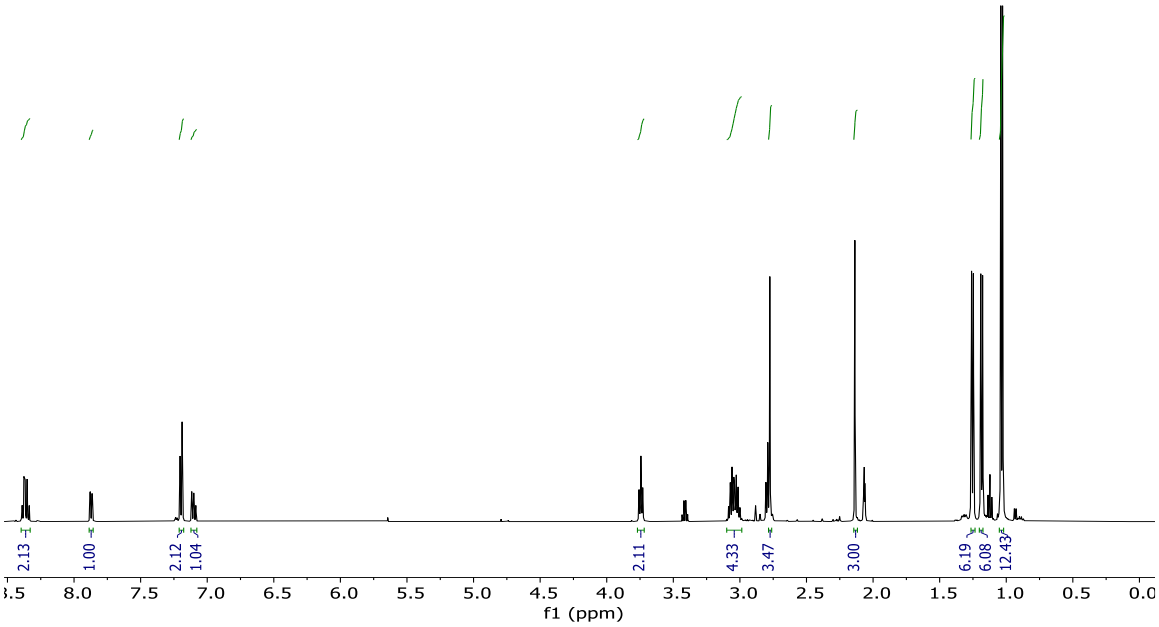

Figure S25. ^{1}H NMR (500 MHz) spectrum of **5Fe(NO)$_2$** in CD_3CN.

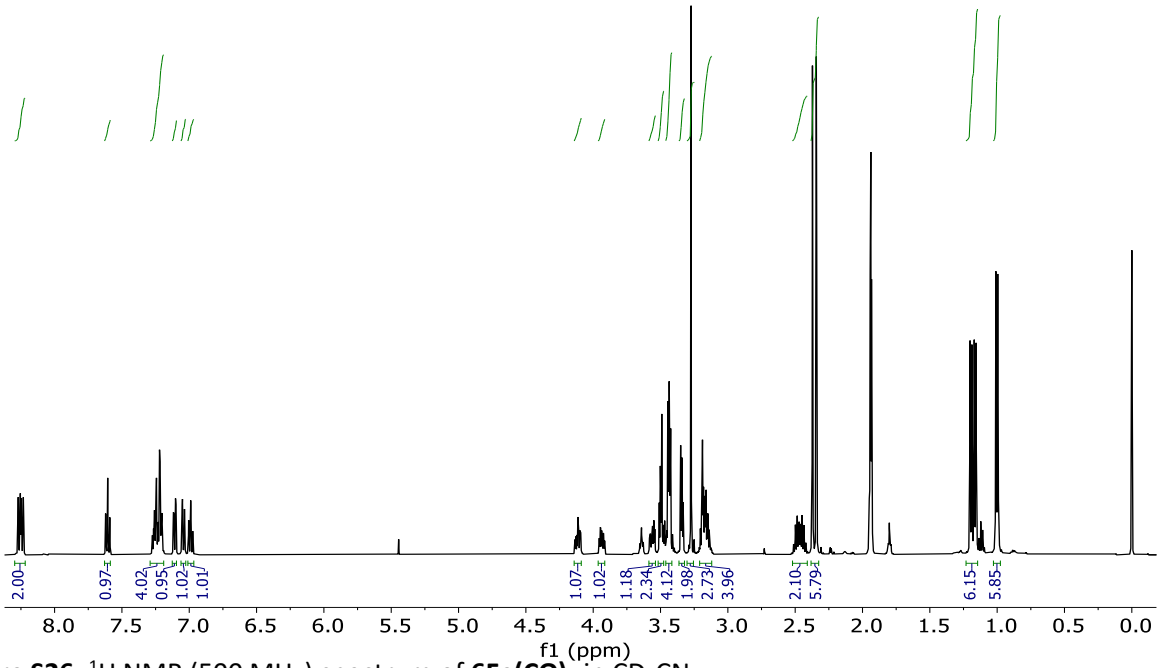

Figure S26. ^{1}H NMR (500 MHz) spectrum of **6Fe(CO)$_2$** in CD_3CN.

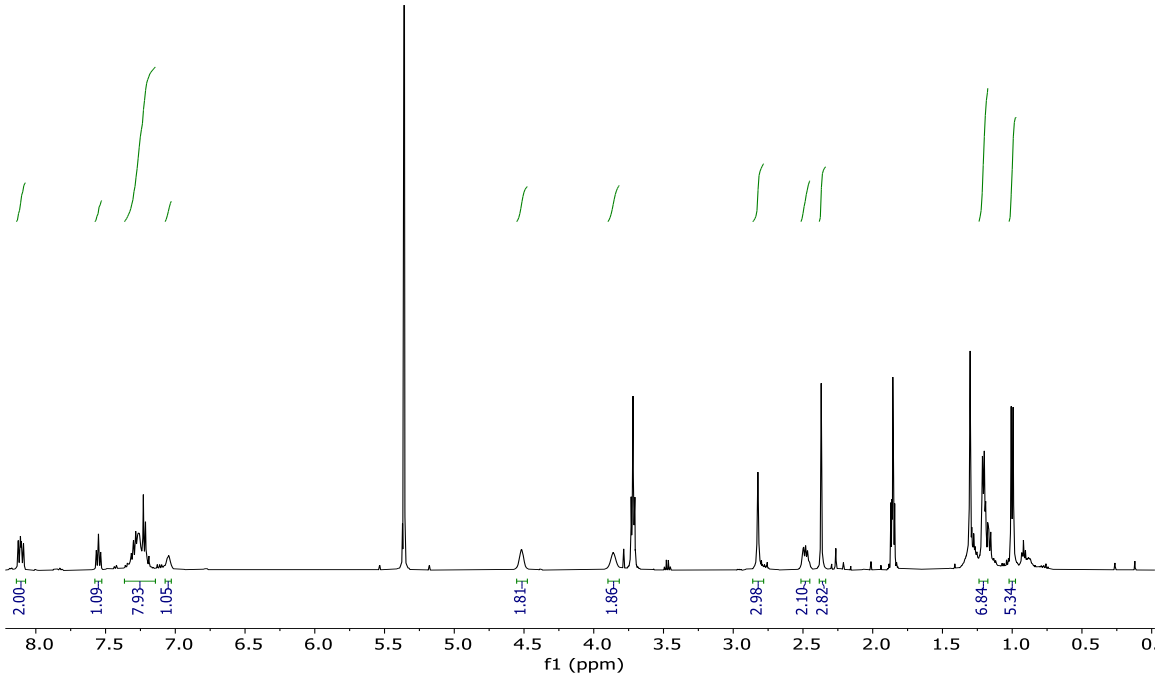

Figure S27. ^{1}H NMR (500 MHz) spectrum of **8Fe(CO)$_2$** in CD_3CN.

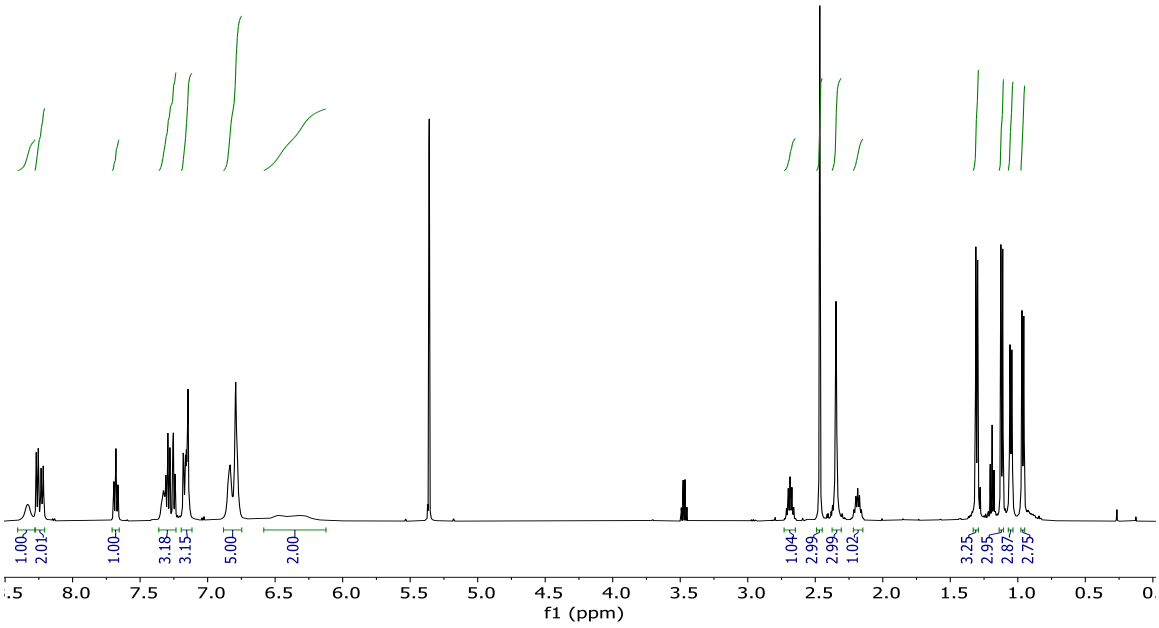

Figure S28. ^{1}H NMR (500 MHz) spectrum of **9Fe(CO)$_2$** in CD_2Cl_2.

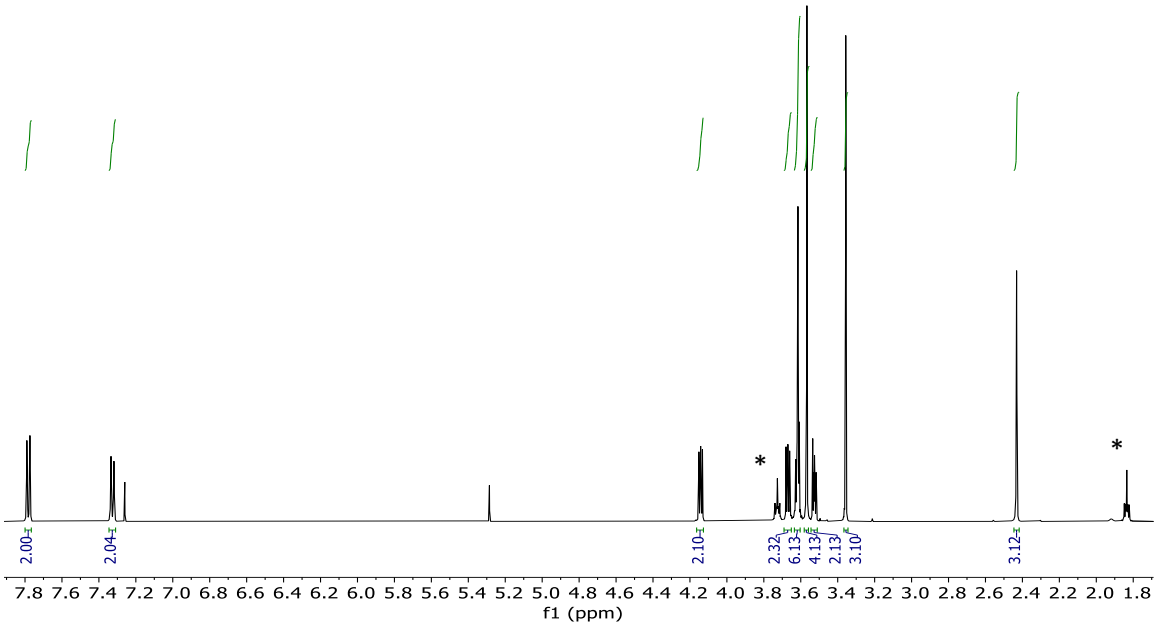

Figure S29. ^{1}H NMR (500 MHz) spectrum of **Tosyl tetraethyleneglycol monomethyl-ether** in $CDCl_3$, THF impurities marked with (*).

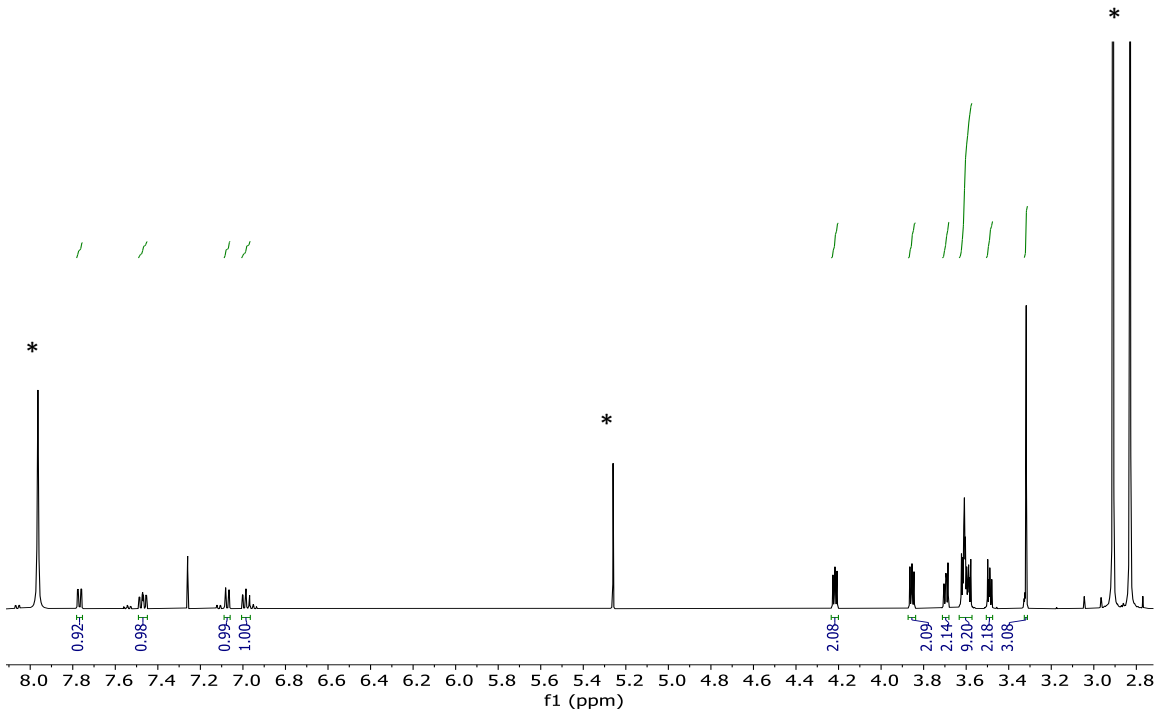

Figure S30. ^{1}H NMR (500 MHz) spectrum of **1-Nitro-(2-tetraethyleneglycol monomethyl-ether) benzene** in $CDCl_3$, DMF and CH_2Cl_2 impurities marked with (*).

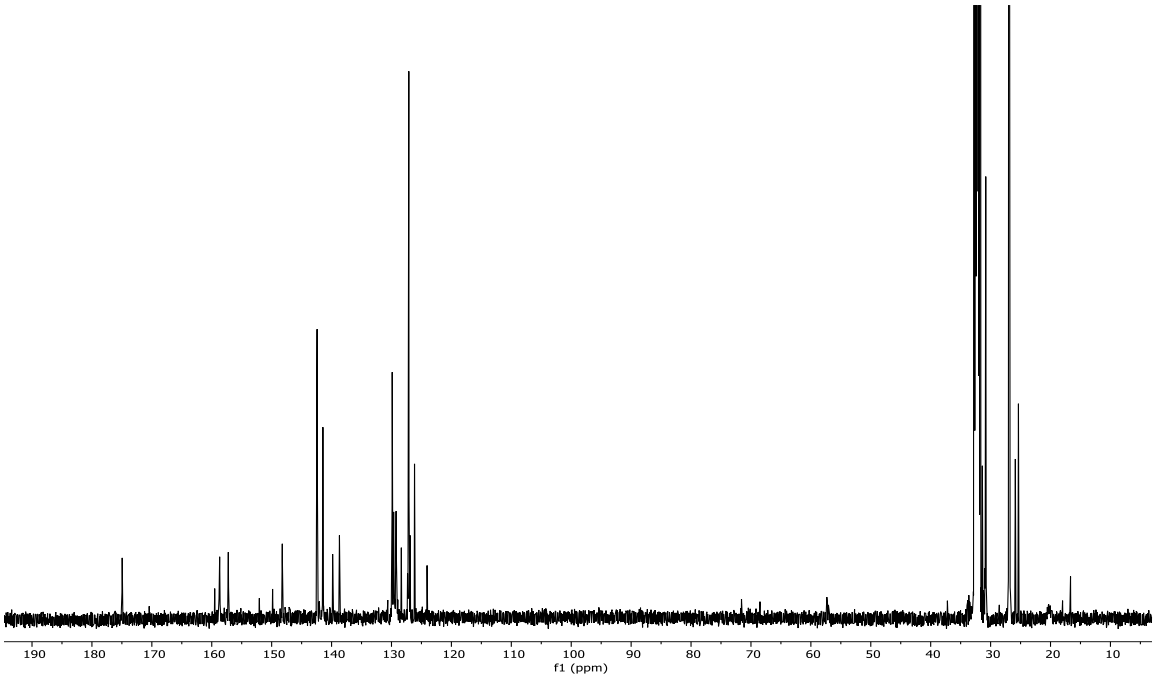

Figure S31. ^{13}C NMR (125 MHz) of **2Fe(NO)$_2$** in $(CD_3)_2C=O$.

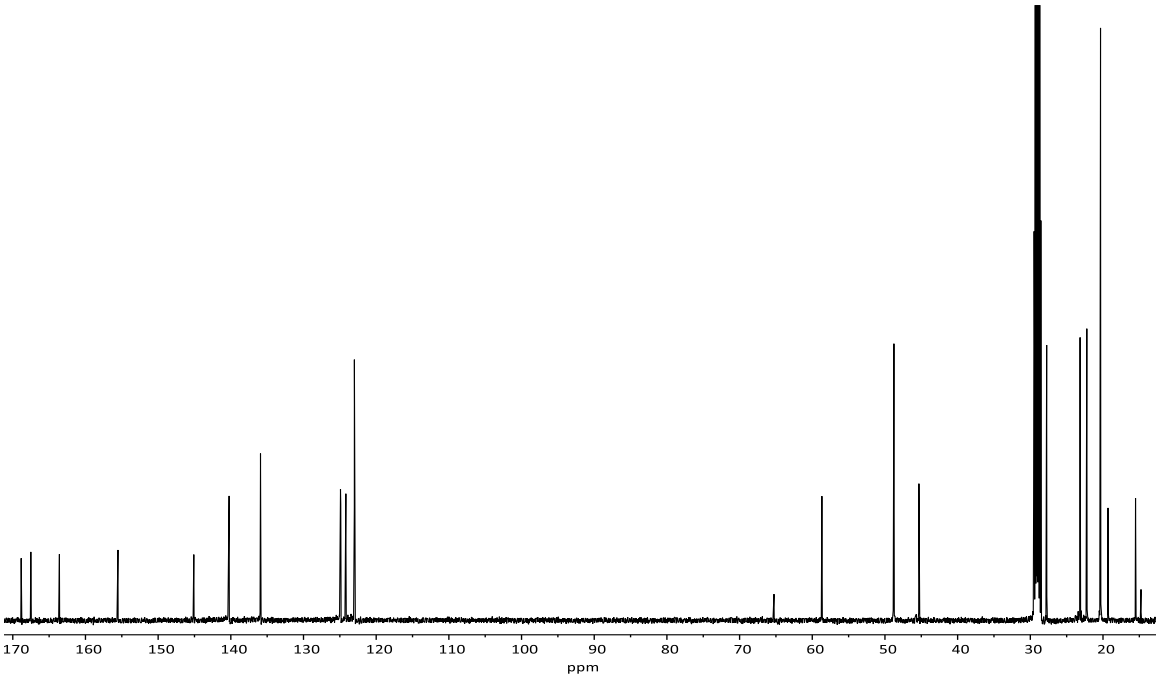

Figure S32. ^{13}C NMR (125 MHz) of **5Fe(CO)$_2$** in $(CD_3)_2C=O$.

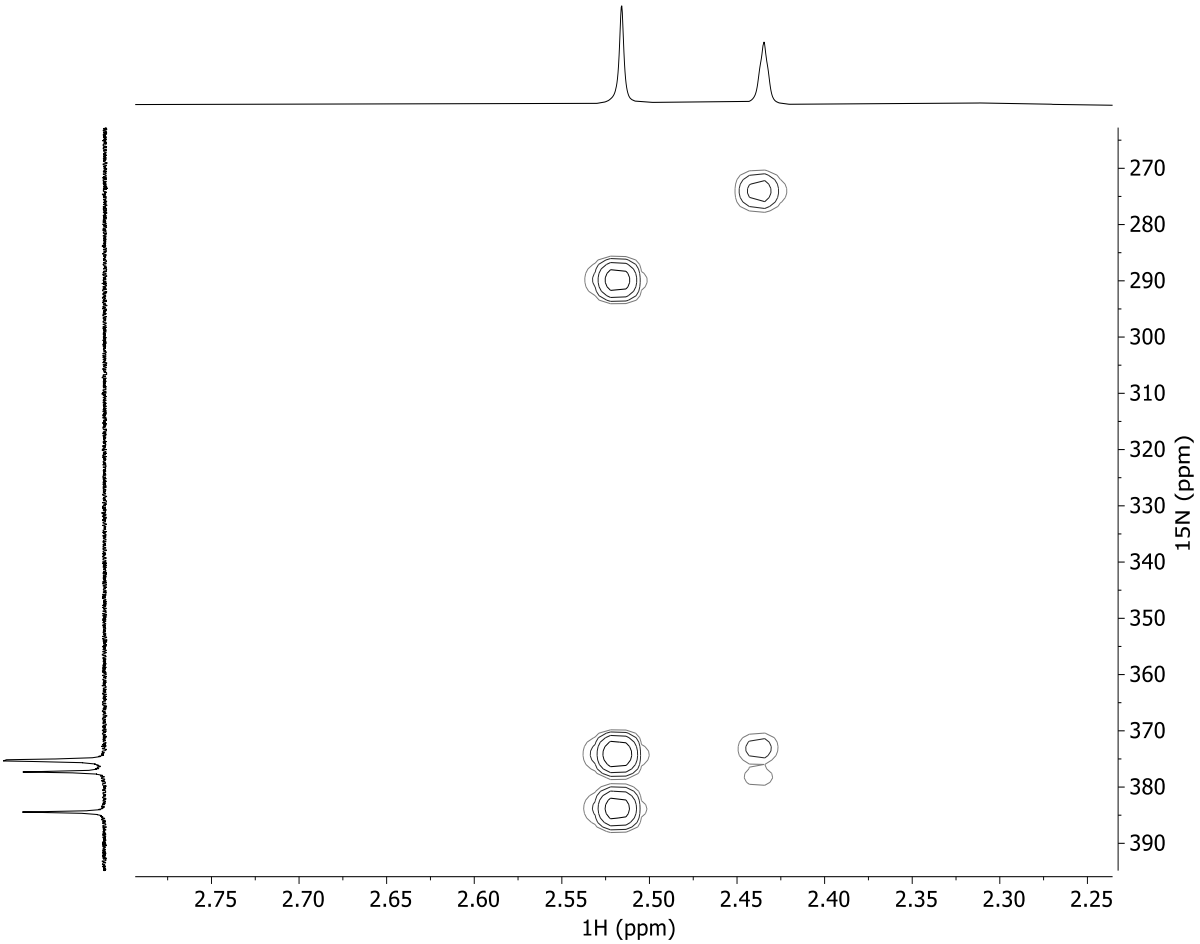

Figure S33. $^{1}H,^{15}N$ HMBC NMR of **$1Fe_2(NO)_4$** in $(CD_3)_2C=O$ showing correlation between the imine $–CH_3$ groups and the nitrosyls.

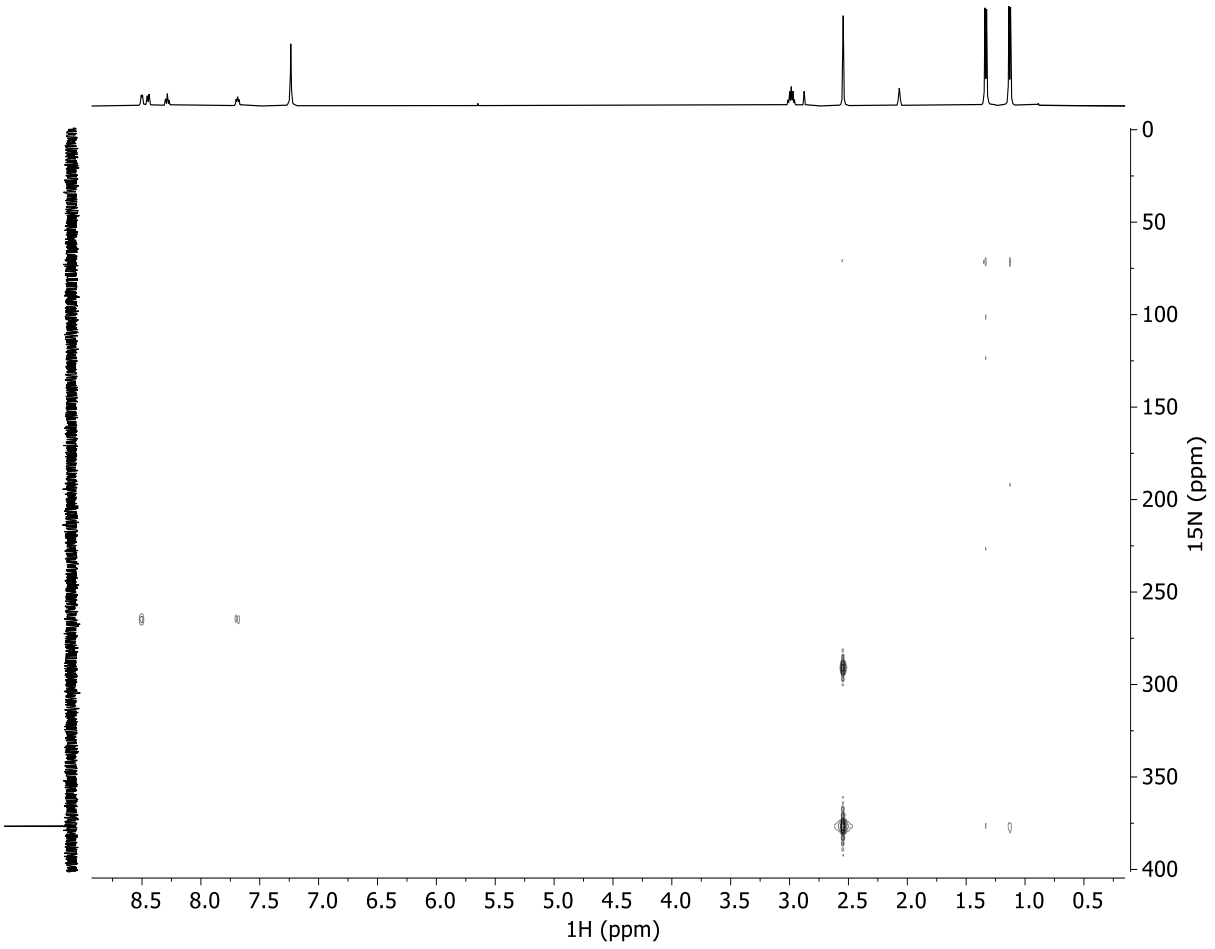

Figure S34. $^{1}H,^{15}N$ HMBC NMR of **$2Fe(NO)_2$** in $(CD_3)_2C=O$ showing correlation between the imine $–CH_3$ group and the nitrosyls.

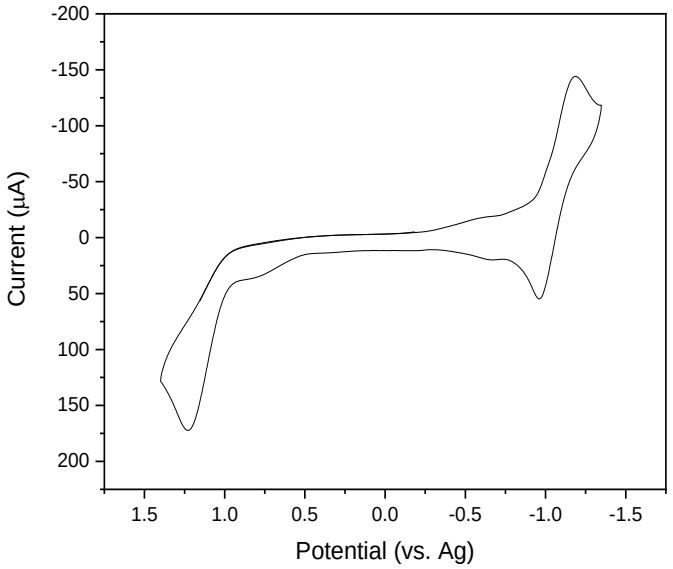

Figure S35. CV of **[1Fe(NO)][BPh_4]** (10 mM) in MeCN, glassy carbon working electrode, platinum counter electrode, with $TBAPF_6$ supporting electrolyte (100 mM), silver wire pseudo reference.

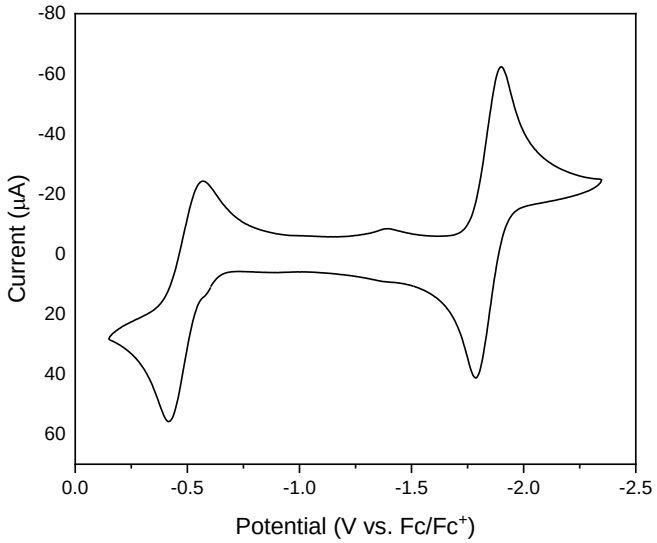

Figure S36. CV of **$2Fe(NO)_2$** (5 mM) in MeCN, glassy carbon working electrode, platinum counter electrode, and 100 mM $TBAPF_6$ supporting electrolyte.

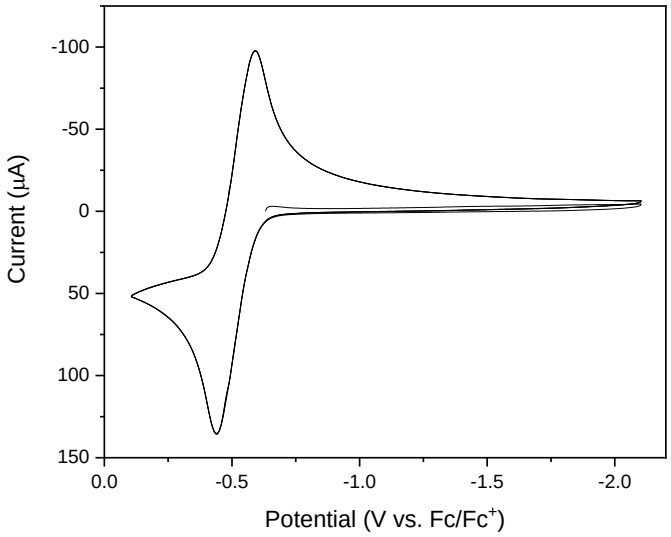

Figure S37. CV of **$3Fe(NO)_2$** (5 mM) in MeCN , glassy carbon working electrode, platinum counter electrode, and 100 mM $TBAPF_6$ supporting electrolyte.

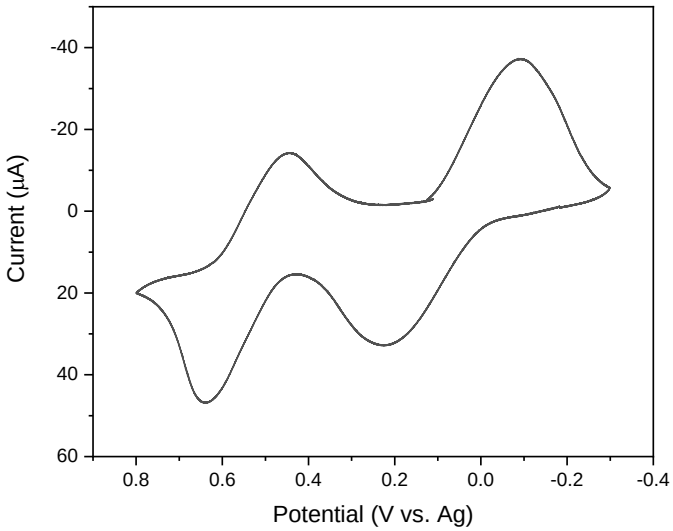

Figure 38. CV of **$4Fe_2(NO)_4$** (5 mM) in CH_2Cl_2, glassy carbon working electrode, platinum counter electrode, silver pseudo reference, scanning 10 mV/s.

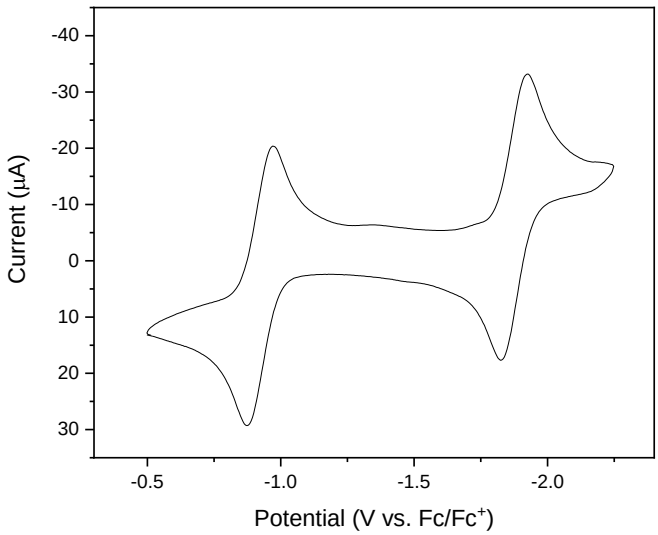

Figure S39. CV of **5Fe(NO)$_2$** (5 mM) in MeCN, glassy carbon working electrode, platinum counter electrode, and 100 mM $TBAPF_6$ supporting electrolyte.

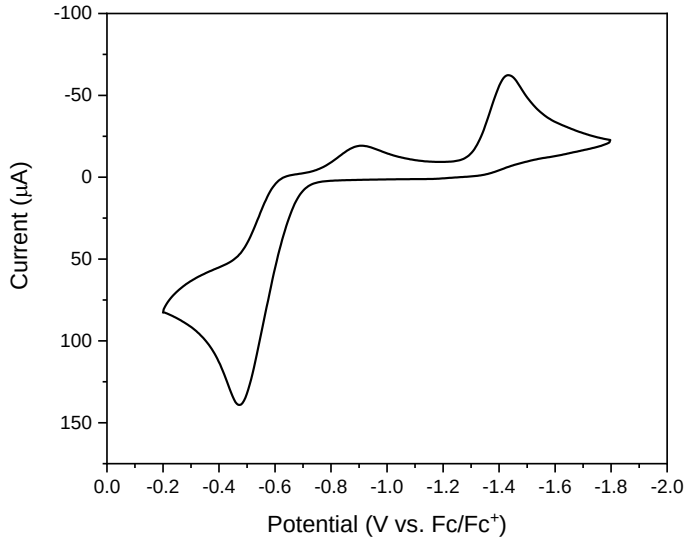

Figure S40. CV of **2Fe(CO)$_3$** (10 mM) in MeCN, glassy carbon working electrode, platinum counter electrode, and 100 mM $TBAPF_6$ supporting electrolyte.

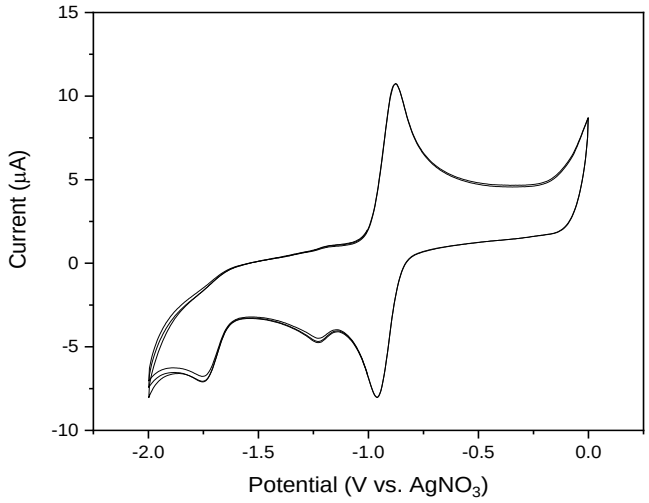

Figure S41. CV of crude **2_2Fe(CO)** in CH_2Cl_2, glassy carbon working electrode, platinum counter electrode, referenced to $Ag/AgNO_3$ 100 mM $TBAPF_6$ supporting electrolyte.

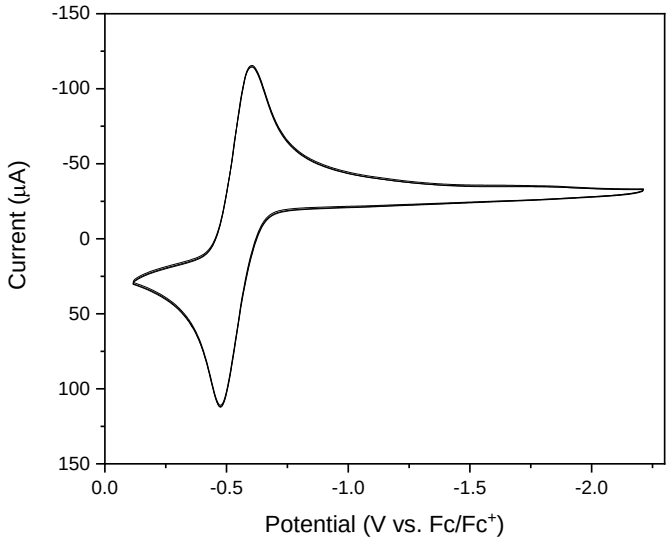

Figure S42. CV of **$3Fe(NO)_2$** (5 mM) in MeCN, glassy carbon working electrode, platinum counter electrode, and 100 mM $TBAPF_6$ supporting electrolyte.

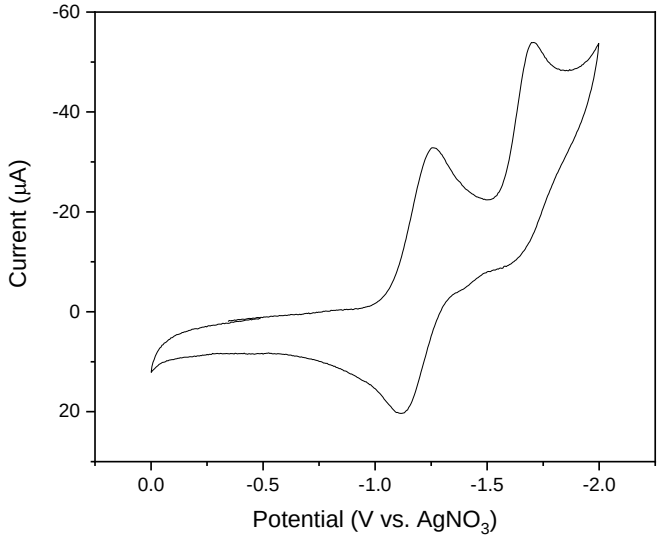

Figure S43. CV of **1Fe(PF$_6$)$_2$** (2.5 mM) in MeCN referenced to Ag/AgNO$_3$ glassy carbon working electrode, platinum counter electrode, 100 mM TBAPF$_6$ supporting electrolyte.

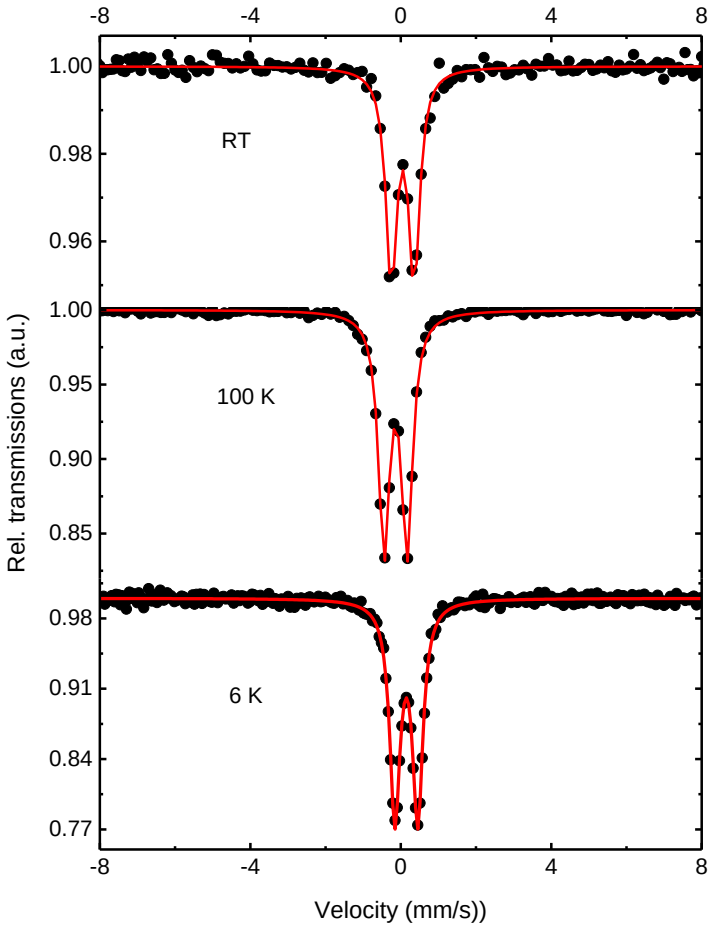

Figure S44. Variable temperature zero-field Mössbauer spectra of **$2Fe(NO)_2$**. (RT); δ = 0.154(3) mm/s, ΔE_Q =0.605(6) mm/s, Line width, Γ = 0.348(8) mm/s. . (100 K); δ = 0.238(2) mm/s, ΔE_Q = 0.610(2) mm/s, Line width, Γ =0.346(3) mm/s. . (6 K); δ =0.251(1) mm/s, ΔE_Q = 0.605(2) mm/s, Line width, Γ = 0.348(3) mm/s.

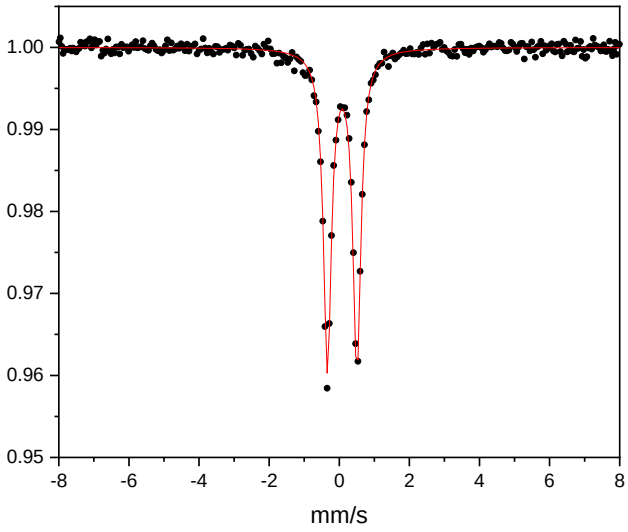

Figure S45. Zero-field Mössbauer spectrum of **3Fe(NO)$_2$**. Fit parameters: δ = 0.109(1); ΔE_Q = 0.842(4); Line width, Γ = 0.27(2).

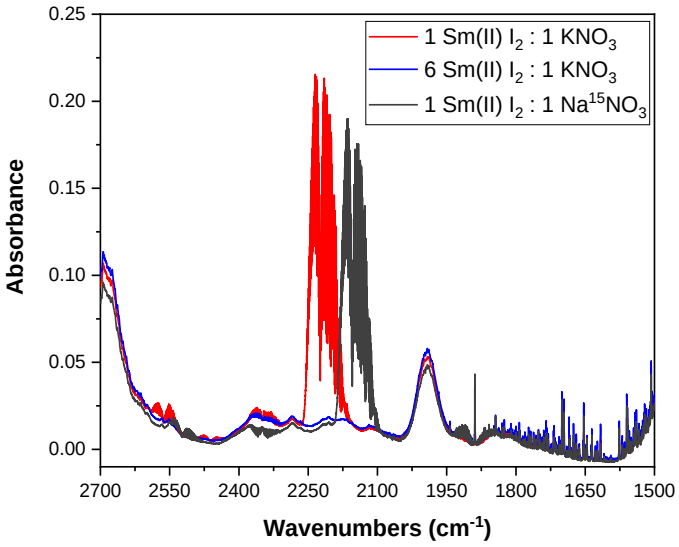

Figure S46. Gas-phase infrared absorption spectra of reaction headspace after reduction of potassium nitrate by 1 molar equivalent samarium diiodide in tetrahydrofuran (red trace) and 6 molar equivalents (red trace) respectively. Isotopic labeling shown in gray.

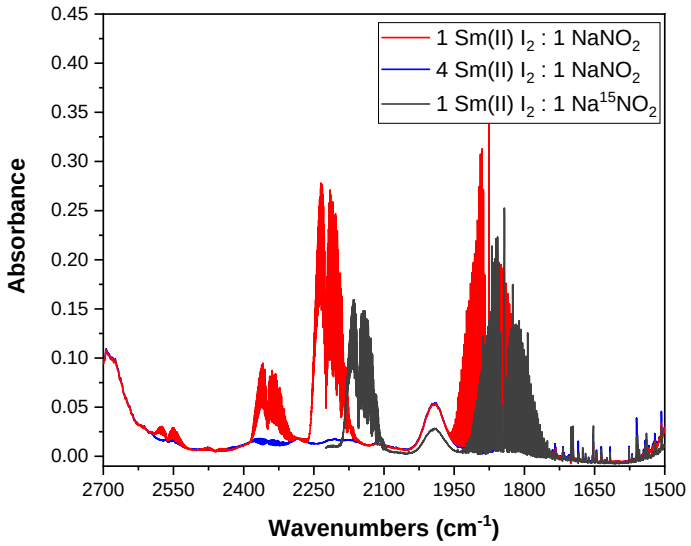

Figure S47. Gas-phase infrared absorption spectra of reaction headspace after reduction of sodium nitrite by 1 molar equivalent samarium diiodide in tetrahydrofuran (red trace) and 4 molar equivalents (red trace) respectively. Isotopic labeling shown in gray.

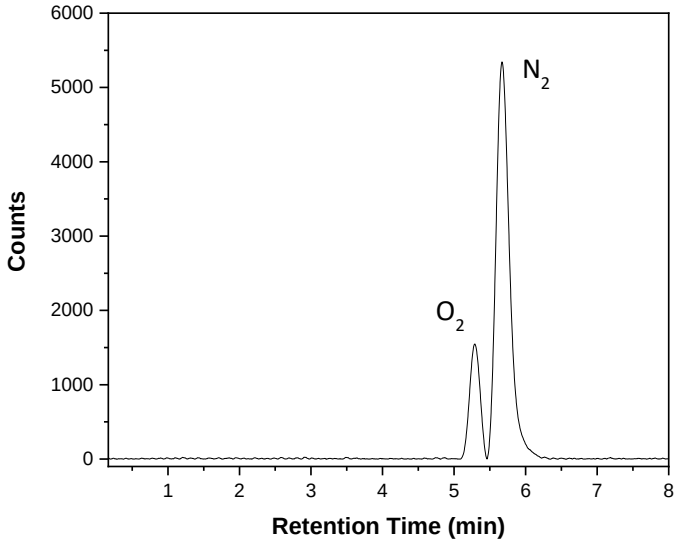

Figure S48. GC trace of air showing separation of oxygen and nitrogen.

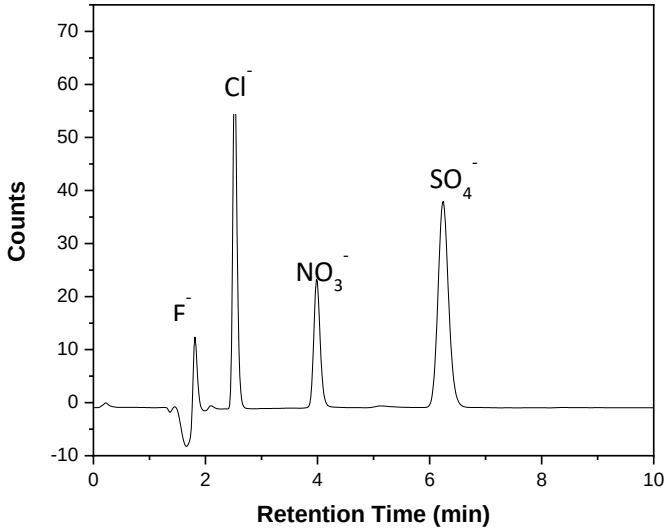

Figure S49. Ion chromatography standard of F^-, Cl^-, NO_3^-, and SO_4^- in nano-pure water.

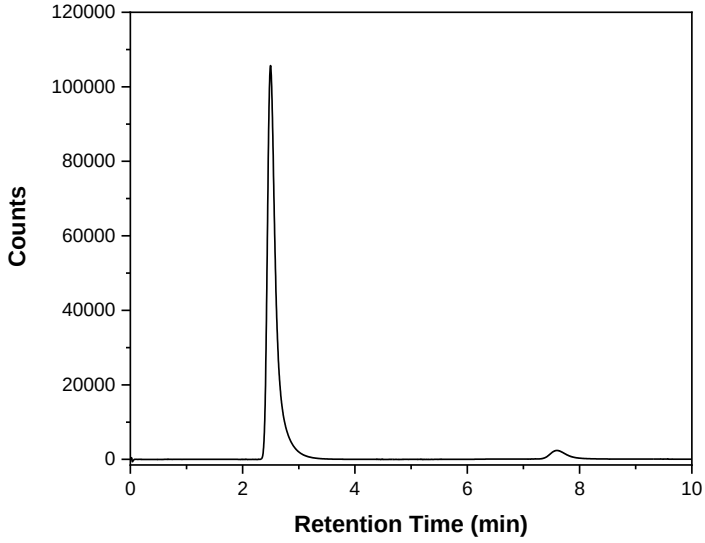

Figure S50. GC headspace analysis of **$1Fe_2(NO)_4$** (0.1051 g; 0.162 mmol) oxidation by ferrocenium hexafluorophosphate (0.0535 g; 0.162 mmol) in acetone. N_2O retention time 7.59 min.

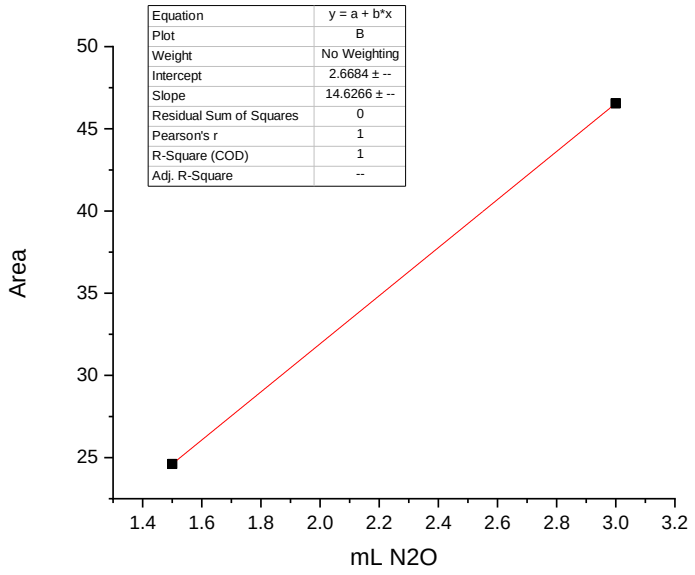

Figure S51. 2 Point "calibration" curve for the quantification of N_2O. Fit parameters are shown in the inset table.

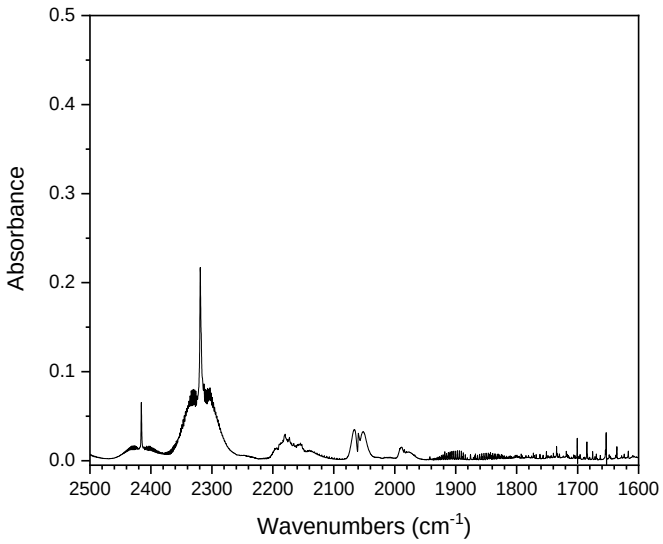

Figure S52. IR headspace of the oxidation of **$2Fe(NO)_2$** by ferrocenium hexafluorophosphate showing evolution of an unquantifiable amount of nitric oxide (1875 cm^{-1}).

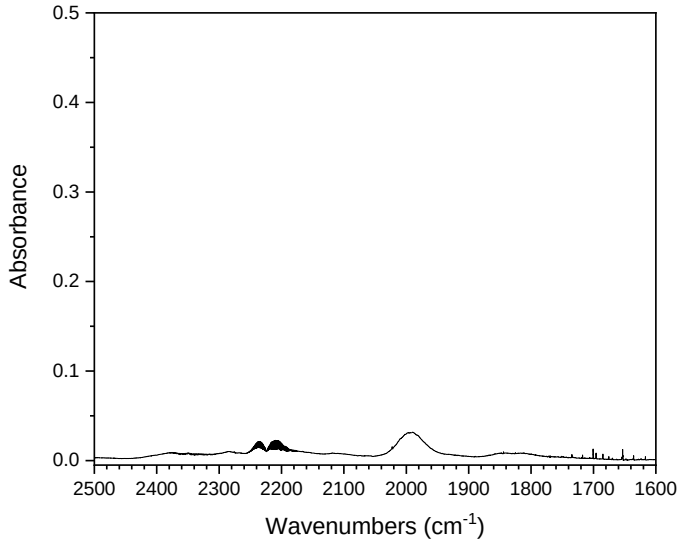

Figure S53. IR headspace of the oxidation of **3Fe(NO)$_2$** by ferrocenium hexafluorophosphate showing evolution of an unquantifiable amount of nitrous oxide (2224 cm^{-1}).

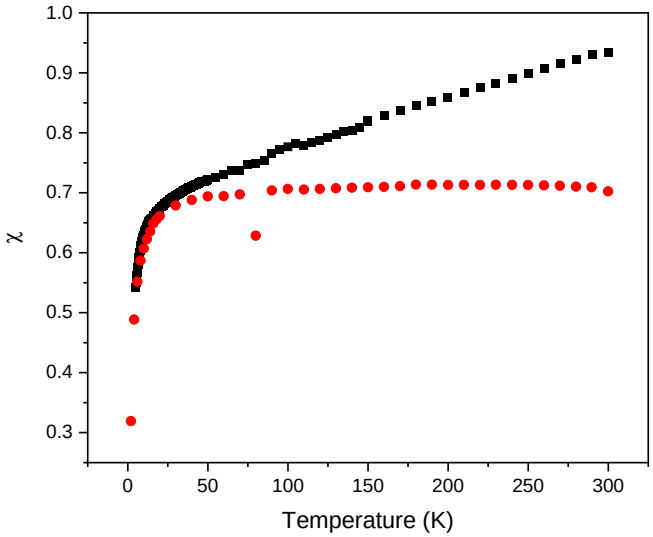

Figure S54. SQUID magnetic susceptibility plot of **[1Fe(NO)$_2$]$^+$** at 0.1 T (black) and 1 T (red), indicating a paramagnetic, iron-centered radical species.

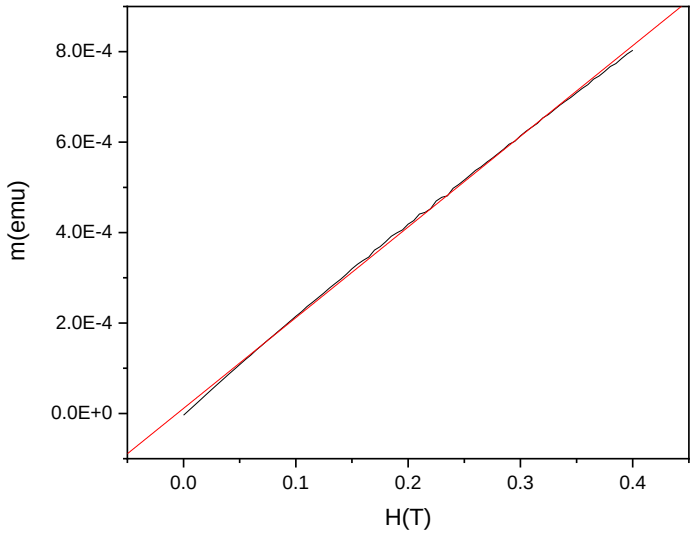

Figure S55. SQUID magnetization, M-H, plot of **[1Fe(NO)$_2$]$^+$.** Linear fit: y = 0.002x + 1E-5; R^2 = 0.9994.

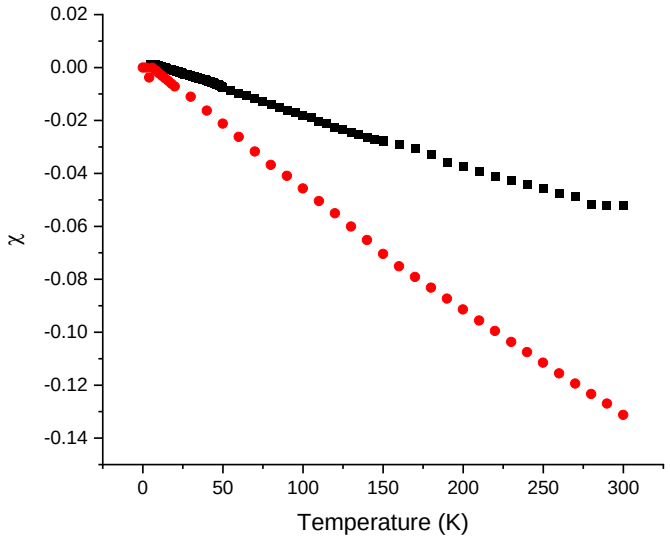

Figure S56. SQUID magnetic susceptibility plot of **1Fe$_2$(NO)$_4$** at 0.1 T (black) and 1 T (red), indicating a diamagnetic complex.

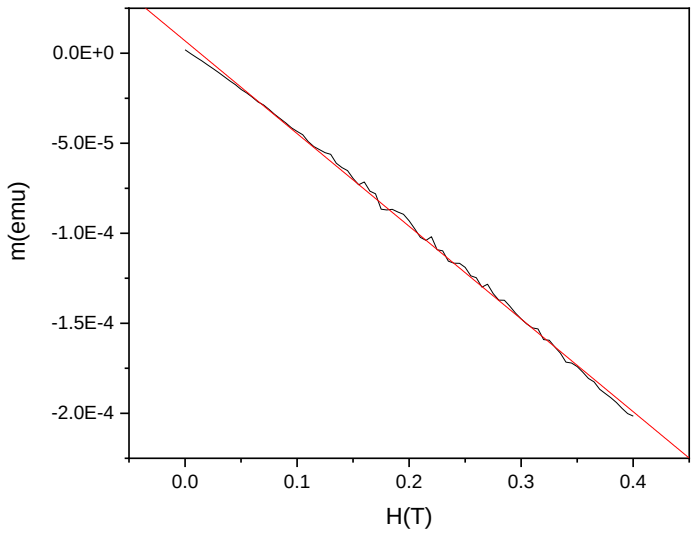

Figure S57. SQUID magnetization, M-H, plot of **$1Fe_2(NO)_4$.** Linear fit: y = -0.0005x + 7E-6. R^2 = 0.9987

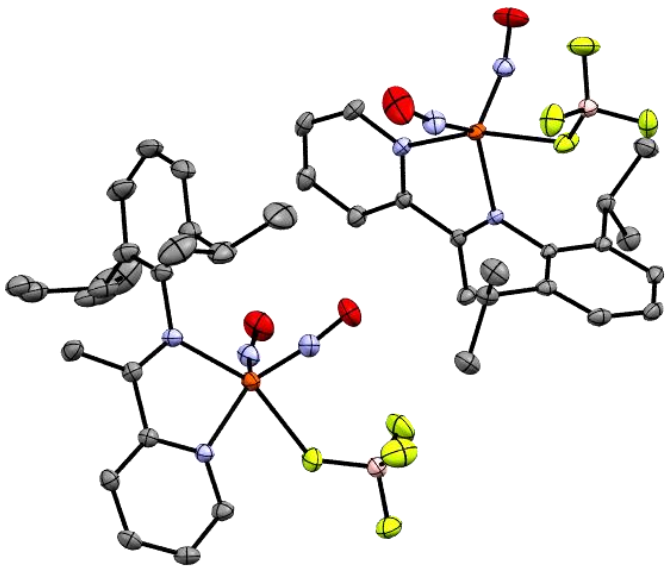

Figure S58. ORTEP view of **$2Fe(NO)_2(BF_4)$** showing the two different BF_4^- coordinations.

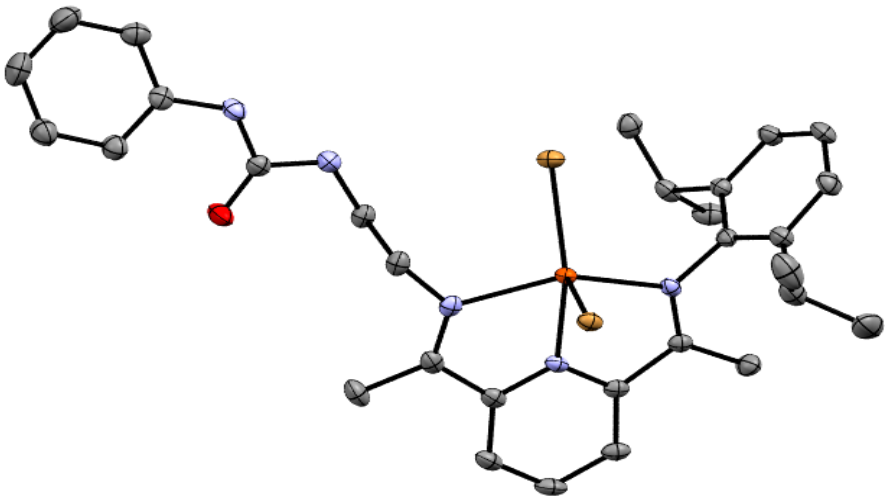

Figure S59. ORTEP view of **8FeBr$_2$**.

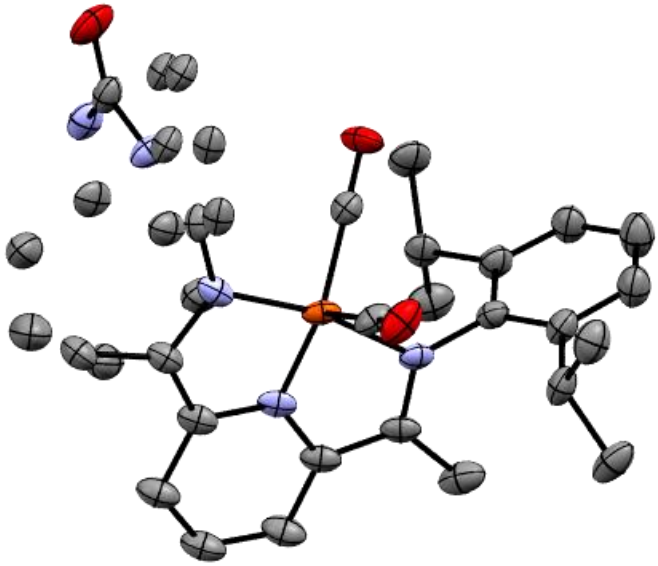

Figure S60. ORTEP view of **9Fe(CO)$_2$.**

References

(1) Walling, E.; Vaneeckhaute, C. Greenhouse Gas Emissions from Inorganic and Organic Fertilizer Production and Use: A Review of Emission Factors and Their Variability. *Journal of Environmental Management* **2020**, *276*, 111211. https://doi.org/10.1016/j.jenvman.2020.111211.

(2) Godfray, H. C. J. Food for Thought. *PNAS* **2011**, *108* (50), 19845–19846. https://doi.org/10.1073/pnas.1118568109.

(3) Lu, C.; Tian, H. Global Nitrogen and Phosphorus Fertilizer Use for Agriculture Production in the Past Half Century: Shifted Hot Spots and Nutrient Imbalance. *Earth System Science Data* **2017**, *9* (1), 181–192. https://doi.org/10.5194/essd-9-181-2017.

(4) Stewart, W. M.; Dibb, D. W.; Johnston, A. E.; Smyth, T. J. The Contribution of Commercial Fertilizer Nutrients to Food Production. *Agronomy Journal* **2005**, *97* (1), 1–6. https://doi.org/10.2134/agronj2005.0001.

(5) Mahmoud, M.; Kurdi, S.; Abay, kibrom; Breisinger, C. Too Much of a Good Thing? Evidence That Fertilizer Subsidies Lead to Overapplication in Egypt. **2020**. https://doi.org/10.2499/p15738coll2.133652.

(6) Byrareddy, V.; Kouadio, L.; Mushtaq, S.; Stone, R. Sustainable Production of Robusta Coffee under a Changing Climate: A 10-Year Monitoring of Fertilizer Management in Coffee Farms in Vietnam and Indonesia. *Agronomy* **2019**, *9* (9), 499. https://doi.org/10.3390/agronomy9090499.

(7) Cavigelli, M. A.; Grosso, S. J. D.; Liebig, M. A.; Snyder, C. S.; Fixen, P. E.; Venterea, R. T.; Leytem, A. B.; McLain, J. E.; Watts, D. B. US Agricultural Nitrous Oxide Emissions: Context, Status, and Trends. *Frontiers in Ecology and the Environment* **2012**, *10* (10), 537–546. https://doi.org/10.1890/120054.

(8) Venterea, R. T.; Halvorson, A. D.; Kitchen, N.; Liebig, M. A.; Cavigelli, M. A.; Grosso, S. J. D.; Motavalli, P. P.; Nelson, K. A.; Spokas, K. A.; Singh, B. P.; Stewart, C. E.; Ranaivoson, A.; Strock, J.; Collins, H. Challenges and Opportunities for Mitigating Nitrous Oxide Emissions from Fertilized Cropping Systems. *Frontiers in Ecology and the Environment* **2012**, *10* (10), 562–570. https://doi.org/10.1890/120062.

(9) Zhang, Y.; Dore, A. J.; Ma, L.; Liu, X. J.; Ma, W. Q.; Cape, J. N.; Zhang, F. S. Agricultural Ammonia Emissions Inventory and Spatial Distribution in the North China Plain. *Environmental Pollution* **2010**, *158* (2), 490–501. https://doi.org/10.1016/j.envpol.2009.08.033.

(10) Davidson, E. A.; Kanter, D. Inventories and Scenarios of Nitrous Oxide Emissions. *Environ. Res. Lett.* **2014**, *9* (10), 105012. https://doi.org/10.1088/1748-9326/9/10/105012.

(11) Conley, D. J.; Paerl, H. W.; Howarth, R. W.; Boesch, D. F.; Seitzinger, S. P.; Havens, K. E.; Lancelot, C.; Likens, G. E. Controlling Eutrophication: Nitrogen and Phosphorus. *Science* **2009**, *323* (5917), 1014–1015. https://doi.org/10.1126/science.1167755.

(12) McIsaac, G. F.; David, M. B.; Gertner, G. Z.; Goolsby, D. A. Nitrate Flux in the Mississippi River. *Nature* **2001**, *414* (6860), 166–167. https://doi.org/10.1038/35102672.

(13) Marks, W. R.; Baumgardner, D. F.; Reinheimer, E. W.; Gilbertson, J. D. Complete Denitrification of Nitrate and Nitrite to N2 Gas by Samarium(Ii) Iodide. *Chem. Commun.* **2020**, *56* (77), 11441–11444. https://doi.org/10.1039/D0CC04115G.

(14) C. Cabelof, A.; Carta, V.; G. Caulton, K. A Proton-Responsive Ligand Becomes a Dimetal Linker for Multisubstrate Assembly via Nitrate Deoxygenation. *Chemical Communications* **2021**, *57* (22), 2780–2783. https://doi.org/10.1039/D0CC07886G.
(15) Farah, C.; Michel, L. Y. M.; Balligand, J.-L. Nitric Oxide Signalling in Cardiovascular Health and Disease. *Nature Reviews Cardiology* **2018**, *15* (5), 292–316. https://doi.org/10.1038/nrcardio.2017.224.
(16) Fischmann, T. O.; Hruza, A.; Niu, X. D.; Fossetta, J. D.; Lunn, C. A.; Dolphin, E.; Prongay, A. J.; Reichert, P.; Lundell, D. J.; Narula, S. K.; Weber, P. C. Structural Characterization of Nitric Oxide Synthase Isoforms Reveals Striking Active-Site Conservation. *Nature Structural Biology* **1999**, *6* (3), 233–242. https://doi.org/10.1038/6675.
(17) Knowles, R. G.; Moncada, S. Nitric Oxide Synthases in Mammals. *Biochem J* **1994**, *298* (2), 249–258. https://doi.org/10.1042/bj2980249.
(18) Jansson, E. A.; Huang, L.; Malkey, R.; Govoni, M.; Nihlén, C.; Olsson, A.; Stensdotter, M.; Petersson, J.; Holm, L.; Weitzberg, E.; Lundberg, J. O. A Mammalian Functional Nitrate Reductase That Regulates Nitrite and Nitric Oxide Homeostasis. *Nat Chem Biol* **2008**, *4* (7), 411–417. https://doi.org/10.1038/nchembio.92.
(19) Ahmad, A.; Dempsey, S. K.; Daneva, Z.; Azam, M.; Li, N.; Li, P.-L.; Ritter, J. K. Role of Nitric Oxide in the Cardiovascular and Renal Systems. *Int J Mol Sci* **2018**, *19* (9). https://doi.org/10.3390/ijms19092605.
(20) Huerta, S. Nitric Oxide for Cancer Therapy. *Future Sci OA* **2015**, *1* (1). https://doi.org/10.4155/fso.15.44.
(21) Ren, B.; Zhang, N.; Yang, J.; Ding, H. Nitric Oxide-Induced Bacteriostasis and Modification of Iron-Sulphur Proteins in Escherichia Coli. *Molecular Microbiology* **2008**, *70* (4), 953–964. https://doi.org/10.1111/j.1365-2958.2008.06464.x.
(22) Johnson, D. C.; Dean, D. R.; Smith, A. D.; Johnson, M. K. Structure, Function, and Formation of Biological Iron-Sulfur Clusters. *Annu Rev Biochem* **2005**, *74*, 247–281. https://doi.org/10.1146/annurev.biochem.74.082803.133518.
(23) Kennedy, M. C.; Antholine, W. E.; Beinert, H. An EPR Investigation of the Products of the Reaction of Cytosolic and Mitochondrial Aconitases with Nitric Oxide. *J. Biol. Chem.* **1997**, *272* (33), 20340–20347. https://doi.org/10.1074/jbc.272.33.20340.
(24) Suryo Rahmanto, Y.; Kalinowski, D. S.; Lane, D. J. R.; Lok, H. C.; Richardson, V.; Richardson, D. R. Nitrogen Monoxide (NO) Storage and Transport by Dinitrosyl-Dithiol-Iron Complexes: Long-Lived NO That Is Trafficked by Interacting Proteins. *J Biol Chem* **2012**, *287* (10), 6960–6968. https://doi.org/10.1074/jbc.R111.329847.
(25) Hickok, J. R.; Sahni, S.; Shen, H.; Arvind, A.; Antoniou, C.; Fung, L. W. M.; Thomas, D. D. Dinitrosyliron Complexes Are the Most Abundant Nitric Oxide-Derived Cellular Adduct: Biological Parameters of Assembly and Disappearance. *Free Radical Biology and Medicine* **2011**, *51* (8), 1558–1566. https://doi.org/10.1016/j.freeradbiomed.2011.06.030.
(26) Liaw, W.-F.; Tsou, C.-C.; Tsai, M.-L. Dinitrosyl Iron Complexes (DNICs): From Biomimetic Synthesis and Spectroscopic Characterization toward Unveiling the Biological and Catalytic Roles of DNICs. *Acc. Chem. Res.* **2015**, *48*, 1184–1193. https://doi.org/10.1021/ar500459j.

(27) Rogers, P. A.; Eide, L.; Klungland, A.; Ding, H. Reversible Inactivation of E. Coli Endonuclease III via Modification of Its [4Fe-4S] Cluster by Nitric Oxide. *DNA Repair* **2003**, *2* (7), 809–817. https://doi.org/10.1016/S1568-7864(03)00065-X.
(28) Tinberg, C. E.; Tonzetich, Z. J.; Wang, H.; Do, L. H.; Yoda, Y.; Cramer, S. P.; Lippard, S. J. Characterization of Iron Dinitrosyl Species Formed in the Reaction of Nitric Oxide with a Biological Rieske Center. *J. Am. Chem. Soc.* **2010**, *132* (51), 18168–18176. https://doi.org/10.1021/ja106290p.
(29) Liaw, W.-F.; Chiang, M.-H.; Tsai, M.-L.; Chiou, T.-W.; Hsieh, C.-H.; Hsu, C.-N.; Wu, W.-Y. NO-to-[N2O2]2−-To-N2O Conversion Triggered by {Fe(NO)2}10-{Fe(NO)2}9 Dinuclear Dinitrosyl Iron Complex. *Inorg. Chem.* **2019**, *58*, 9586–9591. https://doi.org/10.1021/acs.inorgchem.9b01635.
(30) Kindermann, N.; Schober, A.; Demeshko, S.; Lehnert, N.; Meyer, F. Reductive Transformations of a Pyrazolate-Based Bioinspired Diiron–Dinitrosyl Complex. *Inorg. Chem.* **2016**, *55* (21), 11538–11550. https://doi.org/10.1021/acs.inorgchem.6b02080.
(31) Yeh, S.-W.; Lin, C.-W.; Li, Y.-W.; Hsu, I.-J.; Chen, C.-H.; Jang, L.-Y.; Lee, J.-F.; Liaw, W.-F. Insight into the Dinuclear {Fe(NO)2}10{Fe(NO)2}10 and Mononuclear {Fe(NO)2}10 Dinitrosyliron Complexes. *Inorg. Chem.* **2012**, *51* (7), 4076–4087. https://doi.org/10.1021/ic202332d.
(32) Gwak, J.; Ahn, S.; Baik, M.-H.; Lee, Y. One Metal Is Enough: A Nickel Complex Reduces Nitrate Anions to Nitrogen Gas. *Chem. Sci.* **2019**, *10* (18), 4767–4774. https://doi.org/10.1039/C9SC00717B.
(33) Stein, L. Y.; Klotz, M. G. The Nitrogen Cycle. *Current Biology* **2016**, *26* (3), R94–R98. https://doi.org/10.1016/j.cub.2015.12.021.
(34) Moreno-Vivián, C.; Cabello, P.; Martínez-Luque, M.; Blasco, R.; Castillo, F. Prokaryotic Nitrate Reduction: Molecular Properties and Functional Distinction among Bacterial Nitrate Reductases. *Journal of Bacteriology* **1999**, *181* (21), 6573–6584. https://doi.org/10.1128/JB.181.21.6573-6584.1999.
(35) Damon, P. L.; Wu, G.; Kaltsoyannis, N.; Hayton, T. W. Formation of a Ce(IV) Oxo Complex via Inner Sphere Nitrate Reduction. *J. Am. Chem. Soc.* **2016**, *138* (39), 12743–12746. https://doi.org/10.1021/jacs.6b07932.
(36) Delgado, M.; Gilbertson, J. D. Ligand-Based Reduction of Nitrate to Nitric Oxide Utilizing a Proton-Responsive Secondary Coordination Sphere. *Chem. Commun.* **2017**, *53* (81), 11249–11252. https://doi.org/10.1039/C7CC06541H.
(37) Craig, J. A.; Holm, R. H. Reduction of Nitrate to Nitrite by Molybdenum-Mediated Atom Transfer: A Nitrate Reductase Analog Reaction System. *J. Am. Chem. Soc.* **1989**, *111* (6), 2111–2115. https://doi.org/10.1021/ja00188a026.
(38) Einsle, O.; Messerschmidt, A.; Stach, P.; Bourenkov, G. P.; Bartunik, H. D.; Huber, R.; Kroneck, P. M. H. Structure of Cytochrome c Nitrite Reductase. *Nature* **1999**, *400* (6743), 476–480. https://doi.org/10.1038/22802.
(39) Murphy, M. E. P.; Turley, S.; Adman, E. T. Structure of Nitrite Bound to Copper-Containing Nitrite Reductase from Alcaligenes Faecalis MECHANISTIC IMPLICATIONS. *J. Biol. Chem.* **1997**, *272* (45), 28455–28460. https://doi.org/10.1074/jbc.272.45.28455.
(40) Burns, K. T.; Marks, W. R.; Cheung, P. M.; Seda, T.; Zakharov, L. N.; Gilbertson, J. D. Uncoupled Redox-Inactive Lewis Acids in the Secondary Coordination Sphere Entice

Ligand-Based Nitrite Reduction. *Inorg. Chem.* **2018**, *57* (16), 9601–9610. https://doi.org/10.1021/acs.inorgchem.8b00032.
(41) Kwon, Y. M.; Delgado, M.; Zakharov, L. N.; Seda, T.; Gilbertson, J. D. Nitrite Reduction by a Pyridinediimine Complex with a Proton-Responsive Secondary Coordination Sphere. *Chem. Commun.* **2016**, *52* (73), 11016–11019. https://doi.org/10.1039/C6CC05962G.
(42) Neese, F.; Ye, S. The Unusual Electronic Structure of Dinitrosyl Iron Complexes. *J. Am. Chem. Soc.* **2010**, *132*, 9646–9647. https://doi.org/10.1021/ja9091616.
(43) Hino, T.; Matsumoto, Y.; Nagano, S.; Sugimoto, H.; Fukumori, Y.; Murata, T.; Iwata, S.; Shiro, Y. Structural Basis of Biological N2O Generation by Bacterial Nitric Oxide Reductase. *Science* **2010**, *330* (6011), 1666–1670. https://doi.org/10.1126/science.1195591.
(44) Abucayon, E. G.; Khade, R. L.; Powell, D. R.; Zhang, Y.; Richter-Addo, G. B. Lewis Acid Activation of the Ferrous Heme–NO Fragment toward the N–N Coupling Reaction with NO To Generate N2O. *J. Am. Chem. Soc.* **2018**, *140* (12), 4204–4207. https://doi.org/10.1021/jacs.7b13681.
(45) Usyskin-Tonne, A.; Hadar, Y.; Minz, D. Altering N 2 O Emissions by Manipulating Wheat Root Bacterial Community. *Scientific Reports* **2019**, *9* (1), 7613. https://doi.org/10.1038/s41598-019-44124-3.
(46) Arikawa, Y.; Onishi, M. Reductive N–N Coupling of NO Molecules on Transition Metal Complexes Leading to N2O. *Coordination Chemistry Reviews* **2012**, *256* (5), 468–478. https://doi.org/10.1016/j.ccr.2011.10.023.
(47) Viebrock, A.; Zumft, W. G. Molecular Cloning, Heterologous Expression, and Primary Structure of the Structural Gene for the Copper Enzyme Nitrous Oxide Reductase from Denitrifying Pseudomonas Stutzeri. *Journal of Bacteriology* **1988**, *170* (10), 4658–4668. https://doi.org/10.1128/jb.170.10.4658-4668.1988.
(48) Portmann, R. W.; Daniel, J. S.; Ravishankara, A. R. Stratospheric Ozone Depletion Due to Nitrous Oxide: Influences of Other Gases. *Philos Trans R Soc Lond B Biol Sci* **2012**, *367* (1593), 1256–1264. https://doi.org/10.1098/rstb.2011.0377.
(49) Doyle, L. E.; Piers, W. E.; Borau-Garcia, J. Ligand Cooperation in the Formal Hydrogenation of N2O Using a PCsp2P Iridium Pincer Complex. *J. Am. Chem. Soc.* **2015**, *137* (6), 2187–2190. https://doi.org/10.1021/ja512602m.
(50) Zeng, R.; Feller, M.; Ben-David, Y.; Milstein, D. Hydrogenation and Hydrosilylation of Nitrous Oxide Homogeneously Catalyzed by a Metal Complex. *J. Am. Chem. Soc.* **2017**, *139* (16), 5720–5723. https://doi.org/10.1021/jacs.7b02124.
(51) Luca, O. R.; Crabtree, R. H. Redox-Active Ligands in Catalysis. *Chem. Soc. Rev.* **2013**, *42* (4), 1440–1459. https://doi.org/10.1039/C2CS35228A.
(52) Shimizu, D.; Osuka, A. Porphyrinoids as a Platform of Stable Radicals. *Chem. Sci.* **2018**, *9* (6), 1408–1423. https://doi.org/10.1039/C7SC05210C.
(53) Roncaroli, F.; Videla, M.; Slep, L. D.; Olabe, J. A. New Features in the Redox Coordination Chemistry of Metal Nitrosyls {M–NO+; M–NO; M–NO−(HNO)}. *Coordination Chemistry Reviews* **2007**, *251* (13), 1903–1930. https://doi.org/10.1016/j.ccr.2007.04.012.
(54) Serres, R. G.; Grapperhaus, C. A.; Bothe, E.; Bill, E.; Weyhermüller, T.; Neese, F.; Wieghardt, K. Structural, Spectroscopic, and Computational Study of an Octahedral, Non-

Heme {Fe−NO}6-8 Series: [Fe(NO)(Cyclam-Ac)]2+/+/0. *J. Am. Chem. Soc.* **2004**, *126* (16), 5138–5153. https://doi.org/10.1021/ja030645+.

(55) Enemark, J. H.; Feltham, R. D. Principles of Structure, Bonding, and Reactivity for Metal Nitrosyl Complexes. *Coordination Chemistry Reviews* **1974**, *13* (4), 339–406. https://doi.org/10.1016/S0010-8545(00)80259-3.

(56) Bart, S. C.; Chłopek, K.; Bill, E.; Bouwkamp, M. W.; Lobkovsky, E.; Neese, F.; Wieghardt, K.; Chirik, P. J. Electronic Structure of Bis(Imino)Pyridine Iron Dichloride, Monochloride, and Neutral Ligand Complexes: A Combined Structural, Spectroscopic, and Computational Study. *J. Am. Chem. Soc.* **2006**, *128* (42), 13901–13912. https://doi.org/10.1021/ja064557b.

(57) Kendall, A. J.; Zakharov, L. N.; Gilbertson, J. D. Synthesis and Stabilization of a Monomeric Iron(II) Hydroxo Complex via Intramolecular Hydrogen Bonding in the Secondary Coordination Sphere. *Inorg. Chem.* **2010**, *49* (19), 8656–8658. https://doi.org/10.1021/ic101408e.

(58) Gilbertson, J. D.; Kowalczyk, T.; Zakharov, L. N.; Oswald, V. F.; Aguayo, K. J.; Deshaye, M. Y.; Kwon, Y. M.; Burns, K. T.; Cheung, P. M. Hemilabile Proton Relays and Redox Activity Lead to {FeNO}x and Significant Rate Enhancements in NO2 − Reduction. *J. Am. Chem. Soc.* **2018**, *40*, 17040–17050. https://doi.org/10.1021/jacs.8b08520.

(59) Seo, J.; Cabelof, A. C.; Chen, C.-H.; Caulton, K. G. Selective Deoxygenation of Nitrate to Nitrosyl Using Trivalent Chromium and the Mashima Reagent: Reductive Silylation. *Chem. Sci.* **2019**, *10* (2), 475–479. https://doi.org/10.1039/C8SC02979B.

(60) Evans, W. J.; Grate, J. W.; Bloom, I.; Hunter, W. E.; Atwood, J. L. Synthesis and X-Ray Crystallographic Characterization of an Oxo-Bridged Bimetallic Organosamarium Complex, [(C5Me5)2Sm]2(.Mu.-O). *J. Am. Chem. Soc.* **1985**, *107* (2), 405–409. https://doi.org/10.1021/ja00288a021.

(61) Brady, E. D.; Clark, D. L.; Keogh, D. W.; Scott, B. L.; Watkin, J. G. A Mechanistic Study of the Samarium(II)-Mediated Reduction of Aryl Nitro Compounds to the Corresponding Arylamines. The Crystal Structures of {Sm[N(SiMe3)2]2(Thf)}2(M2-O) and [(Me3Si)2N]2Sm(Thf)(μ-PhNNPh)Sm[N(SiMe3)2]2. *J. Am. Chem. Soc.* **2002**, *124* (24), 7007–7015. https://doi.org/10.1021/ja0168918.

(62) A Quantitative Scale of Oxophilicity and Thiophilicity | Inorganic Chemistry https://pubs.acs.org/doi/10.1021/acs.inorgchem.6b01702 (accessed Apr 12, 2021).

(63) Maia, L. B.; Moura, J. J. G. How Biology Handles Nitrite. *Chem. Rev.* **2014**, *114* (10), 5273–5357. https://doi.org/10.1021/cr400518y.

(64) Chirik, P. J.; Wieghardt, K. Radical Ligands Confer Nobility on Base-Metal Catalysts. *Science* **2010**, *327* (5967), 794–795. https://doi.org/10.1126/science.1183281.

(65) Christe, K. O.; Dixon, D. A.; Mercier, H. P. A.; Sanders, J. C. P.; Schrobilgen, G. J.; Wilson, W. W. Tetrafluorophosphite, PF4-, Anion. *J. Am. Chem. Soc.* **1994**, *116* (7), 2850–2858. https://doi.org/10.1021/ja00086a018.

(66) Delgado, M.; Sommer, S. K.; Swanson, S. P.; Berger, R. F.; Seda, T.; Zakharov, L. N.; Gilbertson, J. D. Probing the Protonation State and the Redox-Active Sites of Pendant Base Iron(II) and Zinc(II) Pyridinediimine Complexes. *Inorg. Chem.* **2015**, *54* (15), 7239–7248. https://doi.org/10.1021/acs.inorgchem.5b00633.

(67) Nitopi, S.; Bertheussen, E.; Scott, S. B.; Liu, X.; Engstfeld, A. K.; Horch, S.; Seger, B.; Stephens, I. E. L.; Chan, K.; Hahn, C.; Nørskov, J. K.; Jaramillo, T. F.; Chorkendorff, I. Progress and Perspectives of Electrochemical CO2 Reduction on Copper in Aqueous Electrolyte. *Chem. Rev.* **2019**, *119* (12), 7610–7672. https://doi.org/10.1021/acs.chemrev.8b00705.

(68) Abdinejad, M.; Seifitokaldani, A.; Dao, C.; Sargent, E. H.; Zhang, X.; Kraatz, H. B. Enhanced Electrochemical Reduction of CO2 Catalyzed by Cobalt and Iron Amino Porphyrin Complexes. *ACS Appl. Energy Mater.* **2019**, *2* (2), 1330–1335. https://doi.org/10.1021/acsaem.8b01900.

(69) Thammavongsy, Z.; Seda, T.; Zakharov, L. N.; Kaminsky, W.; Gilbertson, J. D. Ligand-Based Reduction of CO2 and Release of CO on Iron(II). *Inorg. Chem.* **2012**, *51* (17), 9168–9170. https://doi.org/10.1021/ic3015404.

(70) Xémard, M.; Goudy, V.; Braun, A.; Tricoire, M.; Cordier, M.; Ricard, L.; Castro, L.; Louyriac, E.; Kefalidis, C. E.; Clavaguéra, C.; Maron, L.; Nocton, G. Reductive Disproportionation of CO2 with Bulky Divalent Samarium Complexes. *Organometallics* **2017**, *36* (23), 4660–4668. https://doi.org/10.1021/acs.organomet.7b00630.

(71) Evans, W. J.; Ulibarri, T. A.; Ziller, J. W. Isolation and X-Ray Crystal Structure of the First Dinitrogen Complex of an f-Element Metal, [(C5Me5)2Sm]2N2. *J. Am. Chem. Soc.* **1988**, *110* (20), 6877–6879. https://doi.org/10.1021/ja00228a043.

(72) Evans, W. J.; Bloom, I.; Hunter, W. E.; Atwood, J. L. Synthesis and X-Ray Crystal Structure of a Soluble Divalent Organosamarium Complex. *J. Am. Chem. Soc.* **1981**, *103* (21), 6507–6508. https://doi.org/10.1021/ja00411a046.

(73) Bianchini, C.; Mantovani, G.; Meli, A.; Migliacci, F.; Zanobini, F.; Laschi, F.; Sommazzi, A. Oligomerisation of Ethylene to Linear α-Olefins by New Cs- and C1-Symmetric [2,6-Bis(Imino)Pyridyl]Iron and -Cobalt Dichloride Complexes. *European Journal of Inorganic Chemistry* **2003**, *2003* (8), 1620–1631. https://doi.org/10.1002/ejic.200390213.